Particle Simulations and Polar Spacecraft Observations of Solitary Waves in the Magnetosphere

A THESIS

SUBMITTED TO THE FACULTY OF THE GRADUATE SCHOOL

OF THE UNIVERSITY OF MINNESOTA

BY

James Patrick Crumley

IN PARTIAL FULFILLMENT OF THE REQUIREMENTS

FOR THE DEGREE OF

DOCTOR OF PHILOSOPHY

Robert L. Lysak and Cynthia A. Cattell, Advisors

August, 2002

UNIVERSITY OF MINNESOTA

This is to certify that I have examined this bound copy of a doctoral thesis by

James Patrick Crumley

and have found that it is complete and satisfactory in all respects and that any and all revisions required by the final examining committee have been made.

Robert L. Lysak and Cynthia A. Cattell

(Faculty Advisors)

GRADUATE SCHOOL

August, 2002

Particle Simulations and Polar Spacecraft Observations of Solitary Waves in the Magnetosphere

A THESIS

SUBMITTED TO THE FACULTY OF THE GRADUATE SCHOOL

OF THE UNIVERSITY OF MINNESOTA

BY

James Patrick Crumley

IN PARTIAL FULFILLMENT OF THE REQUIREMENTS

FOR THE DEGREE OF

DOCTOR OF PHILOSOPHY

Robert L. Lysak and Cynthia A. Cattell, Advisors

August, 2002

© James Patrick Crumley 2002

Dedication

This work is dedicated to my wife, Dana. Without her support I never would have gotten so far.

Acknowledgements

First, I would like to thank my advisors Bob Lysak and Cindy Cattell for all of their assistance and guidance in this work. Their help was crucial in getting me through this observational/computational hybrid dissertation. Thanks also to the rest of my thesis committee of John Wygant, Tom Jones, and Keith Olive for their help.

This work would not have been possible without all of the resources that were made available to me. The Polar spacecraft provided wonderful data and for that I am grateful to everyone who worked on Polar and to NASA for funding it. In particular, I would like to thank Forrest Mozer, Principal Investigator for Polar's Electric Field Instrument, for getting a fully three dimensional electric field instrument on Polar. I would also like to thank Jack Scudder and Craig Kletzing for access to Hydra data, Harry Collin and Bill Peterson for access to TIMAS data, and Chris Russell for access to MFE data. I am also grateful to NASA for supporting my research through my advisors' grants and for awarding me a fellowship under their Graduate Student Research Program (GSRP - grant number NAG5-3182).

I would also like to thank my fellow graduate students, John Dombeck, Tim Streed, Doug Rowland, Mike Johnson, Andreas Keiling, Kris Sigsbee, and Kristy Keller, for all of their help and the fun times that we had while in graduate school. Thanks especially to John Dombeck whose work analyzing Polar spacecraft data is the basis for my observational work studying solitary waves. I would like to thank Tim Streed for turning me on to LaTeX, without which this would not look quite like this. Thanks to Kristy Keller and Kris Sigsbee for showing that it was actually possible get a Ph. D. in space physics, and Andreas Keiling for showing that it was

possible to do it relatively quickly. For being excited every time I made a new type of plot I am grateful to Mike Johnson. I would like to thank Doug Rowland for being the last of our cadre to defend his thesis, so I don't have to be the one to "shut out the lights."

Lastly, but not least I would like to thank my family for all of their support and encouragement. I have to thank my parents, Mike and Sharon Crumley, for inspiring in me curiosity and a love of learning. I would also like to thank my brother, Kevin, for giving giving me someone to compete against growing up, and my sister and brother, Katie and Rob, for putting up with their biggest brother. And once again, I'd like to thank my wife, Dana, the light of my life for everything.

ABSTRACT

Both linear and nonlinear electromagnetic waves are ubiquitous in the magnetosphere. In this study, the problem of waves, which previously had been identified as electrostatic ion cyclotron waves, but now have been found to have magnetic as well as electric fluctuations, is examined. Cold and kinetic dispersion relations are used to study these waves, and the results support the idea that these ion cyclotron waves are actually a generalized EIC wave mode that has magnetic, as well as electric, field fluctuations.

Solitary waves are isolated, nonlinear waves which travel parallel to the background magnetic field and have been observed throughout the magnetosphere. Solitary waves are divided into two classes: slower waves which are associated with ion beams, and faster waves which are associated with electron beams. In this study, solitary waves are examined both observationally and through the use of computer simulations. The computer simulations of solitary waves use ES2, a 2.5D particle-in-cell simulation. The observations of solitary waves rely on data from EFI, the Polar spacecraft's electric field instrument. Solitary wave characteristics, including the speeds, electric potential, and spatial extent, are presented from and compared between the observations and simulations. These results show that the speeds of the ion solitary waves lie between the hydrogen and oxygen beam speeds, which supports the theory that ion solitary waves may form from two-stream interactions between ion beams. These observations and simulations also show that the scale size of solitary waves is roughly 22 Debye lengths in both the directions parallel and perpendicular to the background magnetic field. High altitude electron solitary waves in this study are found to have speeds of thousands of km/s and have potential amplitudes that are directly proportional to their scale size parallel to the magnetic field. The median parallel scale sizes for the electron solitary waves are approximately 15 Debye lengths. Though perpendicular scale sizes cannot be observed directly, the ratio of the parallel electric

field to the perpendicular electric field, which should scale as the ratio of the perpendicular to parallel scale size, matches a theoretical predicted relation for electron solitary waves.

Contents

List of Figures

List of Tables

Chapter 1

Introduction

The magnetosphere is the region of space where the Earth's magnetic field is the dominant magnetic field which controls much of the motion of particles. It is located between the Earth's atmosphere, where neutral gases are dominant, and interplanetary space, which is dominated by the solar wind. In the magnetosphere the dominant form of matter is plasma. The plasma is usually collisionless. Due to the charges on the particles in the plasma, electric and magnetic fields are ubiquitous and dynamic in the magnetosphere. One area where particularly interesting waves are seen is the auroral acceleration region. In this region the electrons which cause the aurora are accelerated. Some of the waves seen in this region (Figure 1.1) are the subjects of my research. The large spikes seen in the top panel of Figure 1.1 are solitary waves which are observed as non-linear electric field structures that travel parallel to the background magnetic field and are introduced in Chapter 3. The waves in the bottom panel of Figure 1.1 are ion cyclotron waves which are linear mode1 with electric fields perpendicular to the background magnetic field and are described further in Chapter 2. These linear and nonlinear waves within the magnetospheric plasma will be the focus of this study. To motivate the discussion of the waves, this chapter provides a brief introduction to the magnetosphere and the aurora. More detailed introduction to these topics can be found in many sources including: *Parks* [1991], *Baumjohann and Treumann* [1997], *Kelley and Heelis* [1989], *Kivelson et al.* [1995],

and *Suess and Tsurutani* [1998]. Section 1.1 discusses the magnetosphere in general, and introduces some of the regions of the magnetosphere discussed later. Section 1.2 discusses the origins of the aurora and the waves seen in the region where the aurora is generated.

1.1 Magnetospheric Topography

The magnetosphere has several distinct regions which have very different characteristics (Figure 1.2). Typical plasma parameters for several of the regions mentioned below are included in Table 1.1. The first feature of the magnetosphere, if one heads toward the Earth from the Sun, is the bow shock, which is located roughly 10–15 Earth radii (R_E) from the Earth. The bow shock is caused by the super Alfvénic solar wind encountering an obstruction in the form of the Earth's magnetic field. This shock, when viewed in the rest frame of the Earth, is somewhat analogous to the wave in front of a boat seen from the boat's frame when it travels through water. The characteristics of this shock are complicated, though, by the fact that the fluid in this case is a collisionless plasma.

The solar wind is diverted by the Earth's magnetic field at the bow shock, but the transition to the region dominated by the Earth's magnetic field occurs at the magnetopause. The magnetopause separates the Earth's magnetic field and plasma from the solar wind and the interplanetary magnetic field (IMF). The magnetopause occurs at the place where the magnetic and plasma pressure from the magnetosphere balance the dynamic pressure of the solar wind. The region between the magnetopause and the bow shock is a region called the magnetosheath. The magnetosheath serves as a transition between the dense, cool, but quickly moving solar wind plasma and the less dense, hot, and slower moving magnetospheric plasma. The magnetosheath plasma tends to flow past the magnetosphere and eventually merge back into the solar wind far downstream. Some magnetosheath plasma enters the magnetosphere through magnetic reconnection, both at the dayside and tail portions of the magnetopause.

The part of the magnetosphere which stretches out behind the Earth in the anti-sunward

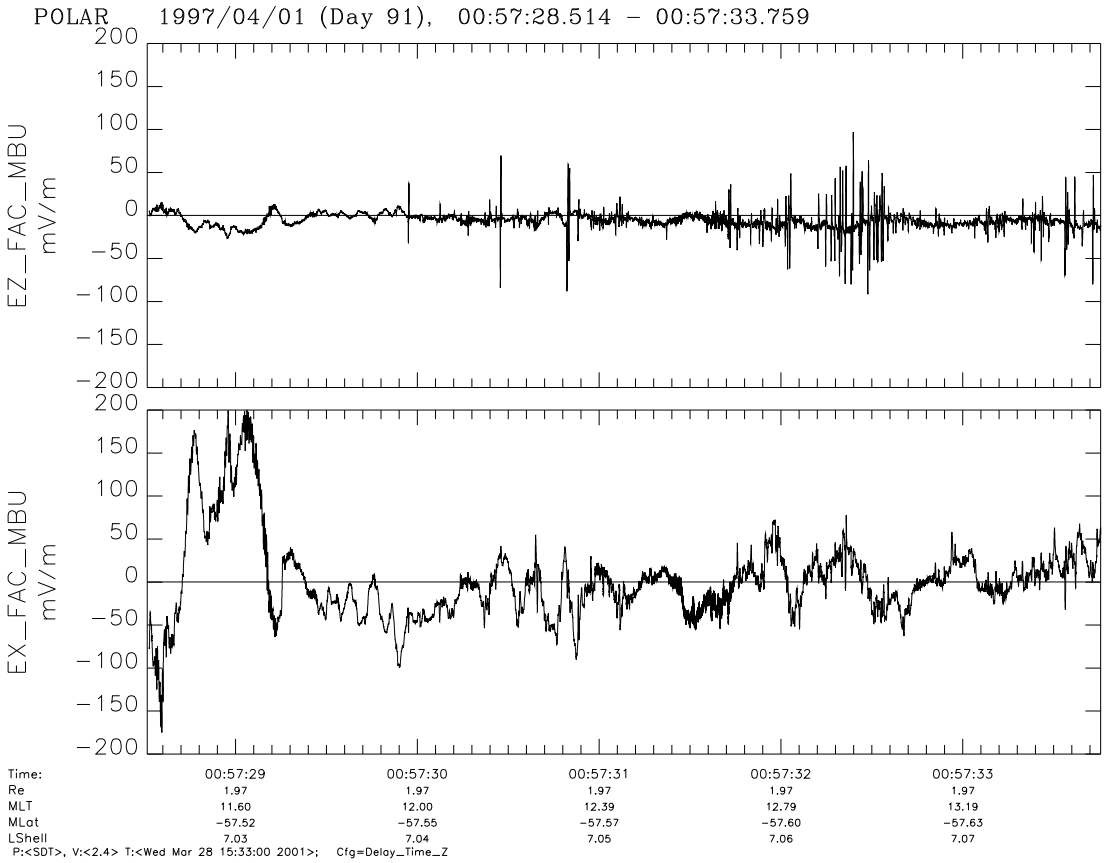

Figure 1.1: This figure shows sample solitary waves and ion cyclotron waves as observed by the Polar spacecraft. The top panel shows the electric field parallel to the background magnetic field measured in mV/m. The bottom panel shows the a component of the electric field perpendicular to the background magnetic field. Solitary waves are the isolated bipolar structures in the parallel electric field which are most evident between 00:57:30 and 00:57:31 in this figure. Solitary waves are the subject of Chapters 3 through 7. The waves seen in the perpendicular direction are ion cyclotron waves, which are the subject of Chapter 2.

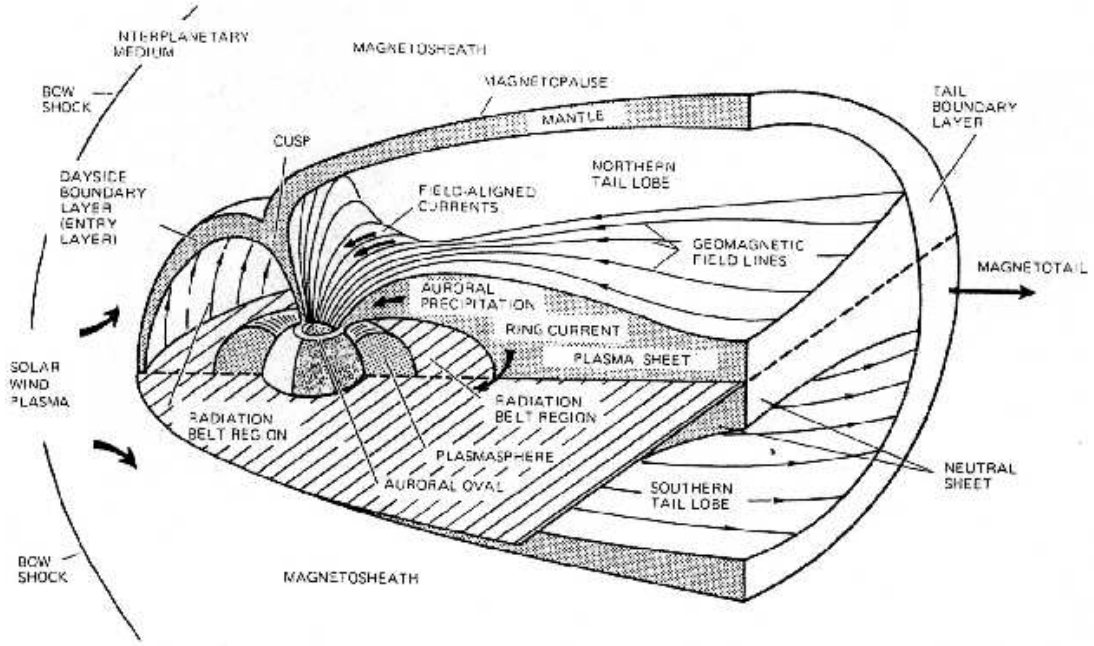

Figure 1.2: An overview of the magnetosphere and the regions within it [*Kelley and Heelis*, 1989].

Region	Number Density (cm^{-1})	Temperature (eV)
Solar Wind	10	10
Plasmasphere	1000	10
Ring Current	0.5	10^5
Radiation Belts	0.5	10^6
Plasma sheet	5	1000
Tail Lobe	0.1	1000
Auroral Acceleration Region	10^6	10

Table 1.1: Magnetospheric Plasma Parameters [*Parks*, 1991; *Baumjohann and Treumann*, 1997]

direction is known as the magnetotail. Just as the bow shock is analogous to the wave in front of a boat moving through water, the magnetotail is like the wake behind the boat. The length of the magnetotail ($\sim$ 100-200 R_E) and its characteristics depend strongly on the solar wind conditions. The outer parts of the magnetotail are the lobes, which have very low density or on open field lines. The nearer and more central region of the tail is called the plasma sheet. This region contains relatively hot and medium density particle distributions. Near the magnetopause, in the polar region, is a layer called the cusp which is the place where the magnetic field is expected to be zero in closed field line models of the magnetosphere. The region between the lobes and the plasma sheet is the plasma sheet boundary layer. This area is interesting because its field lines map down to the auroral oval, and field-aligned flows of particles often occur in this region, both towards the tail and towards the auroral oval, as well as Poynting fluxes associated with Alfvèn waves.

In still closer to the Earth and at low latitudes, and overlapping in space, are the radiation belts, ring current, and the plasmasphere. This area of the magnetosphere corotates with Earth unlike most regions of the magnetosphere. The plasmasphere is dense and cold. Since it is the portion of the magnetosphere that borders on the ionosphere at lower latitudes, it gets its cold

plasma from the ionosphere. The radiation belts are highly energetic particles which have been trapped by the Earth's magnetic field. Ring current particles have a temperature between that of the plasmasphere and the radiation belts. The ring current gets its name because the electrons and ions drift in opposite directions around the Earth, due to the Earth's dipole magnetic field, forming an electric current. Finally, the innermost region of the magnetosphere is the ionosphere. This region serves as the transition between the rest of the magnetosphere, which is plasma dominated, and the atmosphere, which is dominated by neutral atoms and molecules. In contrast to the rest of the magnetosphere, the plasma in the ionosphere is collisional which changes the plasma dynamics in this region.

1.2 The Aurora

The Aurora Borealis (or Australis) are colored light displays often visible at night at high latitudes. The aurora is caused by precipitation of energetic (up to a tens of keV) electrons into the ionosphere. These energetic electrons interact with the neutral ionospheric gas, causing the excitation of electrons in some of the gas. When these electrons fall back to their ground states, they give off light at discrete wavelengths, some of which are visible. These visible emissions lead to the distinctive greens, blues and reds of the aurora.

Most aurora occur near the poles in a region called the auroral oval. The size and shape of the auroral oval changes depending on the conditions in the magnetosphere. On average it is a band about 20° in radius and 5° wide and it is centered 5° to the night side of the magnetic pole (Figure 1.3). This auroral oval is at the same location where upward and downward field-aligned currents are seen in the ionosphere (Figure 1.4). These currents are associated with convection occurring in the magnetosphere and ionosphere and with the ring current.

One of the most interesting questions in magnetospheric physics involves what causes the acceleration of auroral particles. The auroral electrons must have energies of at least 100 eV (and up to $\gtrsim$ 10 keV), but the thermal energies in this auroral region are much lower ($\sim$ 1 eV),

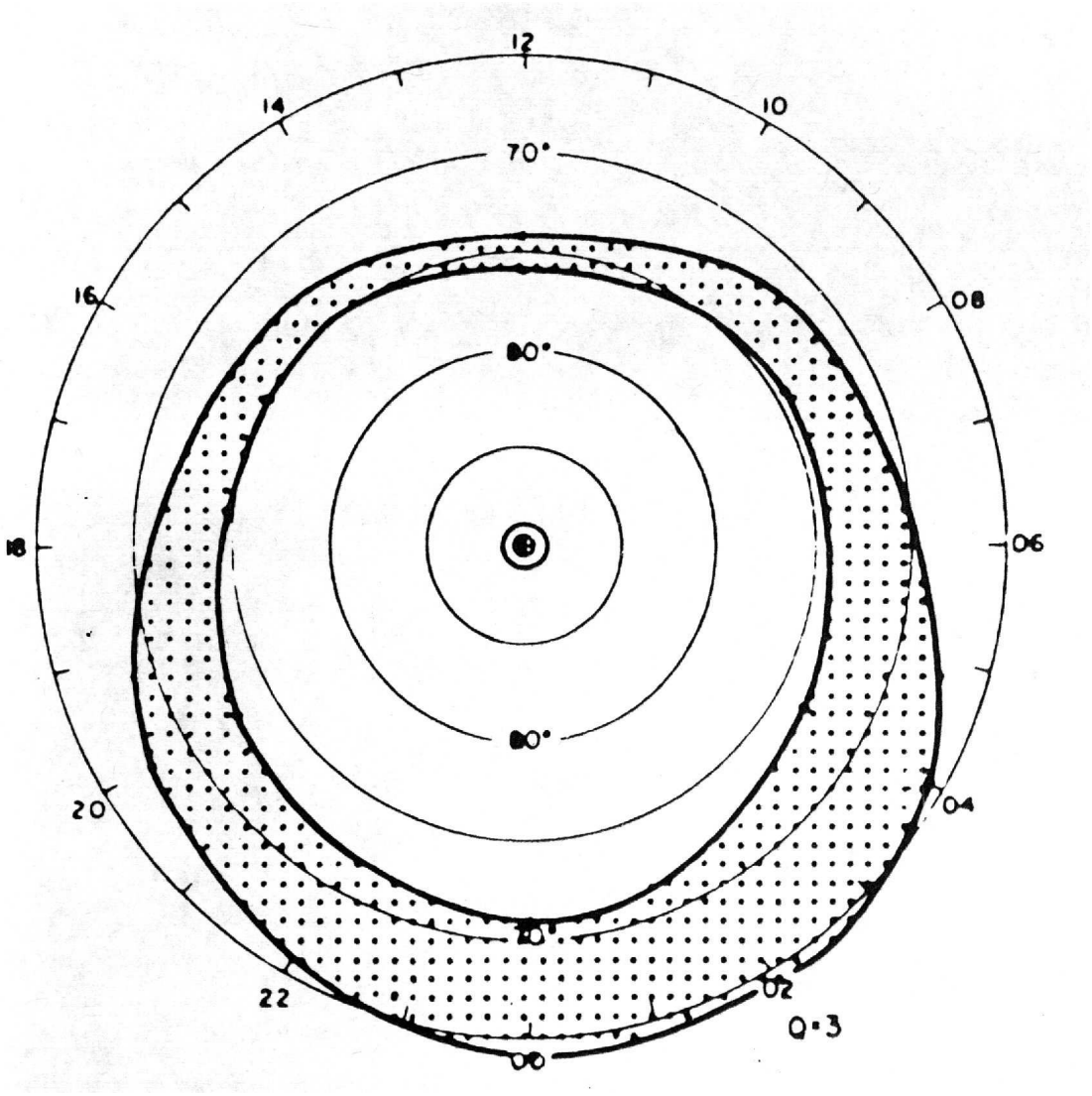

Figure 1.3: This figure shows the regions where the aurora are typically observed.

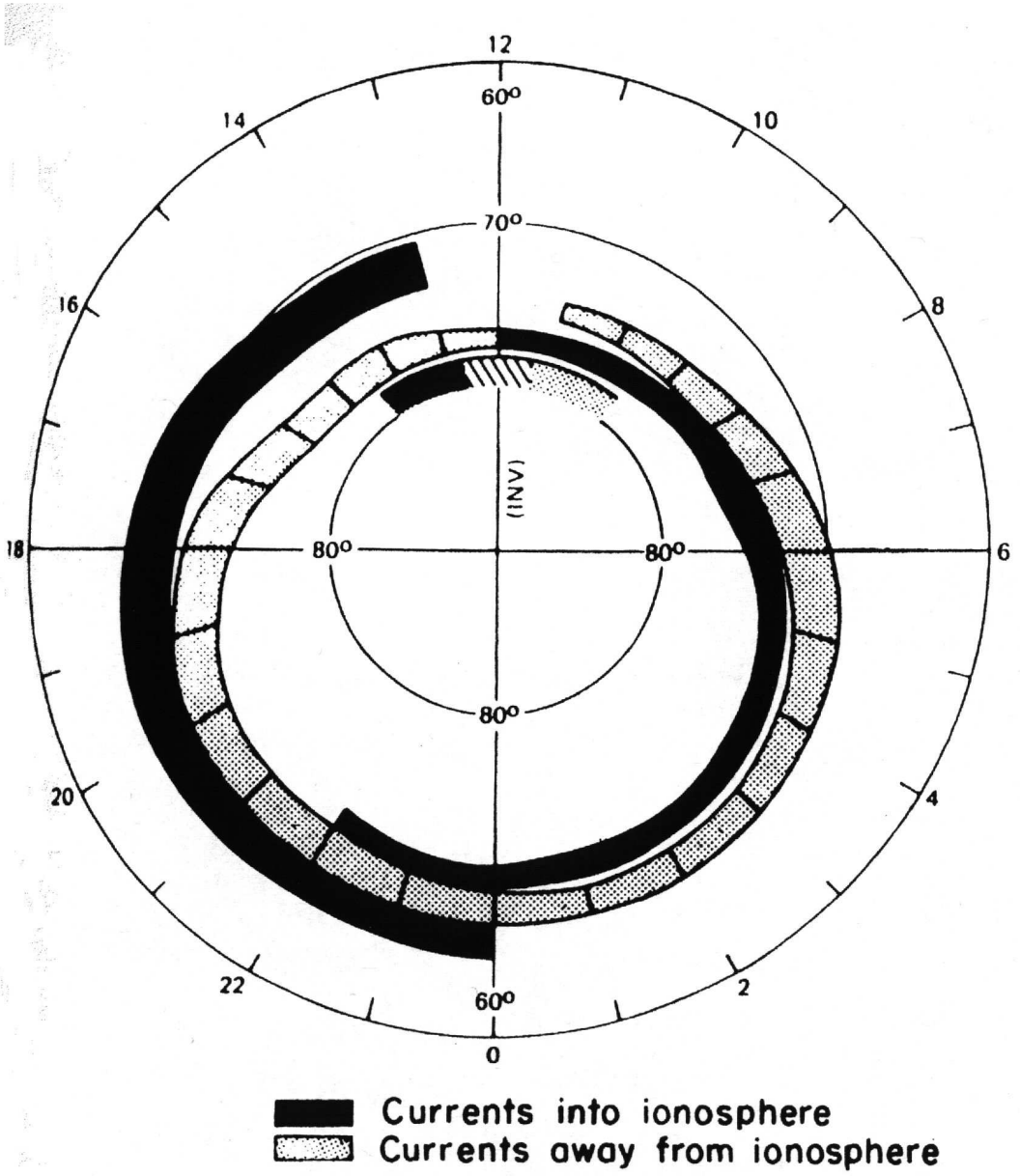

Figure 1.4: The field-aligned currents in the polar region of the ionosphere [*Iijima and Potemra*, 1976].

though there are often hotter plasma sheet particles as well [*Parks*, 1991]. It is generally agreed that there must be electric fields aligned parallel to the magnetic field which accelerate the electrons to the necessary energy. This parallel electric field is believed to be caused by a quasi-static potential drop along the magnetic lines in the auroral acceleration region, though the details of the processes that sustain this potential drop are not entirely worked out [*Ergun et al.*, 1998c; *McFadden et al.*, 1999a; *Mozer and Kletzing*, 1998]. It is also believed that the region in which electrons are accelerated is roughly located between 1400 and 14000 km up auroral magnetic fields lines from the surface of the Earth [*Reiff et al.*, 1993].

Though the details of the generation of the quasi-static potential have not all been worked out, both linear and nonlinear waves have been observed in this region. These waves are seen in association with field-aligned currents and with ion and electron beams, which probably serve as their source of free energy. Though the role that these waves play in auroral acceleration is not completely understood, studying them should provide some insight into the interrelation of waves, currents, and particle acceleration. Study of the physical processes involved in the acceleration of auroral particles is important not only for better understanding of the aurora, but also because the the processes involved may be applicable elsewhere. In particular, acceleration processes are an important topic of research in many astrophysical settings. The processes which cause the acceleration of some high energy cosmic rays are one example of an astrophysical problem where acceleration mechanisms are being studied. The availability of in situ measurements in the magnetosphere leads to the opportunity to probe auroral acceleration processes in ways which are unavailable for astrophysical processes. So understanding the causes of the aurora may also illuminate the physics of other regions.

1.3 Outline

The remainder of this thesis discusses linear and non-linear waves in the magnetosphere, with emphasis on waves in the auroral acceleration region. Chapter 2 deals with cold and kinetic

linear dispersion of these waves and the use of these dispersion relations to study ion cyclotron waves in the auroral acceleration region. Later chapters deal with solitary waves, which are non-linear waves seen in boundary layers throughout the magnetosphere, though most notably in the auroral acceleration region. Chapter 3 reviews previous observations, theories, and simulations of solitary waves. The methods and programs used to simulate solitary waves in this work are covered in Chapter 4, while the results of those simulations are covered in Chapter 6. The observational techniques used to study solitary waves in this thesis are covered in Chapter 5, while the results from these observations are covered in Chapter 7. Finally, a summary of the conclusions of this work and suggestions for future study is presented in Chapter 8.

Chapter 2

Linear Waves and Dispersion Relations

There are many different types of plasma waves in the magnetosphere. As a first approximation, some of these waves can be studied using fairly simple assumptions and methods. In many cases waves within plasmas can be treated as linear, even though the fundamental equations used to describe a plasma have nonlinear terms. These nonlinear terms can often be dropped if the perturbations in density, electric field, and magnetic field caused in the plasma are small enough. Linear waves also have the property that, if more than one wave is present, they can simply be superposed. In general, two nonlinear waves overlap to create an overall wave which is not necessarily a simple superposition of the two.

To study linear waves in plasmas, the equations describing the waves must be linearized. This involves using perturbation theory on Maxwell's equations. The variables in the equations, such as the electric and magnetic fields, are separated into constant, background portions and varying, wave portions. Then the terms of order 2 or higher in the small perturbation variables are dropped. This leads to equations which are first order in these wave variables and the system can be solved using linear techniques. Studying these linear waves can be an important method of learning about physical processes in the magnetosphere.

This chapter begins with a discussion of observations of ion cyclotron waves in the auroral acceleration region which motivate this study of linear waves. Then the utility of dispersion relations is discussed. The dispersion relation in the case of a cold, magnetized plasma is next derived and this dispersion relation is used to study the ion cyclotron in the auroral acceleration region. Since the cold plasma approximation is not satisfied in the observations of the ion cyclotron waves, the kinetic dispersion relation must be applied to these observations. The results from the kinetic dispersion relation are then compared to the results from the cold dispersion relation.

2.1 Motivation

The motivation for calculating the cold dispersion relation was to analyze the properties of ion cyclotron waves that are seen in the auroral acceleration region. Ion cyclotron waves are often seen in association with ion or electron beams. The waves usually propagate at an angle that is almost perpendicular to the background magnetic field. These waves are seen at the O^+ and He^+ cyclotron frequencies, as well as the H^+ cyclotron frequency. Also, magnetic field components are sometimes, but not always seen, with these waves.

Wave modes with frequencies just above the multiples of the ion cyclotron frequency were typically identified as electrostatic ion cyclotron (EIC) waves [*Kintner et al.*, 1979; *Cattell et al.*, 1991]. Typically it is assumed that EIC waves have no magnetic fluctuation, which was consistent with these early observations. Some of the earlier spacecraft did not have instruments that were capable of measuring these magnetic fluctuations. More recent observations of ion cyclotron waves with the FAST (Fast Auroral SnapshoT) spacecraft, which is capable of measuring magnetic fluctuations, have shown that the ion cyclotron waves, with frequencies both above and below the ion cyclotron frequency, often have magnetic fluctuations [*Chaston et al.*, 1998]. An example of these cyclotron waves observed by the FAST spacecraft is shown in Figure 2.1. Another type of cyclotron wave known as the electromagnetic ion cyclotron (EMIC)

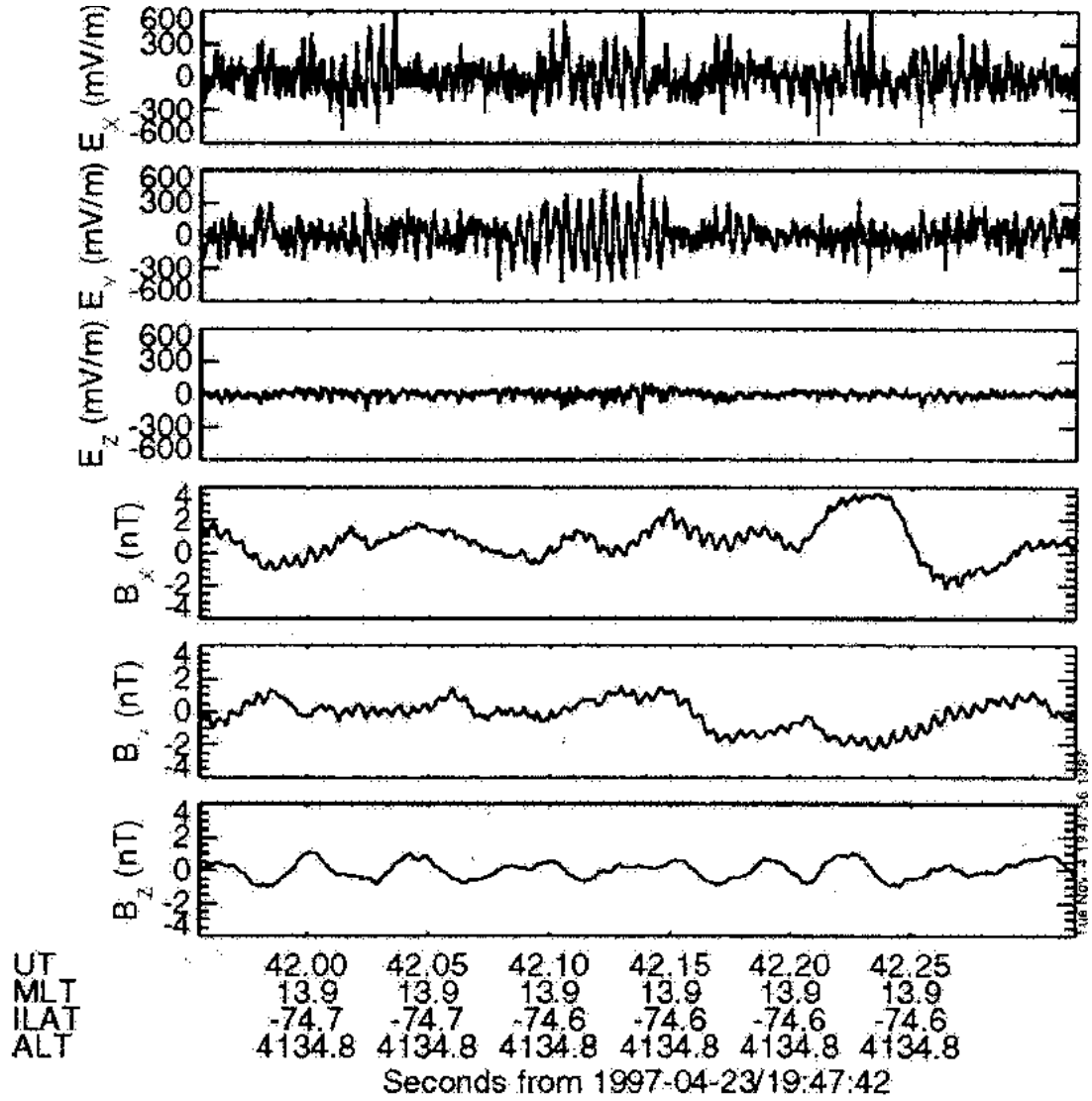

Figure 2.1: Plotted above is FAST spacecraft observations of ion cyclotron waves in the auroral acceleration region. The top three panels show the electric field in magnetic field-aligned coordinates (where z is along the magnetic field direction) measured in mV/m. The bottom three panels show the magnetic field in the same coordinates measured in nT. The ion cyclotron waves are the oscillations in the x and y components of the electric field. The smaller magnetic oscillations are also apparent in the x and y components. These waves are occurring just above the ion cyclotron frequency, where EIC waves are expected [plot from *Chaston et al.*, 1998].

wave does have magnetic perturbations. EMIC waves only occur below the ion cyclotron frequency (the frequency of EMIC waves approaches the ion cyclotron frequency as the the wavenumber goes to infinity, while the frequency of EIC waves approaches the ion cyclotron frequency as the wavenumber approaches 0). EMIC waves have also been identified in the auroral zone [*Temerin and Lysak*, 1984]. Observations of waves at frequencies where EIC waves are expected (just below the ion cyclotron frequency) that have magnetic fluctuations motivate this study to find the exact mode that is being observed.

2.2 Dispersion Relations

Dispersion relations are an important tool for the study of plasma waves, since they encapsulate much of the information about wave modes. A dispersion relation shows the angular frequency (ω) as a function of wavenumber (k). An example of a dispersion relation, which is derived in Section 2.3, is shown in Figure 2.4. The dispersion relation also illustrates the phase velocity ($v_{phase} = \frac{\omega}{k}$) and the group velocity ($v_{group} = \frac{\partial \omega}{\partial k}$) of wave modes. Reflection points for wave modes are seen on dispersion relations as the places where the wave number goes to 0 (infinite phase velocity). Resonance points, where wave modes can transfer energy to the plasma, are locations where the wave number hits a limiting value (zero phase velocity). The imaginary portion of the frequency (which is not presented here) is the growth rate for the wave mode, so this imaginary portion is crucial for examining what modes are expected to be observed in various plasma conditions.

2.3 Cold Dispersion Relations

A simple case, which yields many of the wave modes of interest in a plasma, is to consider waves in a cold, magnetized plasma from a fluid perspective. Looking at the cold dispersion relationship gives insight into the properties of plasma waves at a fairly basic level. Cold dispersion relations can function as a first approximation for waves, though the validity of

that approximation varies depending on plasma properties. Hot plasmas cause changes to the characteristics of the waves, which cannot be accounted for with a cold dispersion relation.

2.3.1 Theory

The dispersion relation for these wave modes can be found by starting from the single particle equation of motion

$$n_s m_s \frac{d\vec{v}_s}{dt} = n_s(\vec{E} + \frac{\vec{v}_s}{c} \times \vec{B}) - \vec{\nabla} \cdot \overleftrightarrow{\Psi}_s \tag{2.1}$$

[following from *Stix*, 1992]. In this equation n_s is the number density of plasma species s, q_s is the charge on that species, $\vec{v}_s$ is the velocity, $\vec{E}$ is the electric field, $\vec{B}$ is the magnetic field, and $\overleftrightarrow{\Psi}_s$ is the fluid stress tensor. $\overleftrightarrow{\Psi}_s$ is 0 because of the assumption that the plasma is cold, which means that the plasma's pressure is 0. By using perturbation theory to linearize equation 2.1, and then Fourier transforming it, equation 2.2 results.

$$-i\omega m_s \vec{v}_s = q_s(\vec{E} + \frac{\vec{v}_s}{c} \times \vec{B}_0) \tag{2.2}$$

Since one form of Gauss's Law is:

$$\vec{\nabla} \cdot \vec{E} = 4\pi(\rho - \vec{\nabla} \cdot \vec{P}) = 4\pi\left(\sum_s n_s q_s - \vec{\nabla} \cdot (\overleftrightarrow{\chi}_s \cdot \vec{E})\right) \tag{2.3}$$

the solution of Equation 2.2 leads to the susceptibility, $\overleftrightarrow{\chi}_s$, for each species. The susceptibility is related to the dielectric tensor, $\overleftrightarrow{\varepsilon}$,

$$\overleftrightarrow{\varepsilon} = \begin{pmatrix} \varepsilon_\perp & -i\varepsilon_x & 0 \\ i\varepsilon_x & \varepsilon_\perp & 0 \\ 0 & 0 & \varepsilon_\parallel \end{pmatrix} \text{ where: } \varepsilon_\perp = 1 - \sum_s \frac{\omega_{p_s}^2}{\omega^2 - \Omega_s^2}\,,\ \varepsilon_x = \sum_s \frac{\varepsilon_s \omega_{p_s}}{\omega} \frac{\omega_{p_s}^2}{\omega^2 - \Omega_s^2}\,,$$
$$\varepsilon_\parallel = 1 - \frac{\omega_p^2}{\omega^2}\,,\ \varepsilon_s = \pm 1 \text{ for ions/electrons,}$$
$$\Omega_s = |\frac{q_s B}{m_s c}|\,,\ \omega_{p_s} = \frac{4\pi n_s e^2}{m_s}\,,\ \omega_p = \sum_s \omega_{p_s} \tag{2.4}$$

by

$$\overleftrightarrow{\varepsilon} = \overleftrightarrow{1} + \sum_s \overleftrightarrow{\chi}_s \tag{2.5}$$

Here, Ω_s is the cyclotron frequency and ω_{p_s} is the plasma frequency for a given species. To find the dispersion tensor, two of Maxwell's equations:

$$\vec{\nabla} \times \vec{B} = \frac{1}{c}\frac{\partial \vec{D}}{\partial t} \tag{2.6}$$

$$\vec{\nabla} \times \vec{E} = -\frac{1}{c}\frac{\partial \vec{B}}{\partial t} \tag{2.7}$$

are linearized, Fourier transformed, and combined to obtain:

$$\overleftrightarrow{D} = \overleftrightarrow{\varepsilon} - n^2(\overleftrightarrow{I} - \hat{k}\hat{k}) \text{ where: } \; n = \frac{kc}{\omega}\,, \; \hat{k} = \sin\theta\hat{x} + \cos\theta\hat{z} \tag{2.8}$$

The wavevector is $\hat{k}$ and the angle that the wavevector makes with respect to the background magnetic field is θ. The dielectric tensor is then used to get the dispersion tensor, $\overleftrightarrow{D}$, using equation 2.8. This leads to the dispersion tensor:

$$\overleftrightarrow{D} = \begin{pmatrix} \varepsilon_\perp - n^2\cos^2\theta & -i\varepsilon_x & n^2\cos^2\theta\sin\theta \\ i\varepsilon_x & \varepsilon_\perp - n^2 & 0 \\ n^2\cos^2\theta\sin\theta & 0 & \varepsilon_\parallel - n^2 \end{pmatrix} \tag{2.9}$$

The eigenmodes of the dispersion tensor give the modes of waves that are allowed to propagate. These can be found by taking the determinant of Equation 2.9. This leads to an equation:

$$\begin{aligned} An^4 + Bn^2 + C = 0 \;\text{ where: }\; & A = \varepsilon_\perp \sin^2\theta + \varepsilon_\parallel \cos^2\theta \\ & B = (\varepsilon_\perp^2 - \varepsilon_x^2)\cos^2\theta + \varepsilon_\perp\varepsilon_\parallel(1+\cos^2\theta) \\ & C = \varepsilon_\parallel(\varepsilon_\perp^2 - \varepsilon_x^2) \end{aligned} \tag{2.10}$$

that is quadratic in n^2 which can be solved for $n(k,\theta)$ or $\omega(k_\parallel, k_\perp)$.

Equation 2.10 is plotted for cases of parallel and perpendicular propagation, in Figures 2.2 and 2.3 respectively, for a plasma consisting of only equal numbers of protons and electrons.

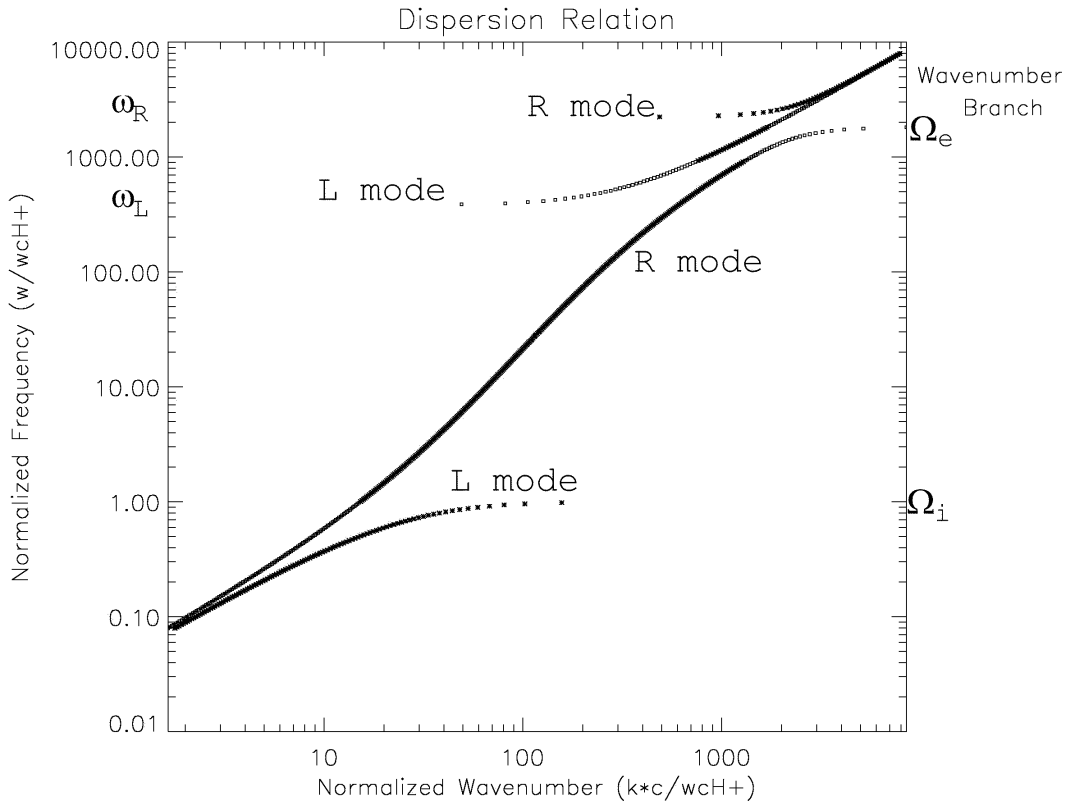

Figure 2.2: The parallel linear dispersion relation for a cold magnetized plasma with one species each of electrons and protons. The most common wave modes are labeled.

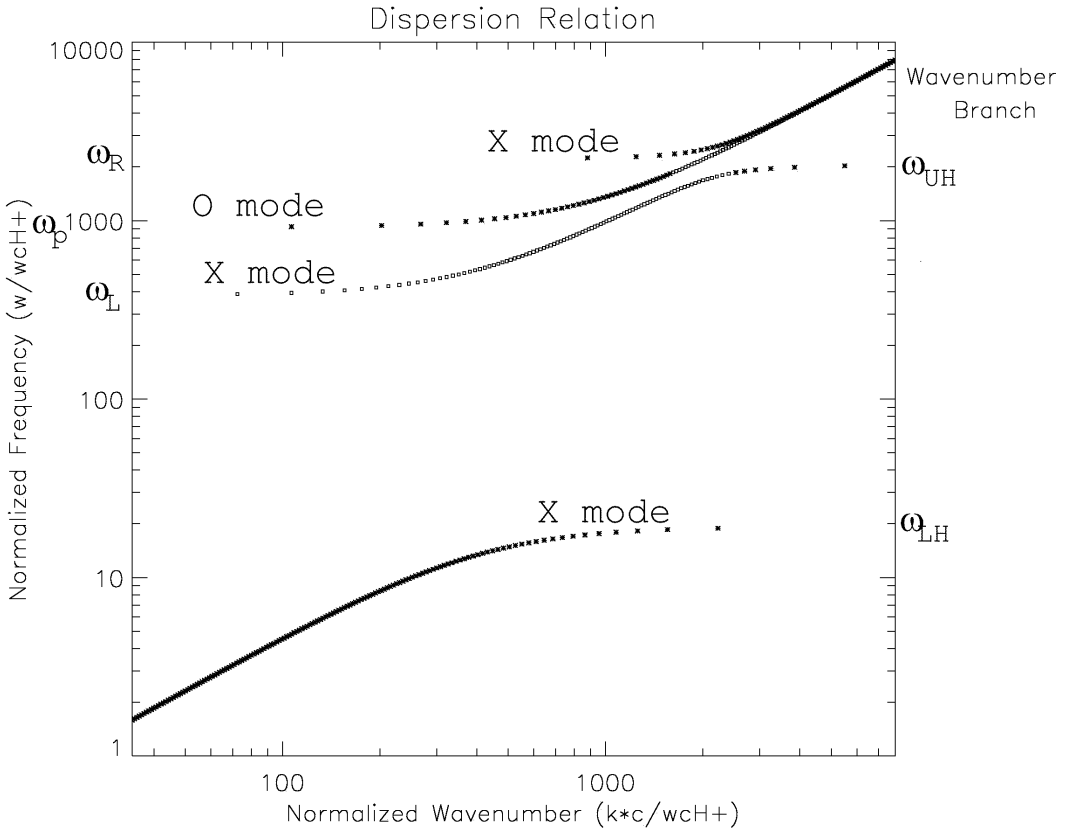

Figure 2.3: The perpendicular linear dispersion relation for a cold magnetized plasma with one species of each of electrons and protons. The most common wave modes are labeled.

These cases were chosen because they show some of the basic plasma wave modes that are often observed in the magnetosphere.

The polarization of the parallel propagating modes is either left (L) or right (R) circular polarization, and two of these modes have resonances at the ion (Ω_i) and electron cyclotron (Ω_e) frequencies. The higher frequency right and left modes have cutoffs (reflection points) at the right $\left(\omega_r = \frac{1}{2}\left(\Omega_e + \sqrt{\Omega_e^2 + 4\omega_p^2}\right)\right)$ and left $\left(\omega_l = \frac{1}{2}\left(-\Omega_e + \sqrt{\Omega_e^2 + 4\omega_p^2}\right)\right)$ frequencies, respectively. In the perpendicular propagation case the ordinary (O) mode has its electric field parallel to the background magnetic field. The O mode cuts off at the plasma frequency and it becomes a light wave at high frequencies. The extraordinary (X) modes, have elliptical polarization with the wave electric field perpendicular to the background magnetic field direction. The X modes have resonances at the upper $\left(\omega_{UH} = \sqrt{\omega_{p_e}^2 + \Omega_e^2}\right)$ and lower $\left(\omega_{LH} = \sqrt{\Omega_i^2 + \frac{\omega_{p_i}^2}{1+\frac{\omega_{p_e}^2}{\Omega_e^2}}}\right)$ hybrid frequencies, as well as cutoffs at the right and left frequencies. Notice that in both parallel and perpendicular cases there is a wave mode that has a resonance at the ion cyclotron frequency. These modes is also known as the EMIC mode. The EIC mode is not visible on these plots since its derivation requires a warm plasma.

Further information can be obtained from the dispersion relations for these waves. The ratio of electric to magnetic field for the waves can be obtained using $\vec{E} \cdot \overleftrightarrow{D}$, which is a form of the wave equation, E_y and E_z can be determined in terms of E_x. Then the magnetic field components can be found in terms of E_x using a linearized and Fourier transformed form of Faraday's Law:

$$\vec{B} = \hat{n} \times \vec{E} \tag{2.11}$$

These components can be combined to find the ratio of the total wave electric field strength to the wave magnetic field strength.

Species	n (cm^{-3})	V_{drift} (km s^1)	$T_\perp$ (eV)	$T_\parallel$ (eV)
e^- (beam)	0.50	6610	200	25
e^- (background)	0.10	0	10	10
H^+ (plasma sheet)	0.10	0	3740	5240
H^+	0.27	0	80	380
He^+	0.15	0	100	200
O^+	0.08	0	100	300

Table 2.1: Parameters obtained from FAST data and used for Figures 2.4 - 2.7

2.3.2 Application to FAST data

The cold dispersion relation can be used as a first approximation for studying the waves discussed in Section 2.1 and shown in Figure 2.1. The plasma characteristics present when these waves were observed [*Cattell et al.*, 1998] are given in the Table 2.1. The plasma in this case consisted of two populations of electrons, with one of these populations moving upward, and four species of ions. The waves of interest were propagating almost perpendicular to the background magnetic field at frequencies just above the ion cyclotron frequency. The cold dispersion relation and field strength ratios for waves, assuming that these waves are propagating at 80°, are shown in Figures 2.4 and 2.5. This dispersion relation shows that there is a resonance at the hydrogen cyclotron frequency, just as in the two component plasma case. The electric to magnetic field ratio is less than the speed of light at the region of interest near the hydrogen cyclotron frequency, which implies that the magnetic field is dominating in this region. These results are limited by the fact that the plasma involved is not actually cold. These limitations will be discussed when these cold dispersion relation results are compared to the kinetic dispersion relation results in Section 2.4.2.

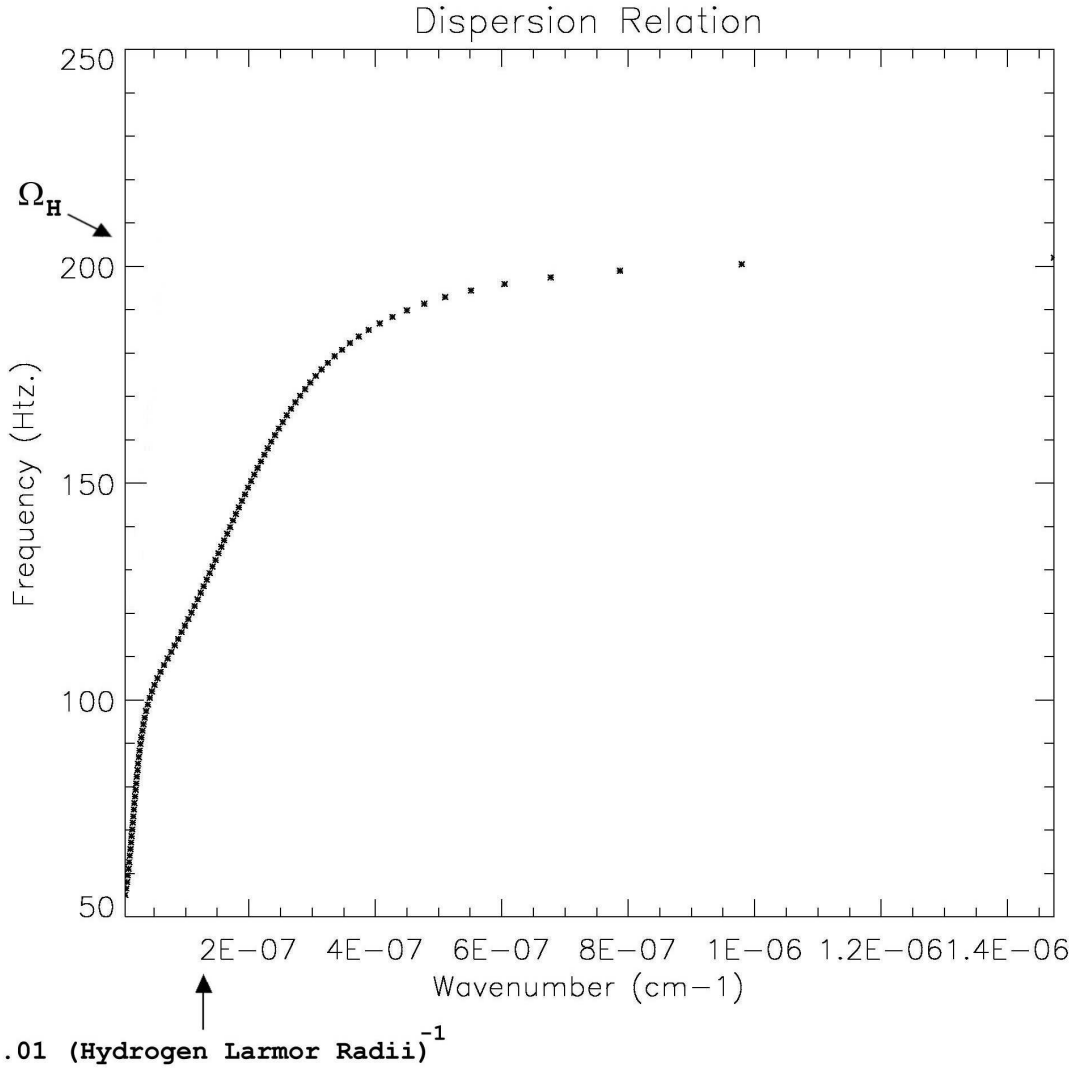

Figure 2.4: Shown above is the cold plasma linear dispersion relation for the FAST spacecraft event shown in Figure 2.1. This dispersion relation is for waves propagating at angle of 80° to the background magnetic field. This plot is obtained by solving equation 2.10. The plasma parameters used for this case are shown in Table 2.1. Compare this plot to Figure 2.6 which is the kinetic version of this dispersion relation.

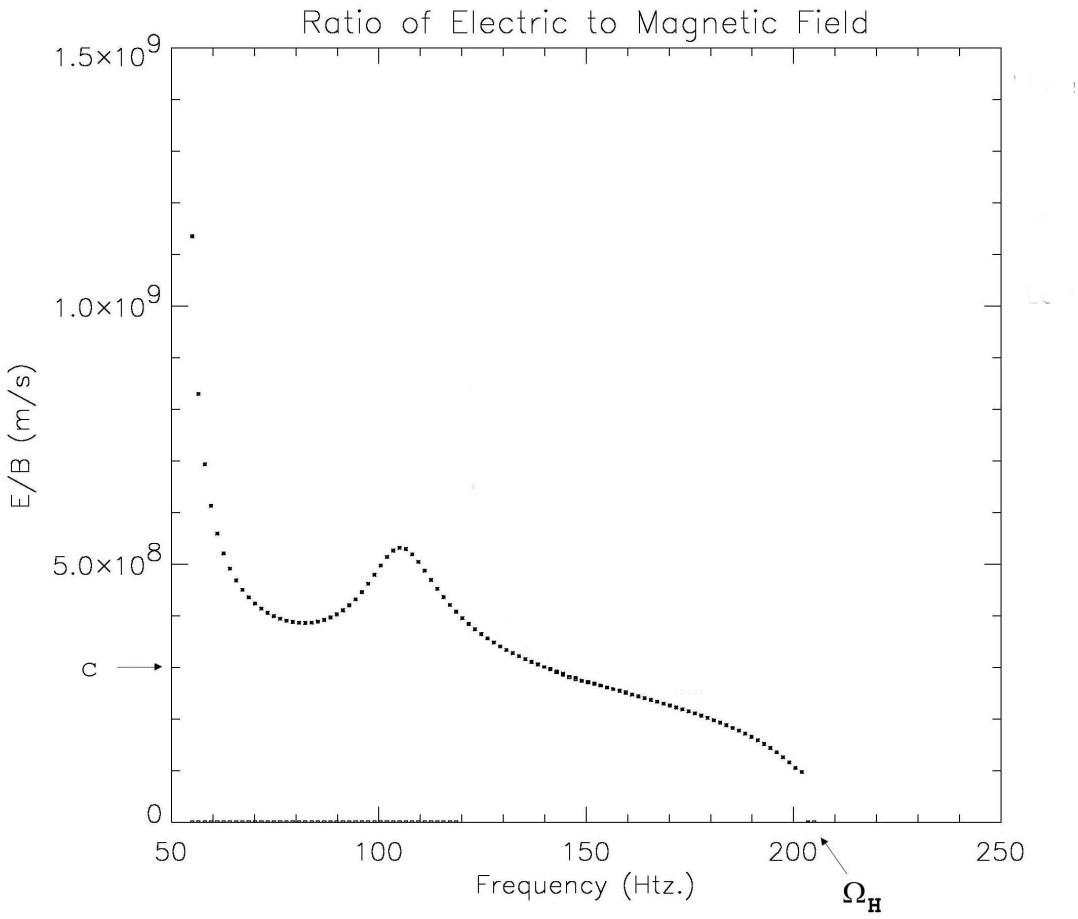

Figure 2.5: Shown above is the ratio of the electric field to magnetic field for the FAST spacecraft event shown in Figure 2.1. These results correspond to the dispersion relation results shown in Figure 2.4 and are for waves propagating at angle of 80°to the background magnetic field. Compare this plot to Figure 2.7 which is the kinetic version of this electric field to magnetic field ratio.

2.4 Kinetic Dispersion Relations

To overcome the limitations of the cold dispersion relation, the previous studies were redone with a computer code that uses a fully kinetic model to solve for the wave modes for hot plasmas [*Rönnmark*, 1983]. The kinetic approach used here assumes that the particle distributions are Maxwellian, or at least bi-Maxwellian (where $T_{\parallel} \neq T_{\perp}$). This approach better describes the wave modes observed because, as seen in Table 2.1, the plasma components are hot in the regions where these cyclotron waves are observed.

2.4.1 Theory

The method used to find the kinetic dispersion relation is very similar to the method for the cold case, though it is more complicated due to additional terms caused by the hot plasma. The susceptibilities, in this case, are derived by first linearizing and Fourier transforming Vlasov's equation:

$$\frac{\partial f_s}{\partial t} + \vec{v} \cdot \frac{\partial f_s}{\partial \vec{r}} + \frac{q_s}{m_s}(\vec{E} + \frac{\vec{v}}{c} \times \vec{B}) \cdot \frac{\partial f_s}{\partial \vec{v}} = 0 \text{ where } f_s \text{ is the distribution function} \quad (2.12)$$

This equation is solved by combining it with linearized and Fourier transformed forms of Maxwell's equations, and then integrating it [*Stix*, 1992]. The details, which are similar to the cold case though more mathematically complicated, will be omitted here.

2.4.2 Application to FAST data

Results of this fully kinetic approach, for the same FAST event as was shown using the cold dispersion relation, are shown in Figures 2.6 and 2.7. For the kinetic case, four different propagation angles between 75° and 90° are shown. In order to facilitate comparison between these plots and the previous plots, which are in different units, common locations are marked on each plot. By comparing the dispersion relation plots (Figures 2.4 and 2.6), it is evident that the kinetic dispersion relation differs from the cold dispersion relation. Both plots have the same general shape, with the wavenumber starting out low and leveling off at or near the

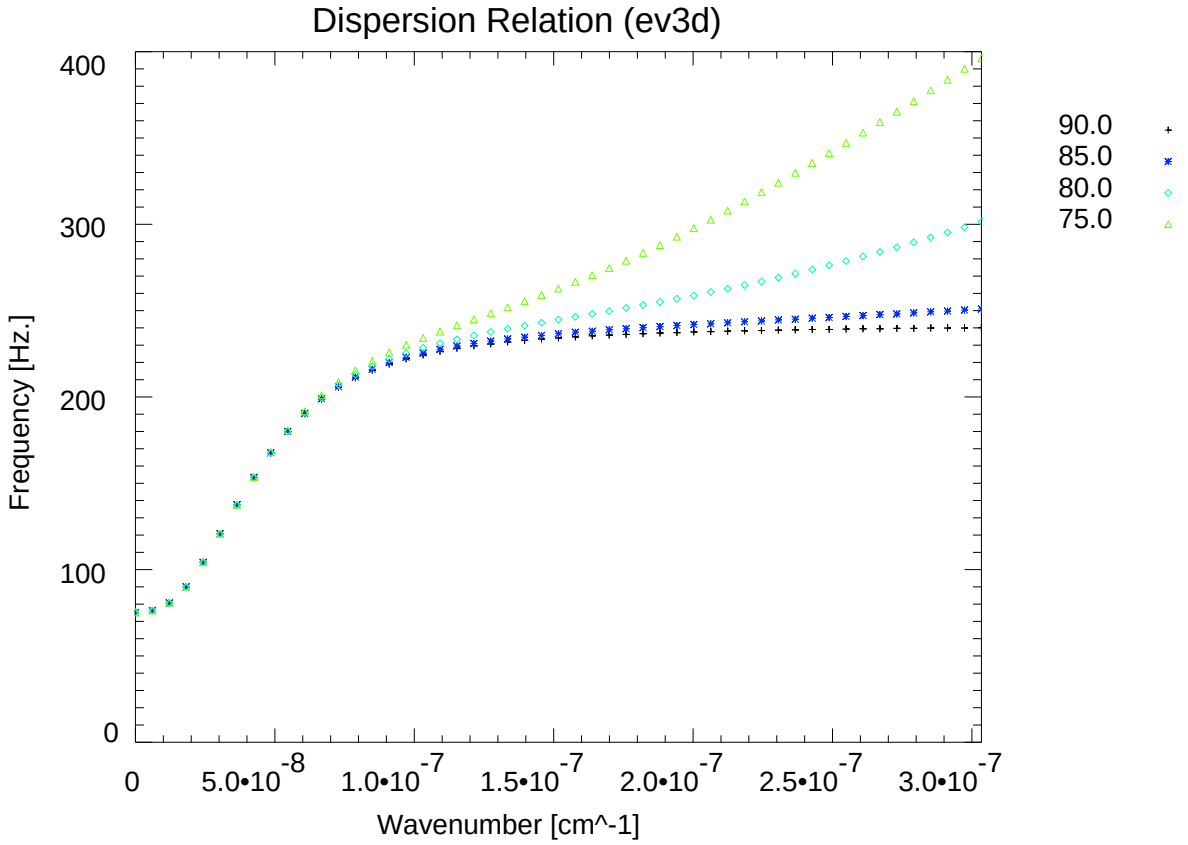

Figure 2.6: Shown above is the kinetic linear dispersion relation for the FAST spacecraft event shown in Figure 2.1. This plot is obtained by solving equation 2.12. The plasma parameters used for this case are shown in Table 2.1. Compare this plot to Figure 2.4 which is the cold plasma version of this dispersion relation.

hydrogen cyclotron frequency, but the kinetic dispersion relation plot levels out at a much lower wavenumber. Also, in the cold case the dispersion relation asymptotically approaches the hydrogen cyclotron frequency, while in the kinetic case, the dispersion relation levels off somewhat, but still continues to climb. This hints that this wave mode is a combination of the EMIC mode, which always has a frequency less than the ion cyclotron frequency, and the EIC mode which always has a frequency above the ion cyclotron frequency.

The differences in the ratios of electric to magnetic field are also dramatic (Figures 2.5 and 2.7). In the cold case, the ratio goes toward 0 as the frequency approaches the hydrogen cyclotron frequency, while in the kinetic case, the ratio has a maximum just above the hydrogen cyclotron frequency. The difference in the magnetic field characteristics of the wave mode is important because the ion cyclotron waves measured by FAST had magnetic fluctuations. *Chaston et al.* [1998] found that the ratio of electric to magnetic field $\geq$ c for cyclotron waves with frequencies above Ω_p, and $\leq$ c (roughly the Alfvèn speed) for waves with frequencies below Ω_p, which roughly agrees with the results shown in Figure 2.7.

An electromagnetic extension of EIC waves has been completed in order to help explain these observations of electromagnetic waves just above the ion cyclotron frequency [*Bergmann et al.*, 1998]. This formulation relies on adding the magnetic field component of the EIC wave as a perturbation on the usual formulation of the EIC wave. It should be noted that these generalized EIC waves are not the same as electromagnetic ion cyclotron (EMIC) waves, though this mode could be considered a combination of these two modes. The resulting generalization of EIC waves gives results that agree with the results shown in Figures 2.7 and 2.6. So these cyclotron waves that have magnetic components which are observed in the auroral acceleration region are likely generalized EIC waves and they can be studied using the kinetic dispersion relation, but not the cold dispersion relation. From these results it is clear that for particle populations that are hot, it is important to use the kinetic dispersion relation.

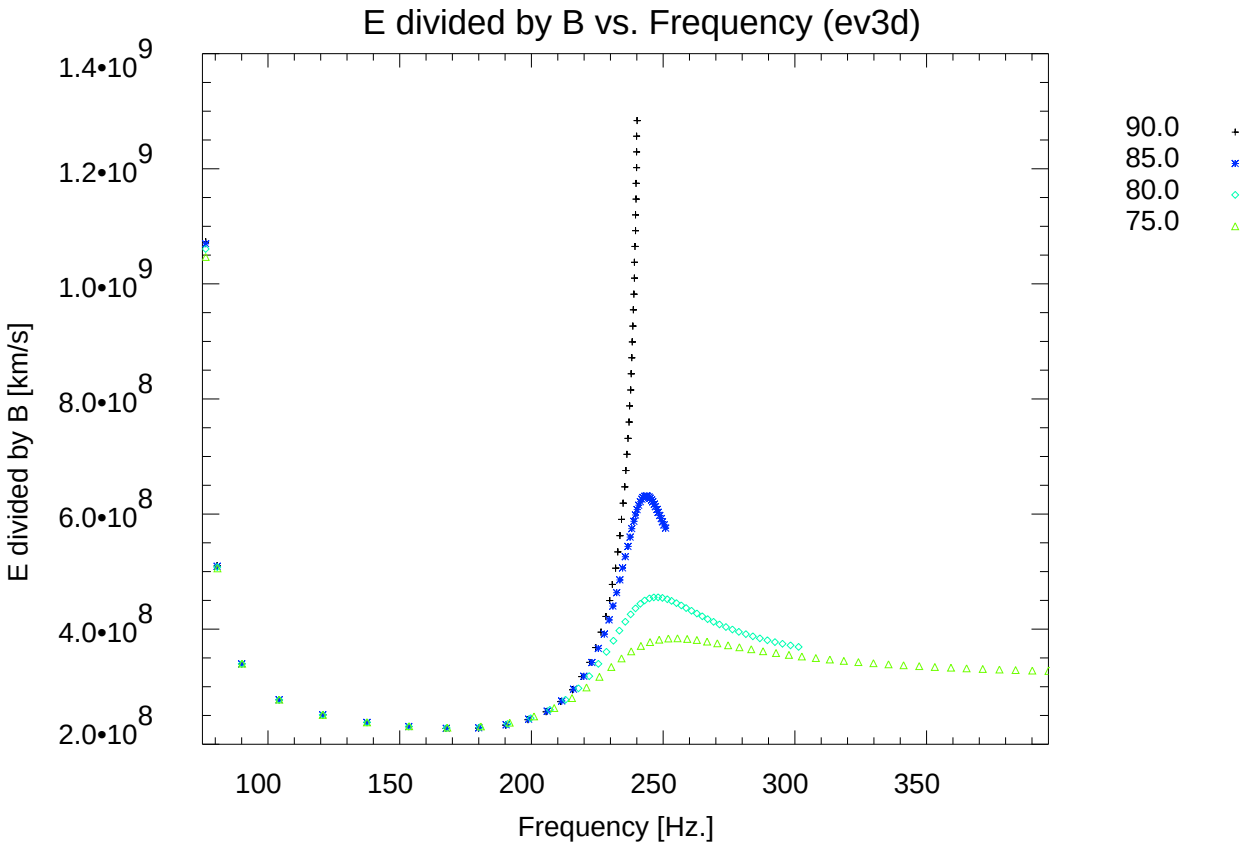

Figure 2.7: Shown above is the ratio of the electric field to magnetic field for the FAST spacecraft event shown in Figure 2.1. These results correspond to the dispersion relation results shown in Figure 2.6. Compare this plot to Figure 2.5 which is the cold plasma version of this electric field to magnetic field ratio.

2.5 Conclusion

Study of dispersion relations and the related information that dispersion relations provide is an important method for understanding waves observed in the magnetosphere. In the cold approximation of the dispersion relation, the temperature of the plasma particles is assumed to be 0. Because they are relatively easy to solve analytically, cold dispersion relations are useful for providing insight into basic plasma modes. They provide a good starting point for the study of linear plasma waves, but in many cases more detailed analysis requires that the full kinetic dispersion relation must be solved. In most cases, the kinetic dispersion relation must be solved numerically.

The comparison of cold and kinetic dispersion relations here is applied to FAST spacecraft observations of cyclotron waves in auroral zones. Waves with frequencies just above multiples of the ion cyclotron frequency were previously typically classified as EIC waves, since there were no observations of magnetic components of these waves. Recent FAST observations of these waves show magnetic components to these waves and theoretical work on these waves suggest that their mode is a magnetic generalization of EIC waves. The dispersion relation results presented here show that the cold dispersion relation is not sufficient to study these generalized EIC waves, since the ratio of electric to magnetic field does not match the observations. On the other hand, kinetic dispersion relation results do match the FAST observations as well as the theory for generalized EIC waves.

Chapter 3

Solitary Waves

Many types of nonlinear waves are seen in the magnetosphere. The focus of this paper will primarily be several related types of nonlinear waves. Solitary waves are structures that are not periodic and continuous. They often look like an isolated half or full wavelength of a linear wave mode. These waves are also observed as a depletion or increase of the plasma density that also coincides with a change in the electrostatic potential. These structures are not static and they propagate in the direction of the background magnetic field. An example of solitary wave observations from the Polar spacecraft is shown in Figure 1.1. The solitary waves are the isolated spikes in the electric field in the direction parallel to the magnetic field which are shown in the top panel of that figure.

Solitons are a specific type of solitary wave that have very definite properties; most importantly to this work, the amplitude is inversely proportional to the width. Another well known feature is that is that two solitons will pass through each other undisturbed. It is this particle-like characteristic of solitons that led to their name. The history of solitons is an interesting one [*Allen*, 1998], with solitons first being seen as water waves in canals in England [*Russell*, 1845]. The first theoretical work describing them was done by *Rayleigh* [1879], and *Korteweg and de Vries* [1895] found the first equation describing a solitary wave (the KdV equation).

Double layers consist of two layers of separated charge that have an electric field between them. Since these double layers are formed by separated charge, they must violate quasi-neutrality. Quasi-neutrality is the assumption that the charges in the plasma balance each other out leaving a plasma that is essentially neutral over macroscopic scales. The scale over which charges in a plasma are screened out by charges of the opposite sign is the Debye length $\left(\lambda_D = \sqrt{\frac{kT}{4\pi n e^2}}\right)$, though this assumes that the potential caused by the charge is small ($\phi \ll kT$). Strong double layers are structures where the electrostatic potential drop associated with charge separation is much larger than the temperatures or beam energies of the ions or electrons. In a strong double layer net charge builds up on scales $\gtrsim \lambda_D$ due to the flow of ions and electrons into the structure [*Borovsky*, 1992]. Weak double layers, on the other hand, have electrostatic potential drops which are less than the order of the electron temperature. A weak double layer is a solitary wave where the electric field signal of the pulse is asymmetric, so that there is a net potential drop across the structure. Electrostatic shocks are believed to be strong double layers which are aligned at an angle to the background magnetic field, instead of parallel to the field like double layers [*Ergun et al.*, 1998c; *McFadden et al.*, 1999a]. Since these structures are at oblique angle to the magnetic field, they accelerate particles both parallel and perpendicular to the background magnetic field.

One of the reasons that these nonlinear waves are of interest is because they might play a role in the parallel potential (which was mentioned in Section 1.2) that accelerates auroral electrons and ions. The structures mentioned above all cause electric fields parallel to the background magnetic field, so they all (except solitons which have symmetric potentials) could possibly sustain the parallel potential drop. The relationship of these waves to the parallel potential drop will be expanded on later in this chapter.

3.1 Solitary Structure Observations

The first double layers in the magnetosphere were observed by the S3-3 satellite [*Temerin et al.*, 1982] in the auroral acceleration region. These structures have since been classified as weak double layers since they had small potential amplitudes. The Viking satellite confirmed the S3-3 observations of double layers in approximately the same region [*Boström et al.*, 1988]. In addition, solitary waves with no net potential drop were also seen near these weak double layers. Furthermore, upward traveling ion beams were also seen at the same time the double layers were observed. Upward moving ions have been observed in this region at times when weak double layers were not observed, but these weak double layers have not been observed without upward traveling ions. This part of the observation has lead to the speculation that these weak double layers do not cause the parallel potential drop, though the fact that ion beams are observed more often than solitary waves is not very strong evidence concerning the effects of solitary waves. It is possible that solitary waves cause the ion beams, but have shorter lifetimes than ion beams causing them to be observed less often. Instead, it is thought more likely weak double layers are a result of the potential drop which also drives the ion beams, since the average net potential drop across weak double layers is small [*Mälkki et al.*, 1993]. Also, for weak double layers to be the cause of auroral acceleration there would have to be a large number of them along each auroral field line, and it is uncertain that enough of such structures have been observed [*Koskinen and Mälkki*, 1993]. Recent observations by the Polar spacecraft have added to the debate [*Mozer et al.*, 1997, see Figure 3.1]. This satellite, which was also making measurements in the auroral zone, has measured solitary structures that were much stronger than those previously measured. The parallel electric fields measured in some of these structures were 200 mV/m, while typical measurements for S3-3 were 10 mV/m. The largest structures seen in this case were not double layers, but were instead symmetric solitary waves. There were double layers present, but they were weak. More recently [*Mozer and Kletzing*, 1998], the Polar satellite has observed structures that have net potential drops with similar strong electric fields (Figure 3.2). These observations are believed to be strong double layers.

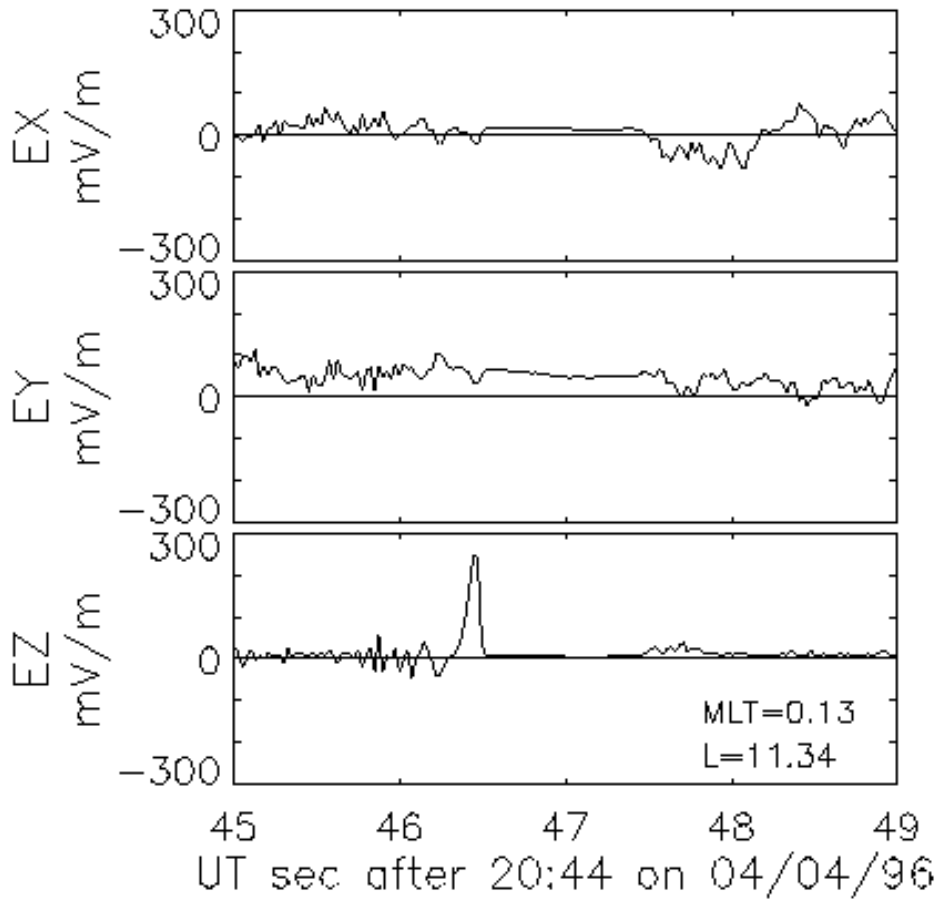

Figure 3.1: This figure from *Mozer and Kletzing* [1998] shows some very large double layer observed by the Polar spacecraft. The plot shows three components of the electric field in magnetic field aligned coordinates where the z component is along the magnetic field line, the x component is in the plane of the magnetic field line and pointing toward the earth, and the y component completes the orthogonal coordinate system.

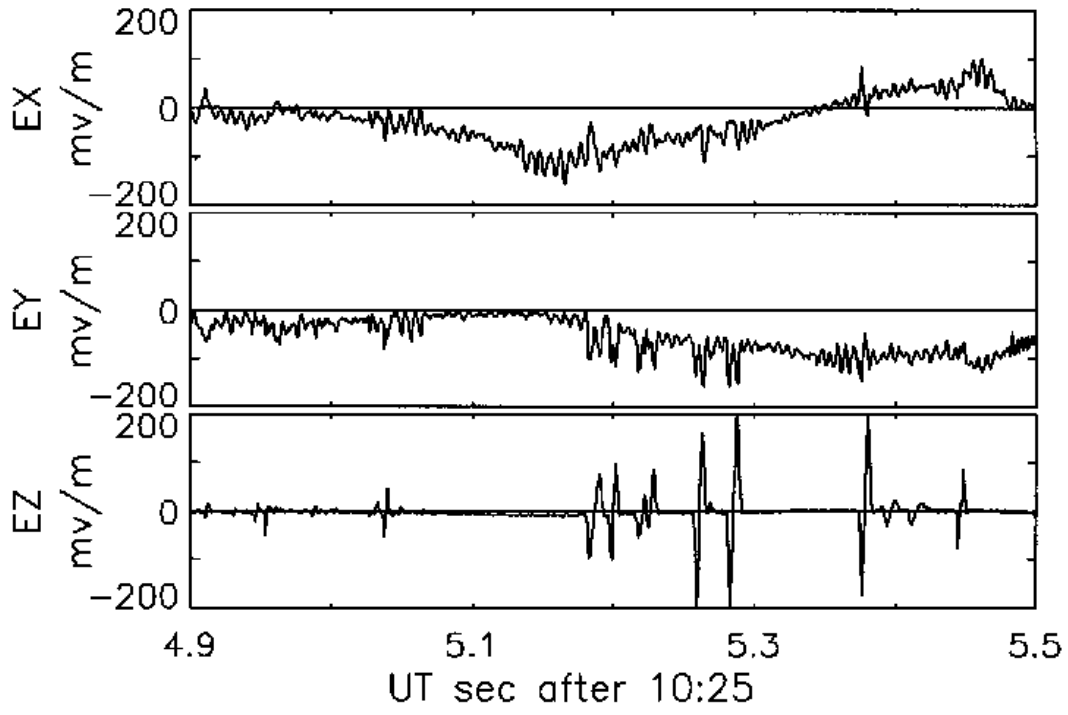

Figure 3.2: This figure from *Mozer et al.* [1997] shows some very large SWs observed by the Polar spacecraft. The plot shows three components of the electric field in the same magnetic field aligned coordinate system which is the as in Figure 3.1.

A strong double layer model would have one region where most of the acceleration is taking place, shooting the electrons down the field lines to cause the aurora (Figure 3.3). FAST has also made observations of strong double layers [*Ergun et al.*, 1998c; *McFadden et al.*, 1999a], including recent observations that suggest a oblique double layers (electrostatic shocks) at the boundary of auroral acceleration region and the ionosphere might cause between 5% and 50% of auroral acceleration [*Ergun et al.*, 2001]. Once again, it is unclear if enough strong double layers have been seen to account for the acceleration of all auroral particles, but it seems likely that they play a significant role.

Recent observations of solitary waves suggest that there are two classes of solitary waves: those associated with electron beams and those associated with ion beams [*Ergun et al.*, 1998b;

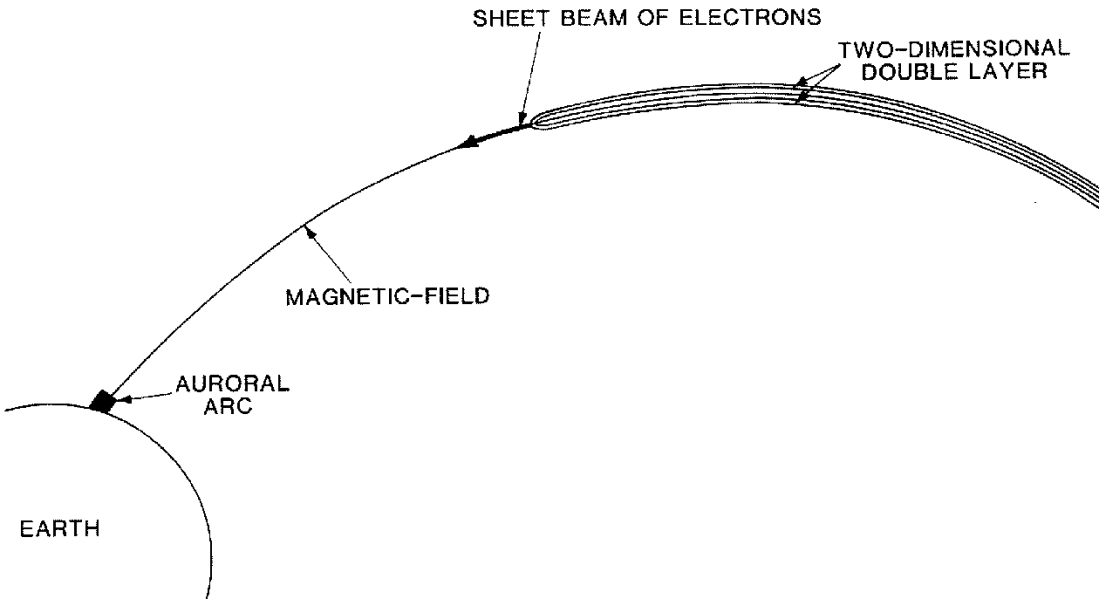

Figure 3.3: This diagram shows a double layer accelerating electrons down a magnetic field line to cause the aurora [From *Borovsky*, 1993].

Bounds et al., 1999]. Figure 3.4 compares the differences between electron and ion solitary waves. Solitary waves associated with electron beams tend to have higher speeds (1000's of km s^{-1}) than those associated with ion beams (100's of km s^{-1}). Solitary waves that are associated with ion beams were first observed in the auroral acceleration region by S3-3 [*Temerin et al.*, 1982], later by Viking [*Boström et al.*, 1988], and most recently by Fast Auroral Snapshot (FAST) [*McFadden et al.*, 2002] and Polar [*Mozer et al.*, 1997; *Bounds et al.*, 1999; *Dombeck et al.*, 2001]. Solitary waves associated with electrons beams (or presumed to be associated with electron beams due to the structures' speeds) were first observed by Geotail in the plasma sheet boundary layer and magnetotail [*Matsumoto et al.*, 1994; *Kojima et al.*, 1997; *Matsumoto et al.*, 1999]; later by FAST in the auroral acceleration region [*Ergun et al.*, 1998b, a] and cusp [*Yi-Jiun et al.*, 2001]; by Polar in the auroral acceleration region [*Mozer et al.*, 1997; *Bounds et al.*, 1999; *Dombeck et al.*, 2001], the cusp [*Cattell et al.*, 1999], the magnetopause [*Cattell et al.*, 2002], plasma sheet boundary layer [*Mozer et al.*, 1997; *Cattell et al.*,

1999; *Franz et al.*, 1998, 2000]; and by Wind in the bow shock [*Bale et al.*, 1998] and solar wind [*Mangeney et al.*, 1999].

S3-3's original observations of solitary waves in the auroral zone showed solitary waves with a lower limit of several volts of net potential drop across the structure and a lower limit of 50 km s^{-1} on the speeds of the structures. The structures had sizes both parallel and perpendicular to the background magnetic field of $\sim$ 40 λ_D, assuming that there was a cold background plasma population (which later results called into question) [*Temerin et al.*, 1982]. Viking's observations gave net potential drops up to 2-3 V and speeds of 5 - 50 km s^{-1}. Scale sizes were of the order of 50-100 m, with the perpendicular scale sizes being slightly greater than the parallel sizes. These scale sizes translated to $\sim$ 10 λ_D, including a cold electron population of 5 eV and 5 cm^{-3} [*Koskinen et al.*, 1990; *Mälkki et al.*, 1993] that was indicated by the Viking observations. The Viking observations have recently been caused into question due to the possibility that the technique used to find solitary wave velocities using Viking data is flawed [*McFadden et al.*, 2002].

A recent Polar spacecraft statistical study of ion-related solitary waves in the auroral acceleration region [*Dombeck et al.*, 2001] gives much different characteristics for these structures. The potential amplitude of the structures, $e\phi/kT_e$ (where e is the fundamental charge, ϕ is the potential amplitude, k is Boltzmann's constant, and T_e is the electron temperature), is $\sim$ 0.1, where kT_e is up to 1 keV (i.e., potentials of 10-100 V). The solitary wave speeds are between the hydrogen and oxygen beam speeds, in the same 75-300 km s^{-1} range as that found in a previous Polar study [*Bounds et al.*, 1999]. The scale size in the parallel direction is $\sim$ 10-20 λ_D, with the Debye length being $\sim$ 200 m in this case [*Dombeck et al.*, 2001]. Recent FAST observations have indicated that cold plasma densities are very low in the upward ion beam region [*Strangeway et al.*, 1998; *McFadden et al.*, 1999c]. The presence or absence of cold plasma populations in the regions where solitary waves are observed is important because it impacts which theories can be used to explain the observations of solitary waves.

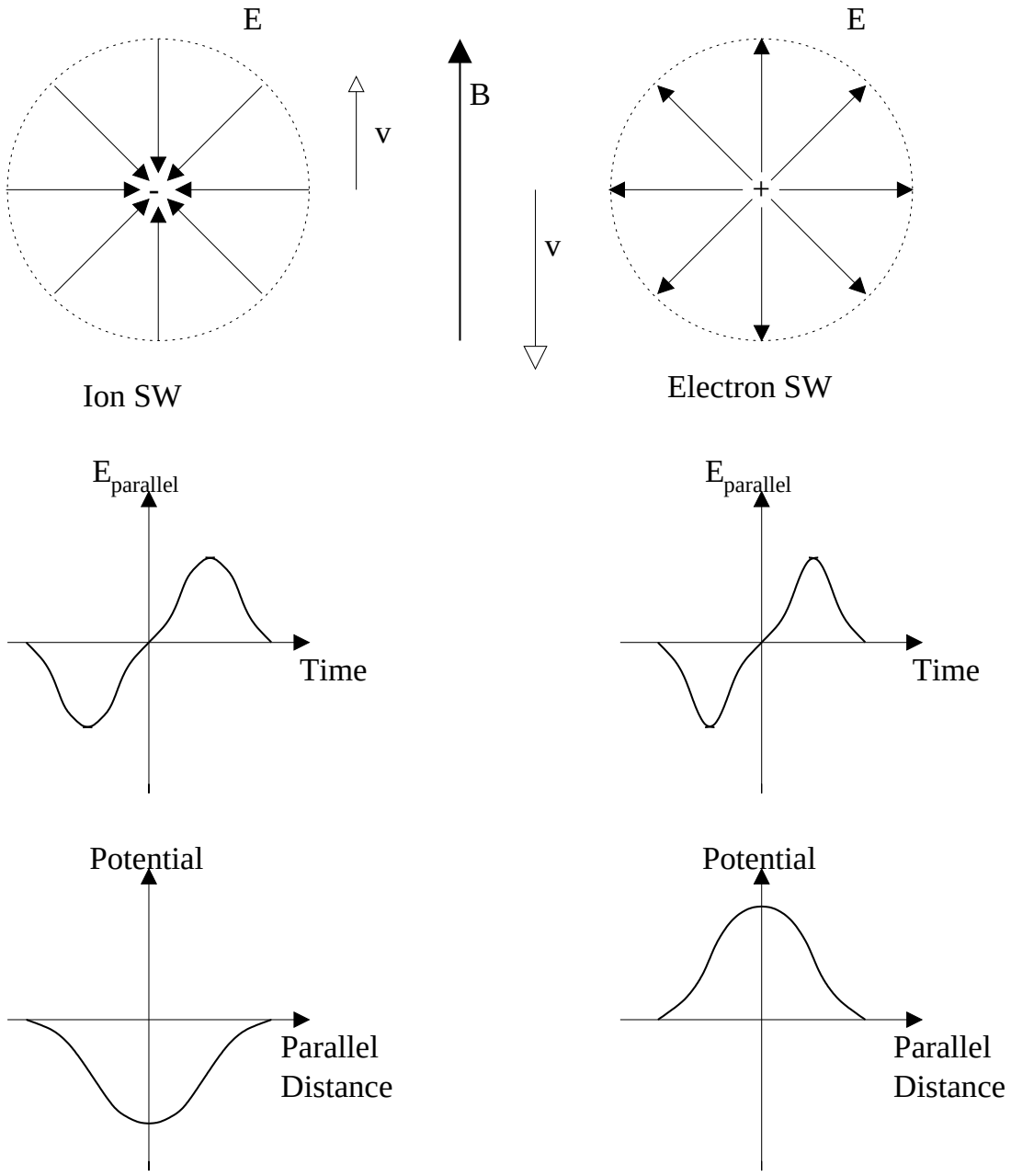

Figure 3.4: The figure above shows some characteristics of ion and electron solitary waves. Notice that the ion and electron solitary waves propagate in opposite directions in this diagram, as ion and electron beams in the auroral acceleration region typically travel in opposite directions.

3.2 Theories and Simulations of Solitary Structures

Solitary structures can be developed in a number of different ways in a plasma, but two commonly cited modes are ion or electron acoustic solitary waves and phase space holes. More background on these topics can be found in many sources including *Treumann and Baumjohann* [1997] and *Stix* [1992].

3.2.1 Ion Acoustic Solitary Waves

Solitary waves can be found from one dimensional analysis of ion acoustic waves, assuming that $T_e >> T_i$ [following *Sagdeev and Galeev*, 1969]. Since the electrons are hot they will have a Boltzmann distribution, while the cold ions will follow a simple continuity relation. These assumptions lead to the momentum equation:

$$m_i\left(\frac{\partial v}{\partial t} + v\frac{\partial v}{\partial x}\right) = -e\frac{\partial \Phi}{\partial t}, \tag{3.1}$$

the continuity equation:

$$\frac{\partial n_i}{\partial t} + \frac{\partial (v n_i)}{\partial x} = 0, \tag{3.2}$$

and Poisson's equation:

$$\frac{\partial^2 \Phi}{\partial x^2} = -4\pi e\left(n_o e^{\frac{e\Phi}{kT_e}} - n_i\right). \tag{3.3}$$

Then by assuming that the solution will be a traveling wave, so the dependence of all of the variables on x and t takes the form x - ut (where u is the solitary wave speed), these three equations can be combined into equation:

$$\frac{\partial^2 \Phi}{\partial x^2} = 4\pi n_o e\left(\frac{u}{\sqrt{u^2 - \frac{2e\Phi}{m_i}}} - e^{\frac{e\Phi}{kT_e}}\right). \tag{3.4}$$

Integrating this equation and determining the integration constant by requiring that the derivative of the potential goes to 0 when the potential goes to 0 gives:

$$\left(\frac{\partial \Phi}{\partial x}\right)^2 = 8\pi n_o\left(u m_i\sqrt{u^2 - \frac{2e\Phi}{m_i}} + kT_e e^{\frac{e\Phi}{kT_e}} - m_i u^2 - kT_e\right). \tag{3.5}$$

This equation can be written in the form of a potential equation:

$$\frac{1}{2}(\frac{\partial \Phi}{\partial x})^2 + U(\Phi) = 0, \tag{3.6}$$

where the potential term, $U(\Phi)$, is known as the Sagdeev Potential [*Sagdeev*, 1966]. One particularly interesting solution of this equation is the ion acoustic soliton solution:

$$\Phi = \frac{3z}{c_s}\,\mathrm{sech}^2\left(\sqrt{\frac{z}{2c_s}}\left(\frac{x-ut}{\lambda_{D_e}}\right)\right), \tag{3.7}$$

where c_s is the ion acoustic speed, λ_{D_e} is the Debye length, u is the wave speed, x is the coordinate in the direction of propagation, t is the time, and $z = \frac{u}{c_s} - 1$. Note that in this solution the amplitude of the soliton $\left(\frac{3x}{c_s}\right)$ is inversely proportional to the square of the width of the soliton $\left(\sqrt{\frac{2c_s}{z}}\right)$. This solution is plotted in Figure 3.5. Notice that in this case the potential returns to its original value, so that there is no net potential across the solitary wave. This case is not a double layer, but instead is a triple layer. There is a layer of electrons on each side, with the ions in the middle.

One major type of theory attempting to explain weak double layers involves the ion acoustic solitary waves. In these models, there are complications that allow the ion acoustic solitons to evolve into weak double layers. One such model involves an electron beam being reflected at a soliton [*Lotko*, 1983] (Figure 3.6). The reflected beam causes the potential to rise on the side it reflects off of, and subsequently the structure has a net potential change associated with it. So this model also relies on the currents that are seen in the auroral region, and the associated beams, as a source of free energy. The problems with these models include growth time scales that are much larger than the observed values [*Mälkki et al.*, 1989], as well as predicting that the potential amplitude is inversely proportional to width while the observations show that they are directly proportional [*Dombeck et al.*, 2001].

Ion acoustic solitons have been studied in the context of the auroral acceleration region in particle-in-cell (PIC) simulations since at least *Sato and Okuda* [1980], whose work was in 1-D. This work was extended to 2-D by *Barnes et al.* [1985] who found that weak double layers did not form unless the plasma was strongly magnetized ($\omega_{ce} > \omega_{pe}$). *Marchenko and Hudson*

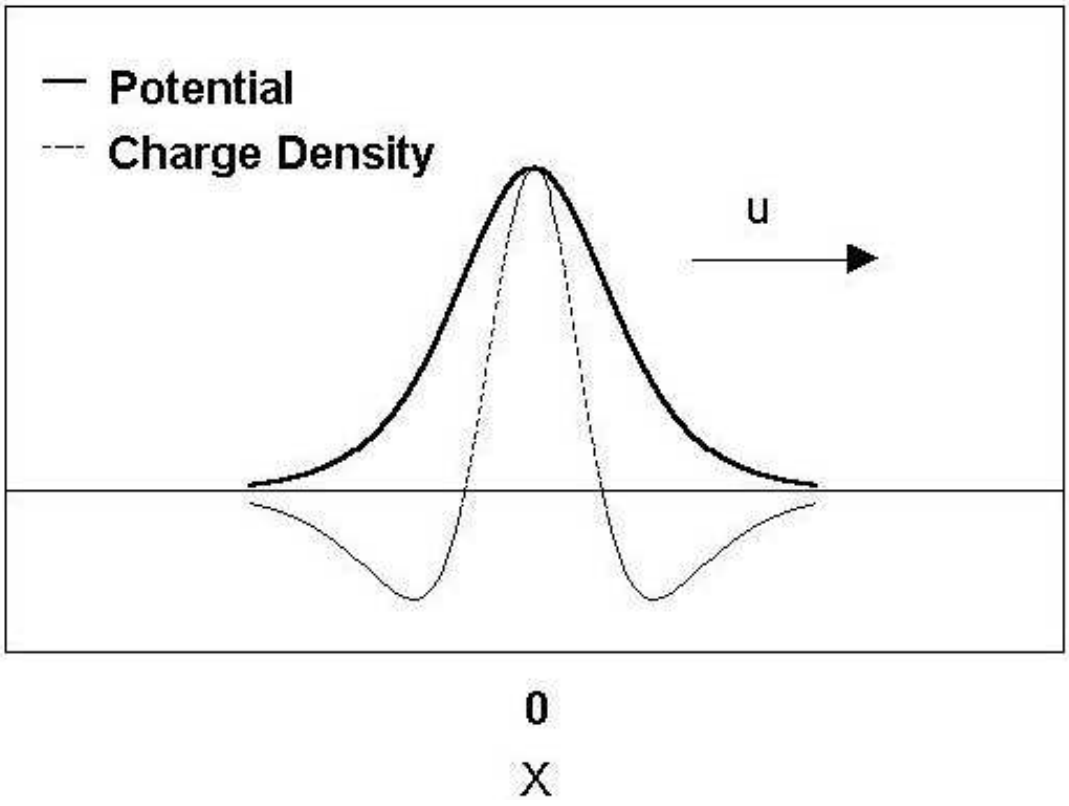

Figure 3.5: This diagram shows the relationship between the electric potential and the charge density for a soliton.

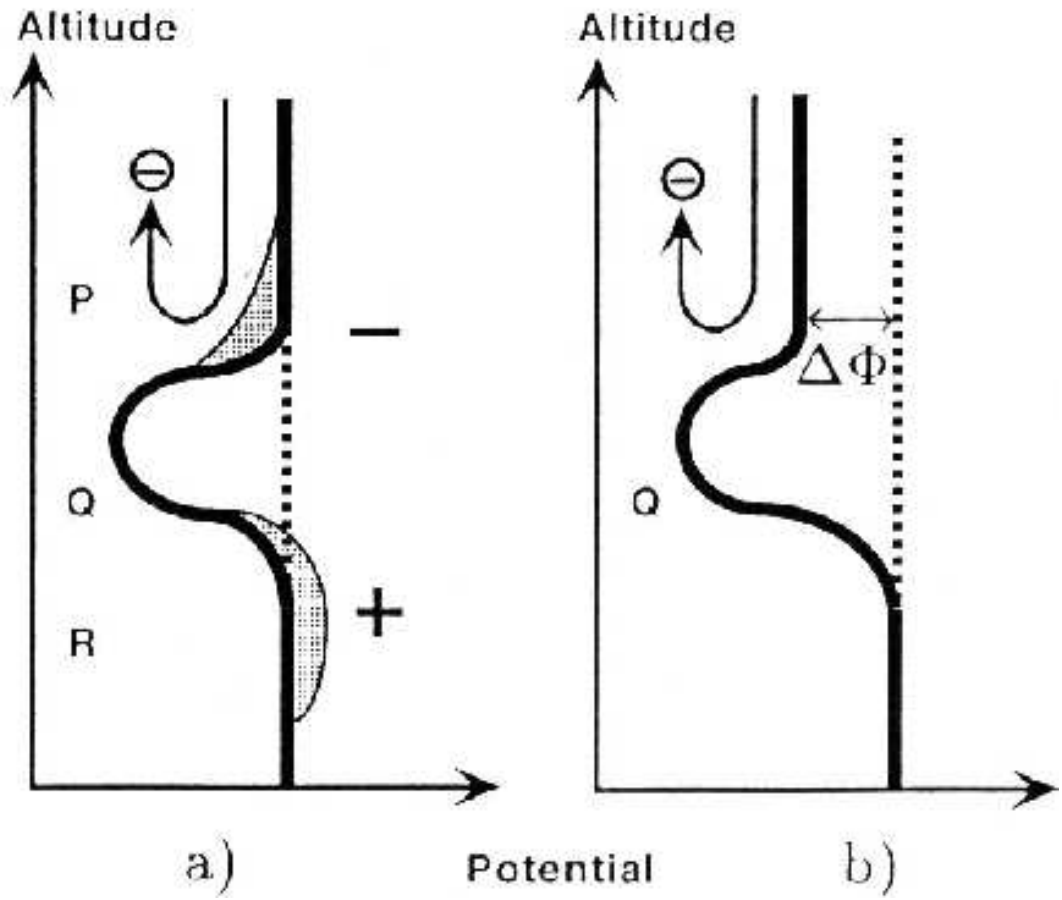

Figure 3.6: This figure shows a proposed mechanism for converting a soliton, which has no net potential drop, into a weak double layer, which has a net potential drop. The mechanism involves reflecting an electron beam off of one side of the soliton's potential structure, which would cause a charge buildup. This charge buildup leads to a net potential across the soliton [from *Eriksson and Boström*, 1993].

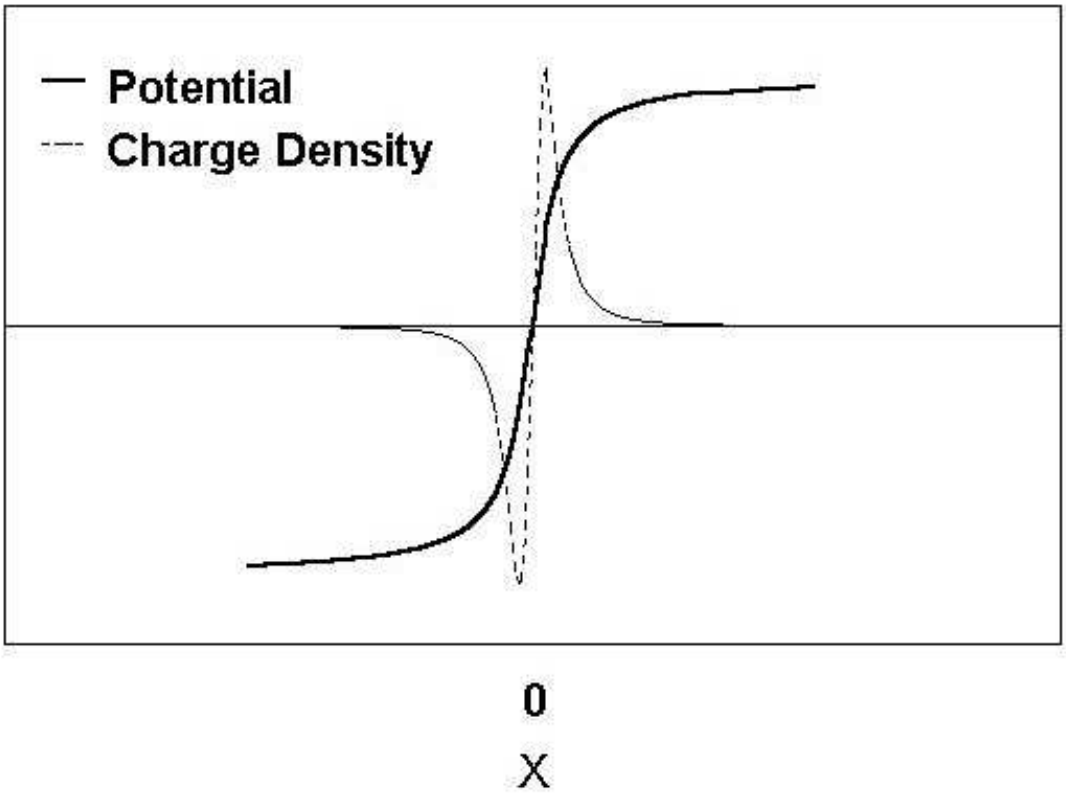

Figure 3.7: This diagram shows the relationship between the electric potential and the charge density for a double layer.

[1995] extended this work to explain the Viking spacecraft observations [*Boström and Anson*, 1988; *Eriksson et al.*, 1997] that solitary waves formed in regions dominated by cold plasma. Chapter 6 will extend this work to deal with plasma parameters consistent with FAST spacecraft observations, which sees little to no cold plasma in the auroral acceleration region [*McFadden et al.*, 1999c].

3.2.2 Strong Double Layers

Strong double layers (Figure 3.7) are separated regions of charge where the potential drop across the structure is greater than the electron temperature. The biggest strike against theories explaining the auroral potential drop through the use of strong double layers had been that strong enough electric fields are not often observed in the magnetosphere. According to [*Borovsky*, 1993], parallel electric fields of 500 mV/m would be required for strong double layers to be the source of the auroral acceleration. Electric fields of that order have been observed by Polar (See Figure 3.1). It is not clear if there are enough of them to support the auroral potential drop, though single large structures can support a significant fraction of the auroral potential drop [*Mozer et al.*, 1997]. FAST has also recently observed strong double layers [*Ergun et al.*, 2001, 2002], making it more likely that strong double layers support at least a portion of the auroral potential drop. Recent computational and theoretical work concerning these strong double layers, also suggest that they may be the source of electron phase space holes [*Newman et al.*, 2002].

3.2.3 Phase Space Holes

The other main type of theory explaining weak double layers involves Bernstein-Greene-Kruskal (BGK) phase space holes [*Bernstein et al.*, 1957]. BGK phase space hole models have been advanced to explain both ion beam related solitary waves [*Dupree*, 1982; *Tetreault*, 1988, 1991] and electron beam related solitary waves [*Muschietti et al.*, 1999a, b]. An explanation of ion phase space holes will be given here, though the explanation of electron phase space holes is quite similar. These models involve “holes” in the the ion distribution function when the electron population is drifting with respect to the ion population (Figure 3.8). These holes are originally caused by thermal fluctuations, but the holes grow and move towards the center of the distribution [*Tetreault*, 1991]. Physically this result can be explained by thinking of the holes as negative particles being repelled by the electrons. The size of the hole grows because the hole enters a phase region that is more densely populated. The electrostatic potential can be

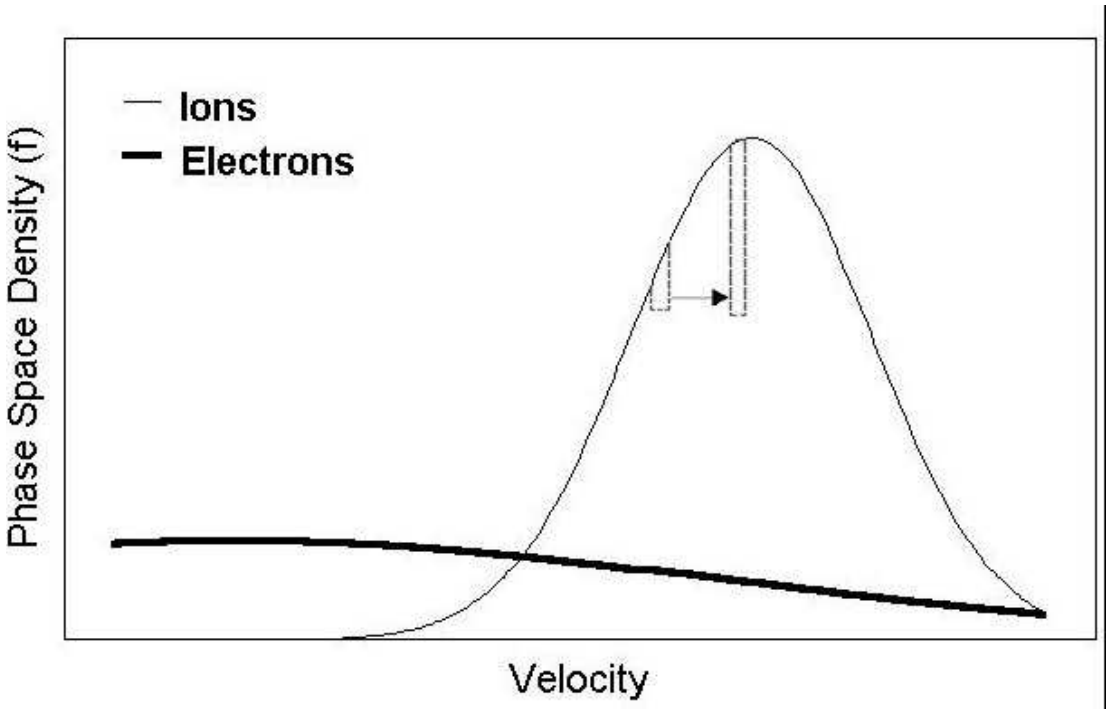

Figure 3.8: This diagram shows the development of an ion phase space hole. The phase space hole develops near the edge of the ion distribution function and then moves toward the center of the distribution and grows.

determined from this model using Poisson's equation, and the predicted potential drops can be quite large depending on the initial conditions for the hole. The drifting in these models is due to the field aligned currents, so once again the source of free energy is these currents. One of the advantages of BGK phase space holes is that they can form with any drift drift velocity. One of the most serious shortcomings of these hole models stems from the fact the theories have only been done in one dimension, and it is believed that perpendicular effects should be important. Also, these models don't usually account for the linear wave modes which are usually present near the weak double layers [*Koskinen et al.*, 1993], though *Tetreault* [1991] does mention the possibility of ion phase space holes being a source of electrostatic ion cyclotron waves.

Simulations involving electron phase space holes in the context of laboratory plasmas started with *Morse and Nielson* [1969]. Several groups have done simulations involving electron phase space holes in the magnetosphere, though no simulations focusing on magnetospheric ion phase space holes have been done. Geotail observations of electron solitary waves, which were originally referred to as broadband electrostatic noise (BEN), have lead to several attempts at simulations to explain the results [*Omura et al.*, 1994; *Matsumoto et al.*, 1994; *Krasovsky et al.*, 1997; *Omura et al.*, 1999]. *Muschietti et al.* [1999a] has looked at electron phase space holes by loading a particle simulation with a BGK stable solution for an electron phase space hole, and then following the evolution of these structures. *Singh* [2000] used a 1-D Vlasov code to simulate the electron solitary waves seen by FAST and found that an electron beam accelerated by a double layer would create electron holes, as well. *Oppenheim et al.* [2001] have done 2-D and 3-D PIC simulations of electron holes and found that the electron holes decay into whistler and lower hybrid waves.

3.3 Summary

Magnetospheric solitary waves, which are nonlinear structures most often observed in electric field measurements, have been observed throughout the magnetosphere by a variety of spacecraft. Several different types of solitary waves have been observed, including strong and weak double layers. Solitons are solitary waves that have symmetric potential profiles and in which the potential amplitude is inversely proportional to the width. Double layers are structures that are named due to their two regions of separated charge which cause these structures to sustain a net potential drop. Strong double layers have a net potential drop larger than the electron temperature, while weak double layers do not. The observations of solitary waves have been further divided based on the type of particle beams they are generally seen with. Electron solitary waves are generally observed along with electron beams throughout the magnetosphere and have propagation speeds on the order of thousands of kilometers per second. Ion solitary waves are observed along with ion beams only in the auroral acceleration region and have speeds of hundreds of kilometers per second. One theory used to explain the origin of ion solitary waves is that they evolve from ion acoustic solitons into weak double layers due to the influence of electron beams. BGK phase space holes are another theory which is used to explain both ion and electron solitary waves. Simulations studying both ion and electron solitary waves have been performed.

Weak double layers have been observed frequently, but there is no model which explains them satisfactorily. It is also uncertain how they fit into auroral acceleration. At the present time, it is unclear whether they cause auroral acceleration or they are just a side effect of other processes which drive the auroral acceleration [*Eriksson and Boström*, 1993]. Much of the remainder of the work presented here will discuss our simulations and observations of solitary waves and how they fit into the physics of the auroral acceleration region.

Chapter 4

Solitary Wave Simulation Methods

This chapter begins with a brief discussion of computational techniques used to study plasmas in space physics. Then particle-in-cell (PIC) simulation techniques and ES2, the code used here, are described in more detail. This discussion includes description of the normalizations and initial conditions used to apply ES2 to the problem of ion solitary waves in the auroral zone.

4.1 Plasma Simulations

Several different schemes for numerically studying plasma behavior are commonly used including magnetohydrodynamic (MHD), PIC, and Vlasov codes. Each of these methods is suitable for studying plasma behavior in specific plasma regimes.

MHD codes work by modeling the plasma as a fluid. In fact, the equations that are the basis for MHD simulations are the same as those used to study fluids, with the addition of terms and equations that deal with the response of plasma particles to electromagnetic fields. Typically, MHD simulations treat the plasma as a single fluid with the plasma characteristics averaged over all particle species. Due to the averaging over plasma species that goes into MHD models, they are well suited for studying large-scale plasma processes and processes involving bulk

motion of plasma, but not as suitable for resolving small-scale processes where the details of particle behavior are important. Also, some type of distribution for the particles must be assumed in MHD codes so that the particle distributions can be averaged over. Equilibrium or near equilibrium distributions are usually assumed and therefore MHD codes are harder to apply to situations where non-equilibrium particle distributions are expected [*MacNeice*, 1995].

PIC codes involve modeling the plasma through use of pseudo-particles. Due to computational constraints, the pseudo-particles in a PIC simulation rarely have a one-to-one correspondence to real particles in the plasma. Instead, one pseudo-particle will represent the behavior of many real particles. In a PIC simulation, the positions and velocities of the particles are tracked, but for the purposes of considering the forces on the particles, the simulation is divided into a grid. Forces on particles are calculated by averaging the relevant plasma properties (such as charge density) over each grid cell, and calculating the forces caused by each cell on each particle. Since the particle nature of the plasma is preserved, PIC are well-suited for examining non-equilibrium processes. One drawback of PIC simulations is that the need to have pseudo-particles represent more than one real particle causes PIC simulations to be noisier than the real processes they simulate [*Birdsall and Langdon*, 1991].

Vlasov codes involve solving Vlasov's equation (Equation 2.12) directly for the plasma to be studied. Solving Vlasov's equation is a difficult numerical problem since it involves directly integrating the particle distributions, which often forces Vlasov's codes to be one dimensional, where MHD and PIC codes are most often two or three dimensional. The major advantage of Vlasov codes over PIC codes is that since the distribution function is solved completely, Vlasov codes tend to have much less noise than PIC codes [*MacNeice*, 1995]. So, Vlasov codes are often the preferred choice when the numerical expense of Vlasov codes can be justified, although that is not the most common case.

4.2 ES2 and Solitary Waves

The simulations presented here were performed using ES2 (which is based on ES1 - a 1-dimensional code described in *Birdsall and Langdon* [1991]), a 2.5-dimensional, electrostatic PIC code with periodic boundary conditions. The reasons why these characteristics of ES2 make it an appropriate simulation code to use to study ion solitary waves in the auroral acceleration region are described in this section.

First, it is a PIC code, and the non-quasi-neutral nature of the charge separation in solitary waves makes solitary waves a phenomenon that could not be studied with an MHD code, but can be studied with a particle code. PIC are preferred over Vlasov codes for examining solitary waves because of the difficulty of multi-dimensional Vlasov codes and the fact that extra noise of PIC codes might actually be beneficial in providing a source for solitary waves.

Using a 2.5-dimensional (2.5D means that the code is 2D in physical space and 3D in velocity space) simulation, such as ES2, to study solitary waves is an appropriate trade off between computational difficulty and adherence to physical reality. A 1D code would not be very useful for studying solitary waves since the properties and behavior of these structures is expected to be quite different in the direction parallel to the background magnetic field from the directions perpendicular to the magnetic field. Conversely, the two directions perpendicular to the background magnetic field are expected to be interchangeable, so the increase of computational expense of a fully 3-dimensional simulation is not necessarily warranted. The Lorentz force in a 2.5D simulation includes terms dependent on the velocity in the third dimension. So third dimension is added in velocity space since it adds comparatively little computational expense, but increases the accuracy of the simulation.

Solitary waves are often observed with no magnetic field fluctuations corresponding to the electric field fluctuations. Magnetic field fluctuations have been observed with some electron solitary waves, but the fluctuations were small and consistent with being caused by the motion of the charge of the solitary structure [*Ergun et al.*, 1998b]. So the computational price incurred by using an electromagnetic simulation would not be justified due to the essentially electrostatic

nature of the solitary waves. Therefore, the use of an electrostatic simulation, like ES2, to study solitary waves is appropriate.

Using periodic boundary conditions to study solitary waves is sensible for several reasons. First, it is expected that the direction perpendicular to the background magnetic field will be fairly uniform. Since little motion of particles is expected in the perpendicular direction, allowing the particles to wrap around the simulation to the opposite side after crossing one of the perpendicular boundaries is not likely to cause any problems. Periodic boundary conditions in the direction parallel to the magnetic field are more difficult to defend, but still preferable to the alternatives. The solitary wave structures move at high speeds parallel to the magnetic field, so, with periodic boundary conditions, not only do individual particles wrap around from one end of the simulation grid to the other, but so do entire solitary waves. This wrap around of solitary waves is partially justified by the fact that multiple solitary waves are observed along the length of a magnetic field line. So a single solitary wave in a system with periodic boundary conditions can play the role of multiple solitary waves spread along a magnetic field line. As an alternative, the boundary conditions in the parallel direction could be open. This would require re-injecting "fresh" particles whenever simulation particles crossed one of the parallel boundaries. In order to study solitary waves with a simulation with open boundary conditions a simulation box that is very long compared to its width would be required. It is much more reasonable numerically to use periodic boundary conditions in the parallel direction and to keep in mind that the effective length of our simulation grid is increased by the wrap around of particles from one end of the simulation to the other.

4.3 Computational Details

Electrostatic PIC codes, such as ES2, work by solving Poisson's equation:

$$\nabla^2 \Phi = -4\pi\rho(\vec{x}) \tag{4.1}$$

where Φ is the electric potential and $\rho(x)$ is the charge density. To start the simulation run, the particles are loaded into random locations. Then the charge density caused by the initial positions of the particles is calculated by adding the charge density contribution of each particle to the appropriate grid cells. From the charge density and Equation 4.1, the electric field is determined:

$$E(x) = -\nabla\Phi \; . \tag{4.2}$$

From the electric field, the force on particle i is:

$$F_i = q_i E(x_i) = m_i a_i \; . \tag{4.3}$$

Then the particles are allowed to move under the influence of the electric field, and any other forces (such as the background magnetic field), for a time step Δt. Next, new positions are calculated for the particles, and from the new positions, a new charge density is calculated. This process is then iterated for the remainder of the time steps left in the simulation run.

Several factors complicate the simple overview of ES2's computational scheme presented above. One of these complications is the computation of the charge density [*Birdsall and Langdon*, 1991]. The charge density must be calculated for all of the discrete points on the grid from the continuous measurements of particle position. The simplest method of weighting, known as zeroth-order weighting, is to assign the entire value of a particle's charge to the grid point that it is closest to. This scheme is fast computationally, but it leads to problems with noise since a small change in a particle's position can change which grid point its charge is included with for calculating the charge density.

To reduce the noise due to weighting, some simulations such as ES2 use first-order weighting [*Lawson and Gray*, 1989]. In first-order weighting, the charge of a particle is effectively spread over an entire grid box. If the particle's position happens to lie exactly on a grid point when the charge density is calculated, then all of its charge is added to that grid point. Otherwise, the charge is spread over two or more grid points. The particles in this weighting are effectively clouds of charge instead of discrete points of charge. First-order weighting is more

expensive computationally, but it leads to less noisy simulations, which aids in interpretation of the results.

Analogous considerations go into the weighting of electric fields for the determination of forces on particles. In zeroth-order weighting for forces, the electric field at the grid point nearest the particle is used to determine the force on the particle. As with charge density, zeroth-order forces lead to noise. So first-order force weighting, where the electric field for a particle is determined by interpolating the electric fields from the nearby grid points, is used in ES2.

The method of solving Equation 4.1 is also more complicated. Instead of solving the finite difference version of that equation, the equation is Fourier transformed [*Lawson and Gray*, 1989]. This simplifies the solution, since in k-space the Poisson's equation (Equation 4.1 in 2D becomes:

$$\phi(\vec{k}) = -\frac{\rho(\vec{k})}{k^2}\,, \tag{4.4}$$

which is easier to solve. Equations 4.2 and 4.3 are also solved in k-space. The results are then transformed back into normal space for analysis.

4.4 Normalizations

Since computers deal in unitless numbers, it is the responsibility of the programmer to keep track of the units. Some simulation programs are designed to use certain sets of units and require input and output in those units. Other programs, such as ES2, use normalized values for input and output. Normalized units simplify the equations that go into the simulation and make more obvious the variety of scales for which the simulation results are valid. Normalization schemes other than the one described below can be used with ES2 without changing the code itself, but this scheme has a lot of useful qualities. This scheme is the same as the one used by *Marchenko and Hudson* [1995] and others.

The most basic normalizations in ES2 are of time and space. In this study, the distance scale

was set to the electron Debye length and the time-scale was set to the inverse of the electron plasma frequency which leads to very convenient results. If there is more than one electron species, the convention of having normalizations based on the first electron species in the input file is used. With this type of normalization, velocities were normalized by the electron thermal velocity:

$$\lambda_{De}\omega_{pe} = \sqrt{\frac{T_e}{m_e}} = v_{tex}, \tag{4.5}$$

where $\lambda_{De}, \omega_{pe}, T_e, m_e$, and v_{tex} are the electron Debye length, plasma species, temperature, mass, and thermal speed respectively.

Some of the other normalizations come from the definitions of the plasma and cyclotron frequency in the 2-D case. The plasma frequency,

$${\omega_p}^2 = \frac{n_0 * q^2}{(m * lx * ly)} = \frac{n_0 * qm * q}{(lx * ly)}, \tag{4.6}$$

is used in ES2 to find out what the charge is, since only qm (charge divided by mass) is used as input. Also, this equation is used to determine the plasma frequencies for species other than the first electron species:

$$\omega_{pj} = \sqrt{\frac{n_{0j}}{n_{0e}}\frac{qm_j}{qm_e}}. \tag{4.7}$$

In this equation j is the species in question, and e is the first electron species.

The cyclotron frequency,

$$\Omega_c = \frac{ZeB_0}{mc} = qm * b, \tag{4.8}$$

where e is the fundamental charge, Z is the number of charges, B_0 is the background magnetic field, and b the normalized magnetic field, leads to the normalization for b. Since qm is set to -1 for electrons, if sign is ignored, $\Omega_e = b$. So b has units of inverse time, and it can be normalized with respect to the plasma frequency. Another way to consider the normalization for b is to regard it in terms of the ratio of electron cyclotron frequency to electron plasma frequency [*Lawson and Gray*, 1989]. This is an informative way of thinking about the problem

since the electron cyclotron frequency is a measurable quantity and it gives some insight into how magnetized the electrons in a given system are.

Electric field is normalized based on $T_e/e * L$, or electron temperature divided by electron charge divided by length of the box. So basically, the potential drop across the box is chosen and then divided by the size of the box.

For setting the other velocities in the simulation, the fact that all of the velocities scale as v_{tex} of the first electron species is used. Then :

$$v_{tjk} = \sqrt{\frac{qm_j T_{jk}}{T_{ex}}} \tag{4.9}$$

where j is a given species, and k is a coordinate. This works for thermal speeds and drift (beam) speeds. Also, charge (q) can be used as a check to make sure ω_p was set correctly. All singly ionized species should have the same absolute value for charge.

4.5 Initial Conditions

The initial particle populations are crucial initial conditions for these simulations of solitary waves. The details of the particle populations used are described in Chapter 6, but the general idea is to model the particles observed in as few particle populations as possible. For these purposes, the electrons were modeled with one background population, while the ions were modeled with one or more equal energy beam populations to follow the observations of the auroral acceleration region [*McFadden et al.*, 1999c]. For the ion beams, all the simulations have at least a hydrogen beam population, while some of the runs add an oxygen or oxygen and helium beam populations. Variations in the number of particle populations were included to simulate the variety of particle populations observed, which ranged from particle distributions almost completely dominated by hydrogen, to particle distributions with large fractions of oxygen and helium.

The other physically interesting initial condition is the electric field that is applied across the simulation box along the magnetic field direction. This electric field is included in the

simulation to simulate the quasi-static electric field that is observed in the auroral acceleration region. This electric field also is a source of free energy for the particles in the simulation.

4.6 Summary

PIC simulation codes, along with magnetohydrodynamic and Vlasov codes, are often used to simulate plasma processes. PIC codes, due to their particle nature, are well suited for studying non-equilibrium processes like solitary waves. ES2, the simulation program used in this study, is a 2.5-dimensional, electrostatic PIC code. In ES2, the spatial and time simulation parameters are normalized in terms of the Debye length and the inverse of the electron plasma frequency, which leads to convenient normalizations for most other simulation parameters. The simulations presented here include one electron population and one or more ion population, as well as an applied electric field along the magnetic field, in order to simulate the observed plasma conditions in the upward field aligned current portion of the auroral acceleration region.

Chapter 5

Solitary Wave Observation Methods

The Polar spacecraft was used to make observations of solitary waves for this study. This chapter introduces the Polar spacecraft and its instruments. First, the history and purpose of the Polar spacecraft are introduced. Next Polar's orbit and its precession are discussed. Then the Electric Field Instrument (EFI), which is the main instrument used in this study for studying solitary waves, is discussed, along with how this instrument is used to study solitary waves. Finally, the selection criteria used for determining solitary waves is explained.

5.1 The Polar Spacecraft

The Polar spacecraft was launched February 24, 1996. It has a variety of instruments including field instruments, imagers, and particle detectors (see Table 5.1 [*Russell*, 1995]). The main source of data for this study is from the EFI, though some magnetic field (MFE) and particle data (TIMAS and Hydra) are used as well.

The majority of Polar's instruments are mounted on or near the central body of the spacecraft. An exception is the EFI which consists of 3 sets of perpendicular booms that have electric field detectors at their ends. 2 of the sets of booms are flexible wire booms which require spin for stability, so Polar rotates with a period of 6 seconds. Polar's spin plane is set so that it is

Field Instruments	
Electric Fields Instrument	EFI
Magnetic Fields Experiment	MFE
Plasma Waves Instrument	PWI
Imagers	
Ultraviolet Imager	UVI
Visible Imaging System	VIS
Polar Ionospheric X-Ray Imaging Experiment	PIXIE
Particle Detectors	
Toroidal Imaging Mass-Angle Spectrograph	TIMAS
Thermal Ion Dynamics Experiment	TIDE
Plasma Source Investigation	PSI
Charge and Mass Magnetospheric Ion Composition Experiment	CAMMICE
Comprehensive Energetic-Particle Pitch-Angle Distribution	CEPPAD
Source/Loss Cone Energetic Particle Spectrometer	SEPS
Hot Plasma Analyzer	Hydra

Table 5.1: Polar Spacecraft's Instruments

the same as the plane of Polar's orbit, which means that Polar "cartwheels" through its orbit [*Harten and Clark*, 1995].

5.1.1 Polar's Orbit

Polar has a polar orbit with a period of 18 hours, an inclination angle of 85 degrees, an apogee of 9 R_E, and a perigee of 1.8 R_E geocentric (see Figure 5.1). Due to the precession of its orbit, Polar has made observations in a wide variety of regions of the magnetosphere. Polar's orbit has precession in two different directions due to different effects.

One of the precessions of Polar's orbit is actually due to the motion of the Earth around the Sun. The plane of Polar's orbit stays relatively constant in inertial coordinate systems fixed to the Earth, but rotates in common magnetospheric coordinate systems (GSE, GSM, SM) that are set by the line between the Sun and the Earth. Since the line from the Sun to the Earth revolves with a period of one year, the position of the orbit will precess with that same period. Due to this precession, the orbit will sweep through all local times twice per year. The coverage of local times is doubled because each orbit covers two local times - i.e. an orbit that covers the noon local time at one end of the orbit would cover midnight at the other end of the orbit.

The other type of precession of Polar's orbit causes the perigee of the orbit to slowly precess toward the equatorial plane. The orbit precesses roughly 16 degrees a year. In the beginning of the Polar mission, the perigee and apogee were almost directly over the poles. Currently perigee is just above the equatorial plane and it will cross the equatorial plane August 27, 2002.

The precession of Polar's orbit is beneficial for using the spacecraft to study the magnetosphere, since the regions that the spacecraft observes varies throughout the lifetime of the spacecraft. In the case of our observations of solitary waves, Polar's orbit has allowed observations solitary waves in the southern auroral acceleration region [*Bounds et al.*, 1999; *Dombeck et al.*, 2001], the plasma sheet boundary layer [*Cattell et al.*, 1998; *Franz et al.*, 1998], the cusp [*Cattell et al.*, 1999], the magnetopause [*Cattell et al.*, 2002], and the bow shock (see Figure 1.2).

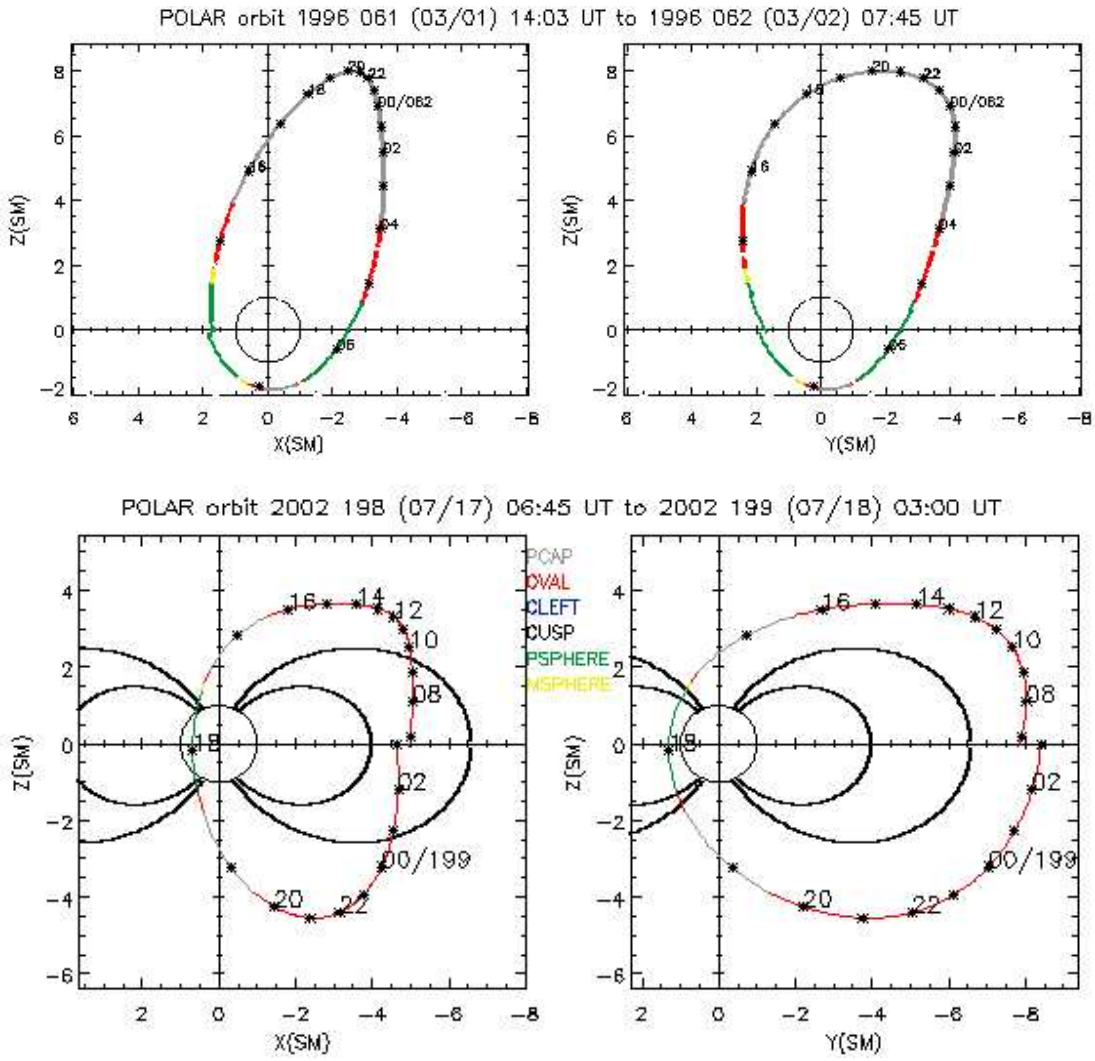

Figure 5.1: This figure shows Polar's orbit on March 1-2, 1996 (top panels), near the beginning of its mission and on July 17-18, 2002 (bottom panels). The left panels show the projection of Polar's orbit into the XZ plane in Solar Magnetic (SM) coordinates and the right panels show the projections into the YZ plane. Solar Magnetic coordinates have the z direction defined by the direction of Earth's magnetic field and the y direction perpendicular to the Earth-Sun line and pointing in the direction of dusk.The colors of the lines in the plots correspond to the region of space Polar is in or the region of the ionosphere the magnetic field line Polar is on maps to. Grey corresponds to the polar cap, red to the auroral oval, blue to cleft, black to the cusp, green to the plasmasphere, and yellow to elsewhere in the magnetosphere. Plots courtesy of *Peredo and Boardsen* [1996].

5.1.2 Polar's Electric Field Instrument

The Electric Field Instrument (EFI) is a fully 3-dimensional electric field detector. It consists of 3 sets of mutually orthogonal booms the ends of which are 20 cm spherical Langmuir probes (see Figure 5.2). The 4 electric field booms in the spin plane are long wires (100 m and 130m long tip-to-tip), while the 2 booms parallel to the spin of the spacecraft are short, rigid stacers (13.8 m tip-to-tip) [*Harvey et al.*, 1995]. The potential difference between the spacecraft and each probe is measured. Pairs of measurements from opposing booms are combined to determine the electric field. EFI can sample the electric field from DC to over 20 kHz. Electric fields between $\sim$ 0.02 and 1000 mV/m can be detected. EFI measurements of spacecraft potential can also be used to infer number densities from $\sim$ 0.01 to 100 cm^{-3}. EFI includes a 2 MB burst memory which allows the instrument to take short bursts of higher time resolution data. The data can then be slowly sent to the ground over the course of Polar's orbit. Several different time resolutions are available for this burst data, although most bursts have been taken at 1.6 or 8 kHz and the majority of the data presented herein is 8 kHz burst data [*Harvey et al.*, 1995]. Burst mode allows Polar to make observations of interesting electric field structures that would not otherwise be possible due to telemetry constraints. The availability of high-time resolution electric field is critical for the study of solitary waves since they are such fast moving structures that some of the structures are under-sampled even at this time resolution. Figure 5.4 shows an example of 8kHz burst data containing solitary waves from February 4, 1997. The data in this figure was taken at low altitude in the auroral acceleration region.

5.1.3 Polar's Particle Detectors

Data from two of Polar's particle detectors is used in this study: Hydra [*Scudder and et al.*, 1995] and TIMAS (Toroidal Imaging Mass-Angle Spectrograph) [*Shelley and et al.*, 1995]. The Hydra instrument measures both ion and electron populations. Hydra consists of six pairs of electrostatic analyzers (ESAs). The ESAs have a curved channel with charged plates on each side and a particle detector at the end of the channel. The charge on the plates is varied, which

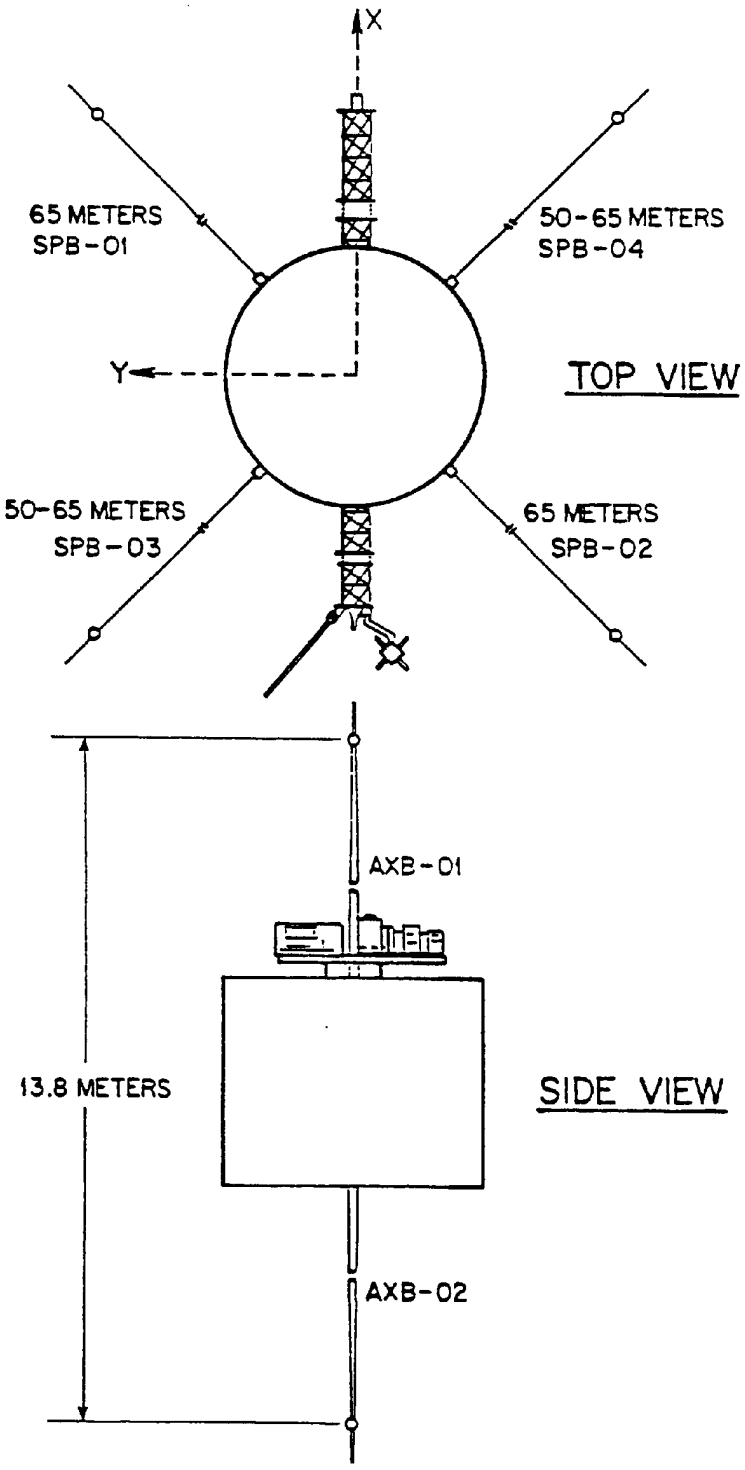

Figure 5.2: This figure from *Harvey et al.* [1995] shows the layout of EFI. The top diagram shows the spin plane and the bottom diagram show the spin axis.

changes which particles can navigate the channel and strike the detector. The six pairs of ESAs allow Hydra to measure the particle distribution. Each ESA has an 8 degree by 8 degree field of view and detects an energy range from 12 eV to 18 keV. Each energy sweep takes 1.15 s and the instrument alternates between ion and electron sweeps.

TIMAS is a spectrograph which simultaneously measures the angle and mass distributions of charges from 1 to over 32 atomic mass units per fundamental charge (amu/e). The field of view of the instrument is 315 degrees by 10 degrees, with measurements being sampled over 20 ms. The spin of Polar allows the spacecraft to sample almost the entire four pi solid angle within a half spin periodic (3 s). The 3-D ion distributions that TIMAS measures have energy ranges from 15 eV/e up to 32 KeV/e.

5.2 Solitary Wave Detection

For the study of solitary waves, EFI is used as an interferometer (see Figure 5.3). To determine the solitary wave speed, the time difference between when the solitary wave is observed by the two probes is calculated. For the purposes of this calculation, the average potential of the two perpendicular booms is used as the reference potential instead of the potential of the spacecraft. This alternate potential is used because the spacecraft would react differently to the potential of the solitary wave than the spherical probes [*Dombeck et al.*, 2001]. Potential measurements for a current biased electric field instrument such as EFI are complicated by interactions with the plasma:

$$\phi_i = E_i \cdot d_i + (V_i - V_s) \tag{5.1}$$

where the subscript i stands for any of EFI's six spherical probes, ϕ_i is the voltage measurement for the probe, $E_i \cdot d_i$ is the plasma potential difference between the spacecraft and the probe, and V_s is the floating potentials of the spacecraft, V_i is the bias voltage of the probe [*Johnson*, 2002; *Mozer*, 1973]. The floating potential of a conductor in a plasma is the potential that the conductor floats at relative to the plasma due to the collection of particles by the conductor.

The spacecraft floating potential changes depending on the plasma density, so it would change during the passage of a solitary wave due to the density fluctuations within a solitary wave. The variation of the spacecraft potential leads to the need for the more stable reference potential, ϕ_c, described below. The probe bias potentials are roughly constant during the passage of the solitary wave and are roughly the same for all of the probes.

The average of the voltage measurements of the perpendicular booms is a as suitable proxy for spacecraft voltage because the perpendicular electric fields that they measure are expected to cancel since the perpendicular scale size of the solitary waves is expected to be larger than the probe separation distance:

$$\begin{aligned}\phi_c &= \frac{1}{2}(\phi_1 + \phi_2) \\ &= \frac{1}{2}(E_1 \cdot d_1 + E_2 \cdot d_2 + V_1 + V_2 - 2V_s) \\ &= \frac{1}{2}(V_1 + V_2) - V_s,\end{aligned} \tag{5.2}$$

where ϕ_c is the central potential. The central potential is then used to find the signals that will be used to analyze the solitary waves:

$$\begin{aligned}\phi_+ &= \phi_3 - \phi_c \\ &= E_3 \cdot d_3 + (V_3 - V_s) - \frac{1}{2}(V_1 + V_2) + V_s \\ &= E_3 \cdot d_3 + (V_3) - \frac{1}{2}(V_1 + V_2) \\ &= E_3 \cdot d_3\end{aligned} \tag{5.3}$$

$$\begin{aligned}\phi_- &= \phi_c - \phi_4 \\ &= \frac{1}{2}(V_1 + V_2) - V_s + E_4 \cdot d_4 - (V_4 - V_s) \\ &= \frac{1}{2}(V_1 + V_2) - V_4 - E_4 \cdot d_4 \\ &= -E_4 \cdot d_4\end{aligned} \tag{5.4}$$

where ϕ_+ is the signal seen by the near boom, and ϕ_- is the signal seen by the far boom. In both the equations above the probe bias potentials cancel because all of the probe bias potentials

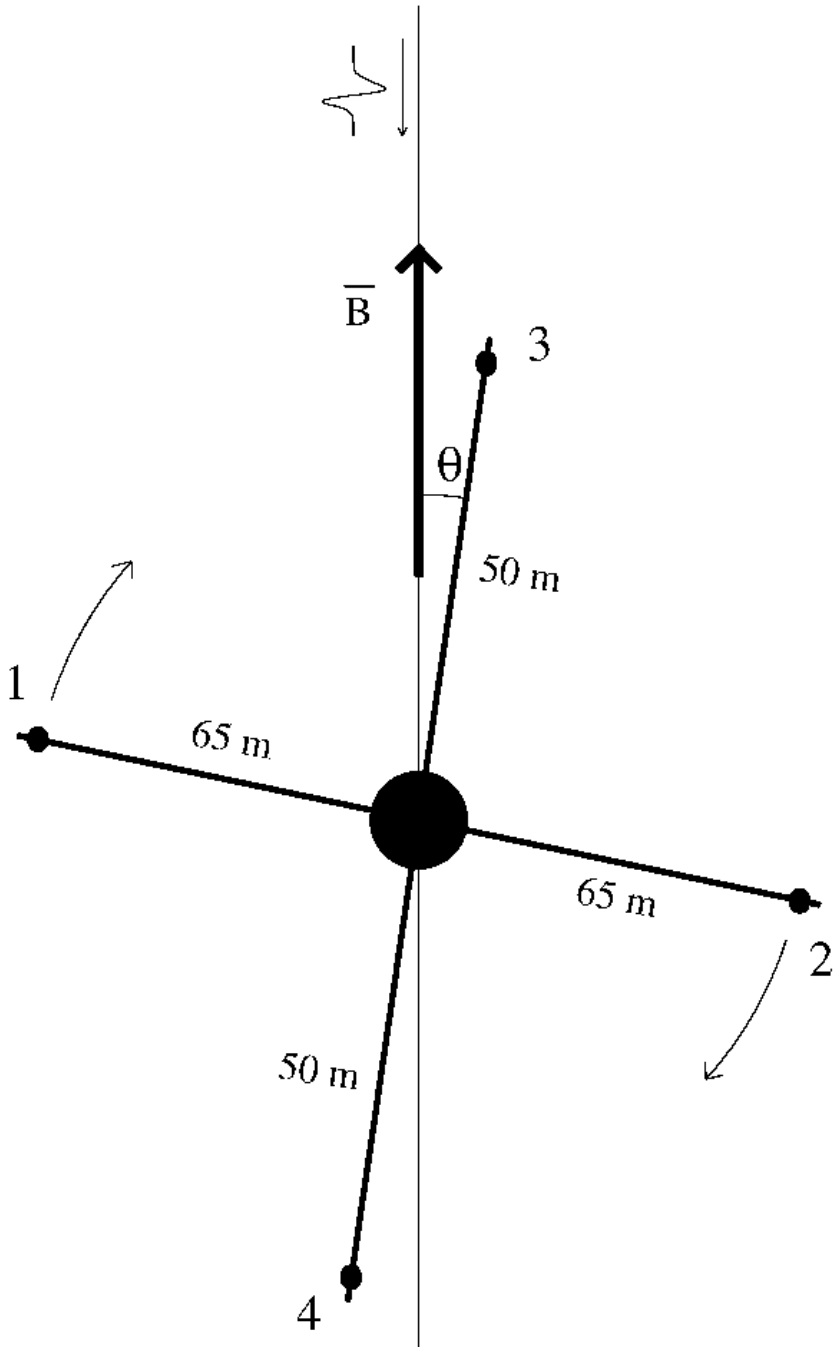

Figure 5.3: This figure shows how EFI is used as an interferometer to detect solitary waves. A solitary wave is shown traveling down the magnetic field line where it is first observed by probe 2, and then later by probe 4. The time difference between when these observations are made is used to determine the speed of the solitary wave. [Adapted from *Dombeck et al.*, 2001].

are roughly equal. The time delay is found by cross correlating the ϕ_+ and ϕ_- signals and find what time shift to the ϕ_- most closely matches it to the ϕ_+. An example of the output of the program used to detect solitary waves (described below) is shown in Figure 5.5.

5.2.1 Solitary Wave Selection Criteria

The Polar solitary waves are analyzed using an IDL (Interactive Data Language) program called Delaytime, originally written by John Dombeck [*Dombeck et al.*, 2001]. The goals of this program are to detect as many solitary waves as possible, while minimizing false positive detections of solitary waves. In order to do this, solitary waves of fairly arbitrary shapes are searched for, since not all solitary waves have symmetric, smooth shapes. Allowing for more general shape differs from some other studies [*Ergun et al.*, 1998a] where the solitary wave shape was fit to a Gaussian. Allowing for general solitary wave shapes is a more difficult problem than looking for Gaussian shapes, consequently a number of selection criteria are used in Delaytime.

The general method used by Delaytime to find solitary waves is as follows. First, all of the 8kHz electric field data for a burst is splined by a factor of 5. The measurements from detectors 1 and 3 are taken 25 μs earlier than the measurements from detectors 2 and 4. So splining is done so that cross correlation can be done on data with a common time basis. Data points that were 125 μs apart and had a time shift of 25 μs between the long boom pairs is splined to data that is 25 μs and has the same time basis for all detectors. Next, limits are placed on the angle between the near probe and the background magnetic field (θ). A minimum angle of 4 degrees is set to avoid problems with magnetic shadowing, and a maximum angle of 25 degrees is set to avoid having too small of an effective boom length. These angle tests are applied before the extrema are found, since the angle does not depend on the extrema and it cuts down on the amount of data that needs to be analyzed. Next, all of the extrema of the potential data are found. Then the neighboring extrema are checked to see if they actually denote a solitary wave, as opposed to some other oscillation. This involves applying several of the selection criteria. To allow for noisier solitary waves to be selected, 2 intermediate peaks within the solitary wave

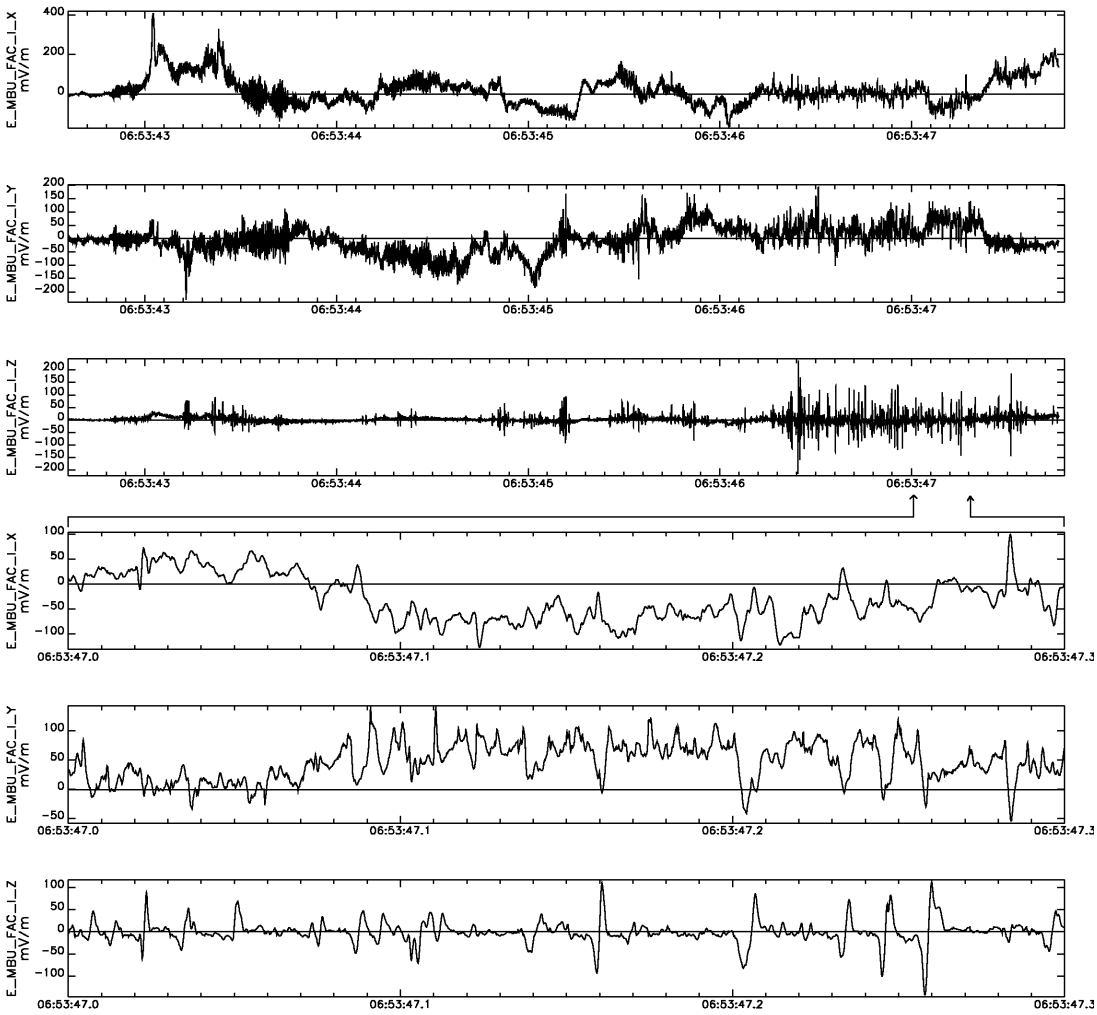

Time:	06:53:43	06:53:44	06:53:45	06:53:46	06:53:47
Re	1.96	1.96	1.96	1.96	1.96
MLT	16.98	16.98	16.98	16.98	16.98
MLat	−67.83	−67.79	−67.76	−67.73	−67.70
LShell	13.73	13.69	13.65	13.61	13.57

Figure 5.4: This figure shows a sample of EFI burst data from February 4, 1997. The top three panels show the electric field field-aligned coordinates (coordinates in which the z-direction is along the magnetic field direction) for the entire burst time period. The bottom three panels show an enlargement of a period containing several solitary waves. In particular, the solitary wave at 6:53:47.15 is the solitary wave shown in Figures 5.5 and 5.9. The solitary waves are most obvious in the z-component of the electric field, though most of these solitary waves have fairly obvious unipolar perpendicular signals as well.

Figure 5.5: The plot on the following page shows the analysis of a sample electron solitary wave.from the burst shown in Figure 5.4. The top panel shows the signals seen near (red line) and far (green line) boom (V_+ and V_- correspond to ϕ_+ and ϕ_- in the text) as well as the parallel electric field multiplied by minus the effective boom length (black line) for comparison purposes. The black vertical lines represent the limits of the solitary wave as determined by Delaytime. The small time delay between the two signals is evident in this plot. The lower panel shows the potential profile of this solitary wave with a slightly different time scale. Included on this plot are many different characteristics of the solitary and diagnostics of the fitting procedure.

were allowed. The amplitude of these intermediate peaks was set at 0.3 times the amplitude of the main solitary wave peak so that the noise of the intermediate peak is not comparable in size to the selected solitary. Also, the amplitude of the solitary wave seen by the one of the parallel probes was required to be within 0.7 of the amplitude seen by the other parallel probe. The minimum electric field amplitude for the solitary wave was also set at 1 mV/m.

Among the most important of the selection criteria is the minimum cross correlation coefficient between ϕ_+ and ϕ_-. Setting a minimum cross correlation coefficient is a trade-off between false positive detection of solitary waves (which will later be removed when solitary waves are checked by eye) and false negative detection of solitary waves (which will not be recovered). In this study the minimum cross correlation coefficient was set at 0.9. Also, a region of time equal to 0.3 times the time width of the solitary structure was checked to make sure there was not another peak with amplitude more than 0.3 times the size of the solitary wave. This criterion helped to eliminate the possibility that linear waves would mistakenly be identified as solitary waves by ensuring that the region just outside the solitary wave had a relatively flat electric field signal.

Nearest Boom to +DC B-Field = 4 FILE = dt1997103119.sw.3.ps

	TIME	TOTAL ANGLE	Spin Angle	Cant Angle
START	19:45:19.001225	10.564496	89.365754	-10.545656
END	19:45:19.020350	10.545557	89.938213	-10.545378

EFFECTIVE BOOM LENGTH
@ AVG. TOTAL ANGLE = 49.2 m
DATA RATE = 0.0001250 s
SPLINED RATE = 0.0000250 s

VELOCITY (km/s)
SPLINED -164
Range -246- -131

Delay Error Range: (0.20) -0.0003750- -0.0002000

DELAY (Seconds)
SPLINED -0.000300

CROSS-CORRELATIONS

-4 Points	-2 Points	-1 Point	@DELAY	+1 Point	+2 Points	+4 Points
0.989	0.991	0.992	0.992	0.992	0.992	0.990

Avg. Offset: 0.29 V Par. Pk-Pk.: 82.9 mV/m Time Width: 0.019125 s E Field Polarity: -/+

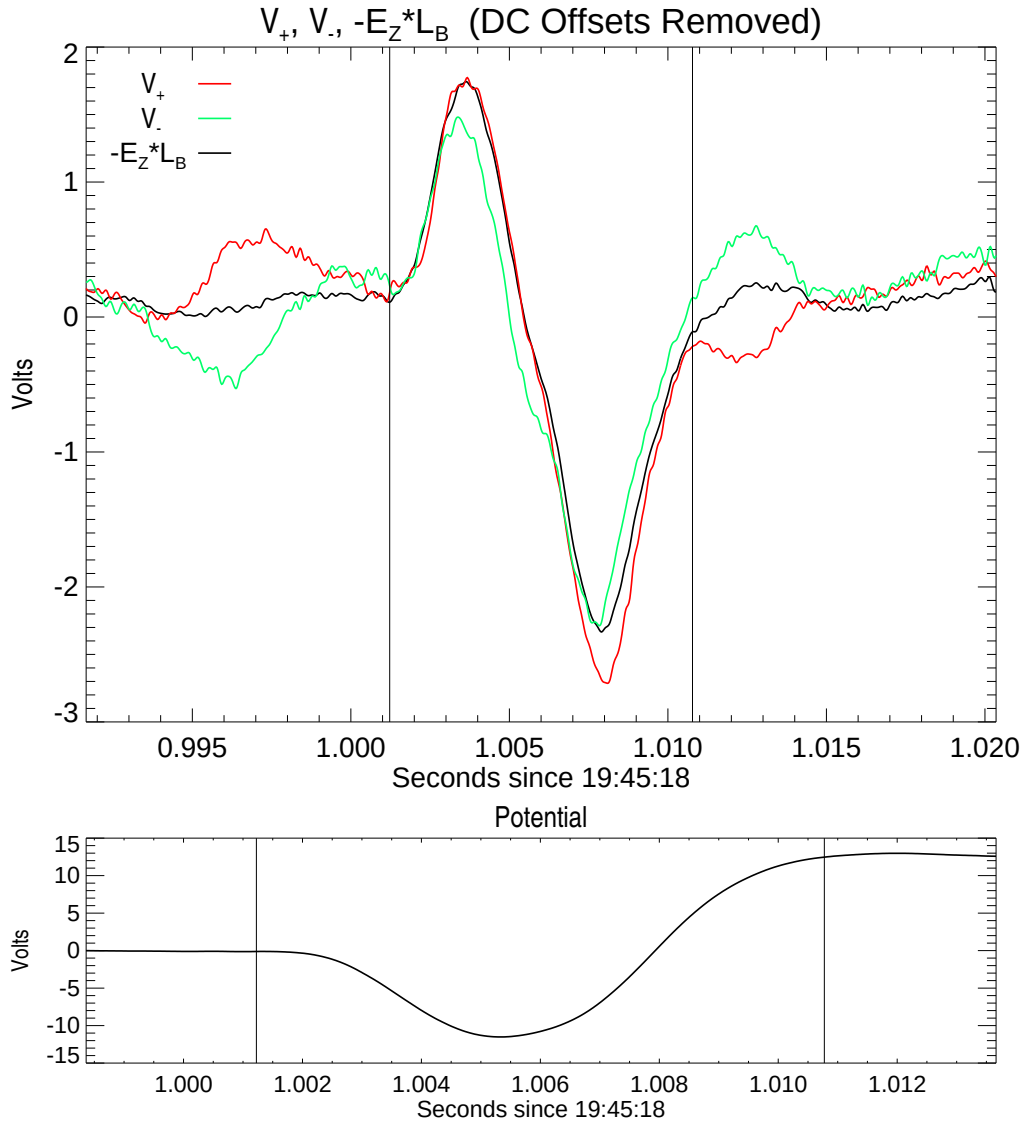

Structure Width: 3.1 km
Potential Amp: -23.99 V
Potential Dif: 12.59 V

Range (km): 2.51- 4.70
Range (V): -9.12- -36.74
Range (V): 10.07- 19.47

Geoc. Dist. (R_E): 2.08
MLT (Hours): 21.03
Mlat (Degrees): -59.94

<Vers. 3.52 Jul 16, 2002>

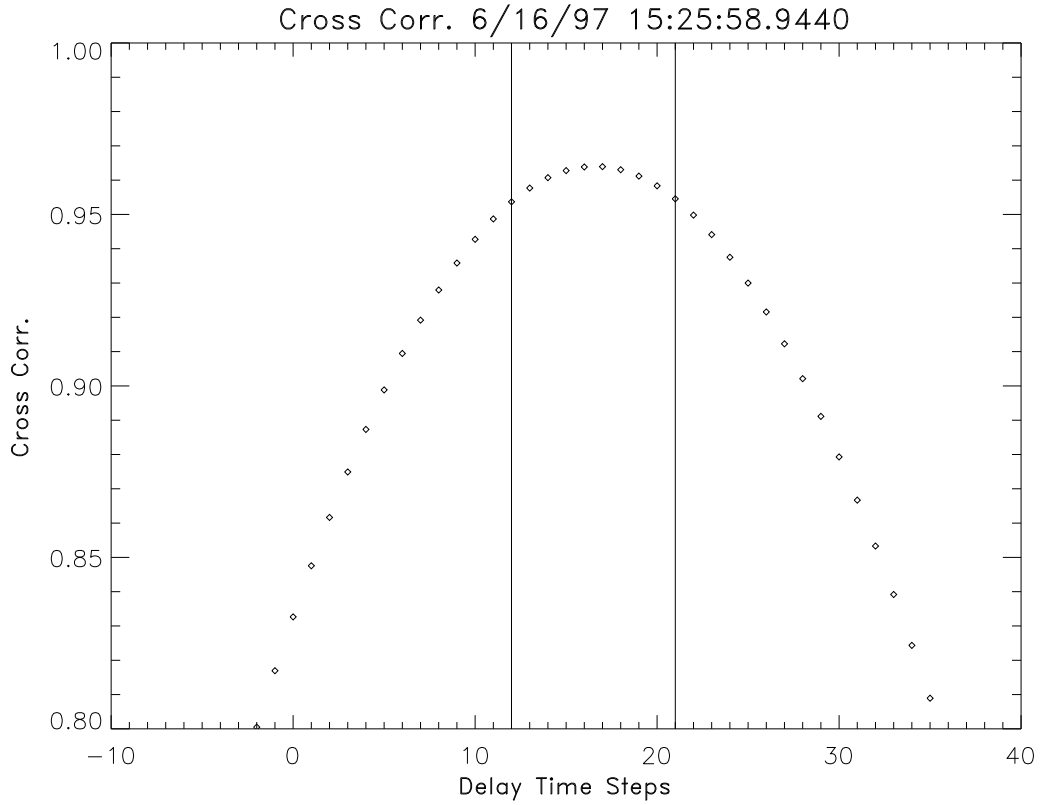

Figure 5.6: This plot shows the variation of the cross correlation coefficient with time delay from a typical solitary wave. The peak correlation is chosen as the time delay for this solitary wave and the error range for the time delay is shown by the vertical lines. [Figure from *Dombeck et al.*, 2001].

5.2.2 Solitary Wave Parameters

As well as determining the time delay for a solitary wave, an error range on the time delay is also found from cross correlation analysis. The time delay is picked as the point with the highest cross correlation, so the time delay has a resolution of 25 μs. The error range on the time delay is found from the time delay where the cross correlation has fallen so that:

$$c < 1.2c_{max} - .2 \tag{5.5}$$

where c is the cross correlation and c_{max} is the maximum cross correlation. A example of the cross correlation versus time delay for a typical solitary wave is shown in Figure 5.6. The typical error range is 2 to 4 time points on each side of the time delay. The error ranges for time delays are propagated through for the other solitary wave characteristics mentioned below.

The time delay leads directly to the solitary wave speed:

$$v_{sw} = \frac{L_{boom_{eff}}}{t_{delay}} = \frac{L_{boom}\cos\theta}{t_{delay}}, \tag{5.6}$$

where θ is the total angle between the background magnetic field and the booms most closely aligned to the background magnetic field, L_{boom} is the total length of the boom, $L_{boom_{eff}}$ is the effective boom length parallel to the magnetic field, and t_{delay} is the time delay. A positive velocity corresponds to a structure moving anti-parallel the magnetic field direction. So a positive velocity is away from Earth in the southern hemisphere, and toward the Earth in northern hemisphere.

Once the velocity of the solitary wave has been calculated, several other properties of the solitary wave can be determined. The parallel scale size of the solitary wave can be determined from the solitary wave speed and the time width of the solitary wave:

$$L_{sw} = v_{sw}t_{width}. \tag{5.7}$$

The parallel potential profile can be determined by integrating the measured electric field:

$$\Phi_{sw} = -\int E_{sw}dx = -\int E_{sw}v_{sw}dt. \tag{5.8}$$

From the parallel potential profile, the potential amplitude and the potential difference (rise or drop) of the solitary wave is determined. The results for a sample solitary wave for this and several other parameters are shown in Figure 5.5.

5.2.3 Perpendicular Characteristics of Solitary Waves

Since solitary waves only pass Polar in the direction parallel to the magnetic field and since the scale size of solitary waves is much larger than Polar's booms, the perpendicular potential profile of solitary waves cannot be measured directly. Some information about the perpendicular scales of the solitary wave can be determined from the perpendicular electric field. The perpendicular electric field also might give hints as to what portion of the solitary wave Polar is passing through, since it cannot be assumed that Polar passes through the center of the structure. If a solitary wave is a symmetric charge structure, it is expected that while the parallel electric field signature is bipolar, the perpendicular electric field signature should be unipolar (see Figure 5.7). In an ideal solitary wave, the minimum or maximum of the perpendicular signal for the solitary wave would occur at the midpoint of the parallel signal of the solitary wave. In Figure 5.9, the perpendicular signature of the solitary wave shown in Figure 5.5 is shown. The perpendicular signal of this solitary wave is unipolar, but the minimum of the perpendicular electric field does not occur at the same time as the center of the parallel signal of the solitary wave. This difference may be due to other waves being present at the same time, or it may relate to non-uniformity in the actual structure of the solitary wave.

5.3 Summary

The Polar spacecraft has a variety of instruments which measure fields and particles and image particles. Though the electric field instrument is the most important to this study of solitary waves, magnetic field and particle data are also used here. Polar's orbit has a perigee of 1.8 and an apogee of 9 R_E geocentric and the precession of its orbit has allowed Polar to observe linear

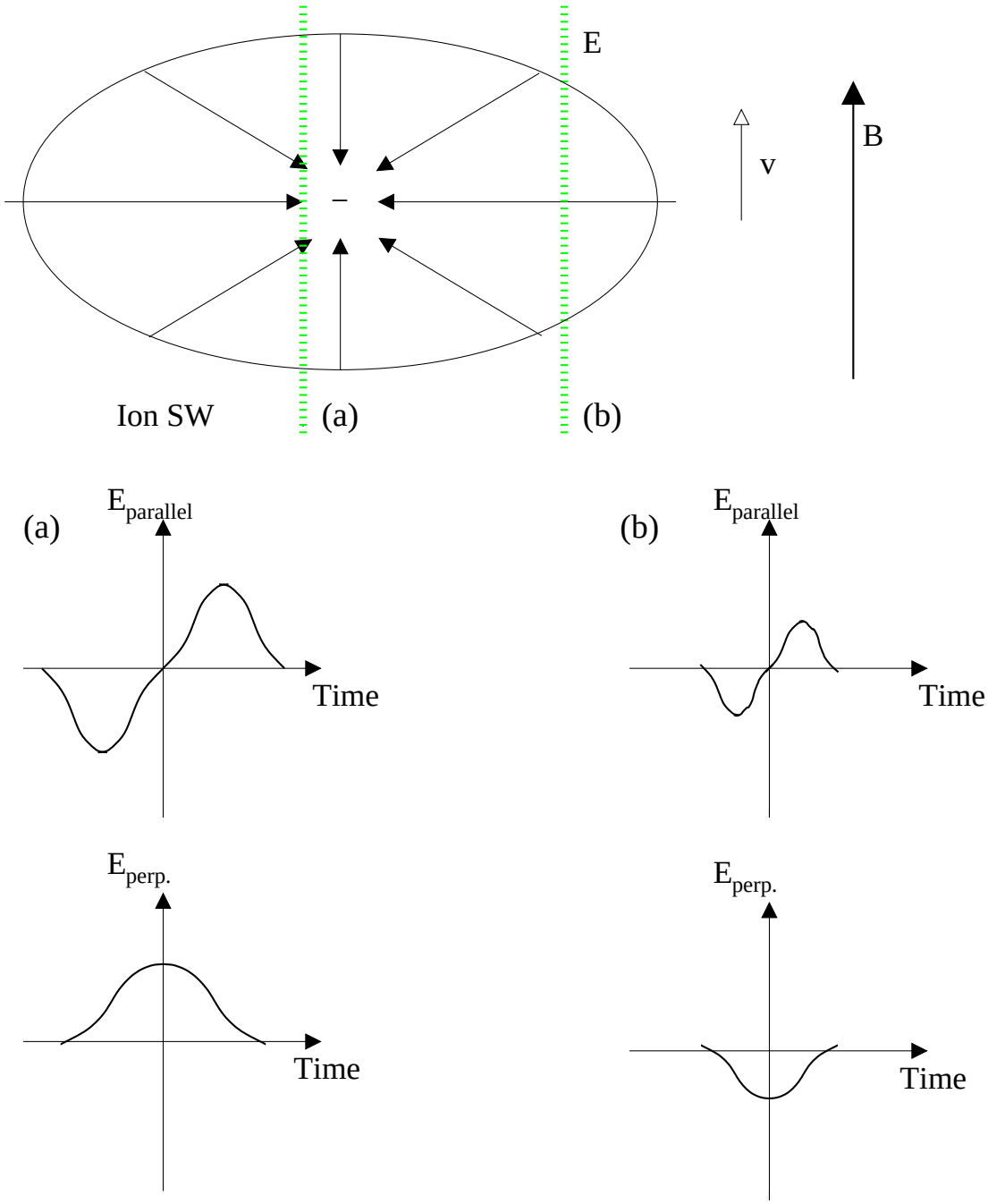

Figure 5.7: Shown above is the diagram of perpendicular structure of a model solitary wave. The green dashed lines show two spacecraft paths through the solitary wave, and the plots below show the parallel and perpendicular electric fields that would be measured. Notice that the values of both components of the electric field scale depending on how close to the center of the solitary wave the spacecraft path crosses.

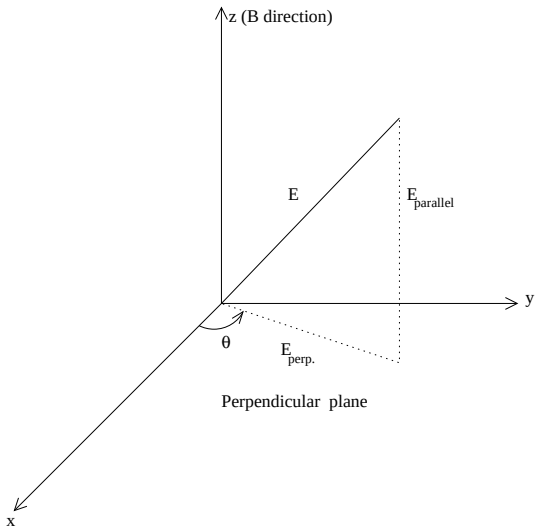

Figure 5.8: Magnetic field-aligned coordinates used for analysis of electric field, as in Figure 5.9.

and nonlinear waves in many different regions of the magnetosphere. Polar's EFI is a fully 3-dimensional detector and it has onboard memory which allows it to save high time-resolution data for short bursts of time, which is critical for this study. Solitary waves are detected and analyzed by using EFI as an interferometer. As well as the speeds of the solitary waves, the spatial size to the magnetic field and potential amplitudes of the structures are also determined. Several selection criteria, are used to find solitary waves and the automatically detected solitary waves are later verified by eye.

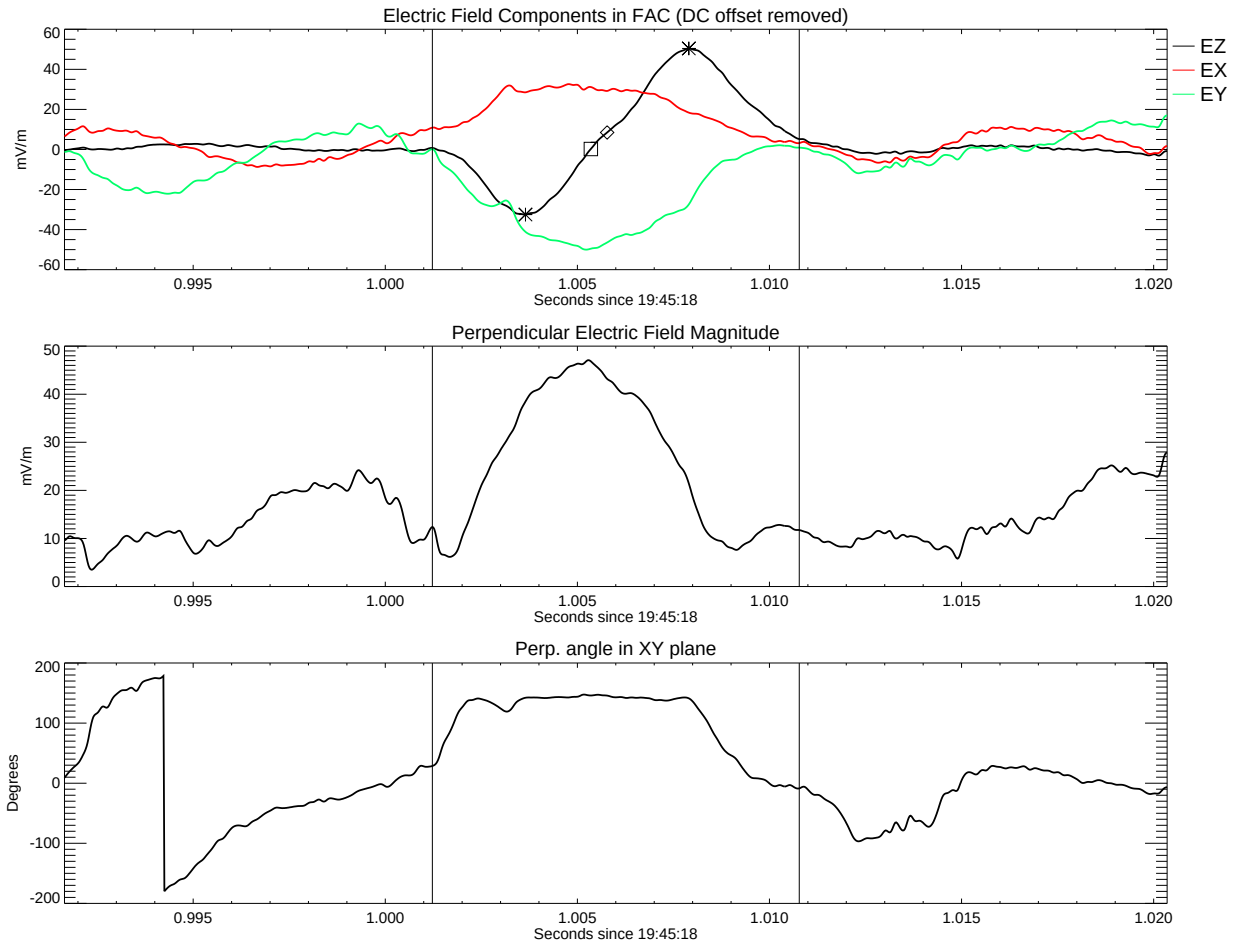

Figure 5.9: This plot shows the perpendicular characteristics of the solitary wave in Figure 5.5. The top panel shows the electric field of the solitary wave in field-aligned coordinates. The next panel has magnitude of the perpendicular magnetic field. The bottom panel show the angle of the solitary wave in the perpendicular plane (see Figure 5.8). The *'s on the plot mark extrema of the plots. The box on the plot top panel marks 0 crossing of the z-component of the electric field and the diamond marks the halfway point between the extrema of the solitary wave. The box and the diamond represent two different ways of determining the center of the parallel signal of the solitary wave, and in this case the results from both methods are the same. Notice that the minimum of the perpendicular electric field is at a time between the minimum of the parallel electric field and the midpoint of the solitary wave.

Chapter 6

Simulations of Ion Solitary Waves [1]

6.1 Introduction

Previous simulation studies of the ion beam related solitary waves attempting to explain the S3-3 and Viking observations [*Boström et al.*, 1988] have described ion solitary waves as being related to ion acoustic solitons [*Barnes et al.*, 1985; *Marchenko and Hudson*, 1995], or Bernstein-Greene-Kruskal (BGK) ion phase space holes [*Tetreault*, 1991], while electron beam related solitary waves are thought to be electron acoustic waves [*Dubouloz et al.*, 1991], or BGK phase space holes [*Muschietti et al.*, 1999a, b; *Goldman et al.*, 1999; *Singh*, 2000]. The work on ion acoustic solitons is based on the theory that nonlinear, coherent potential pulses can develop from linear acoustic waves [*Lotko*, 1983]. Later work extended this theory to include H^+ and O^+ beams [*Qian et al.*, 1989]. In the simulations these structures developed from the interaction of one or more ion or electron beams with background ion and electron populations. The BGK phase space hole theory is based on the idea that holes in the phase space distribution of ions can develop owing to thermal fluctuations, and that these holes can propagate and grow [*Dupree*, 1982]. In simulations these structures driven by drifts between ion and electron species and thermal fluctuations. Simulations of both mechanisms for developing

[1] **An earlier form of this chapter was published as** *Crumley et al.* **[2001].**

solitary waves matched the S3-3 and Viking observations fairly well, but the new observations of plasma distributions and solitary wave characteristics suggest the need for new simulation studies.

In this study we examine ion beam related solitary waves seen in the auroral acceleration region. Our goal is to determine the effect of (1) no cold plasma and (2) ion composition, on the solitary waves. The parameters we use are based on FAST and Polar observations of the auroral acceleration region [*Strangeway et al.*, 1998; *McFadden et al.*, 1999c]. In order to model the observed plasma parameters, we include hydrogen and oxygen ions, since both species are usually present in ion beams in the auroral acceleration region. Previous one-dimensional (1-D) studies of solitary waves [*Hudson et al.*, 1987] have shown that the inclusion of both ion species results in the two-stream instability which affects the range of conditions under which solitary waves can form. Further 1-D studies [*Gray et al.*, 1992] showed that solitary waves formed more quickly when oxygen was present than when only hydrogen was included. We will compare the results of our simulations to theories and recent observations of ion solitary waves. In section 6.2 we describe the details of the simulation. Section 6.3 presents results of some of the simulation runs. Comparison to observation and a discussion of the significance of our studies are given in section 6.4.

6.2 Simulation Details

Our simulations were done using ES2 (see Chapter 4), a 2.5-dimensional, electrostatic particle-in-cell code with periodic boundary conditions. See Table 6.1 for details on simulation parameters used and the physical values that they correspond to. A 128 by 128 grid was used for the runs presented here, with each grid cell being one Debye length long on a side. The simulations were run with time steps equal to 0.3 times the inverse electron plasma frequency (ω_{pe}^{-1}), with 10,000 iterations done for each run. In addition, runs were completed with a 1024 by 128 grid and with time steps of 0.03 ω_{pe}^{-1} to examine numerical effects. Potential

Parameter	Simulation Value	Physical Value
Grid size	128 by 128	21.2 km by 21.2 km
Size of each grid box	1 λ_D by 1 λ_D	165 m by 165 m
Plasma frequency	1 ω_{pe}	9 KHz
Number of time steps	10,000	
Length of time step	0.3 ω_{pe}^{-1}	33 μs
Electron cyclotron frequency	9 ω_{pe}	81 kHz
Electric field	0.6 T_e/eL_x	14 mV m^{-1}
Hydrogen to electron mass ratio	100	1,836
Helium to hydrogen mass ratio	4	4
Oxygen to hydrogen mass ratio	16	16

Table 6.1: Simulation Parameters

plots were averaged over 100 iterations (30 ω_{pe}^{-1}) in order to average out high-frequency noise. The plasma was magnetized so that the electron cyclotron frequency was equal to 9 times the electron plasma frequency. The chosen value for the cyclotron frequency leads to a highly magnetized plasma, which previous studies [*Barnes et al.*, 1985] had indicated was necessary for solitary wave formation. An electric field equivalent to a potential drop of 0.6 T_e across the simulation box was applied along the magnetic field direction. The applied electric field is added to simulate the field-aligned potential drop seen in the auroral acceleration region, as has been done in previous particle-in-cell (PIC) studies of solitary waves [*Marchenko and Hudson*, 1995]. This electric field accelerates the particles and results in relative drifts which provide the source of free energy for the solitary waves.

Simulations of two-, three-, and four-species plasmas are presented here. In the two-species cases the plasma species used are a stationary hot electron population and a hydrogen beam (with the physical number density of each being 1 cm^{-3}). In the three-species cases an oxygen beam is added and in the four-species cases helium is added. A study of ion beam events in

the auroral zone using FAST [*McFadden et al.*, 1999c] data found that the ratio of O^+ number density to H^+ number density ranged from 0.28 to 1.44, with typical values being around 1. *McFadden et al.* [1999c] also found that the ratio of He^+ number density to H^+ number density ranged from 0.20 to 0.67, so helium ions could also play a role in the dynamics of ion-associated solitary waves. The oxygen to hydrogen number density ratio of 1 was chosen for the three-species cases since it is fairly typical of the observations. For the four-species cases, the oxygen to hydrogen and helium to hydrogen ratios were chosen to be 0.5. *McFadden et al.* [1999c] also found plasma sheet ion densities which ranged from much smaller than the beam densities up to comparable densities. Since the plasma sheet ion densities were usually smaller and not believed to be necessary for the production of solitary waves we choose to ignore the plasma sheet population for the purposes of this study, though future studies will include it. The plasma sheet ion populations would probably slow the solitary waves since the beams would probably transfer momentum to the relatively stationary plasma sheet populations, but the remainder the behavior of the solitary waves would probably remain unchanged.

The ion beams start out with equal energies, giving them different velocities, which leads to two-stream interactions between the beams [*Bergmann et al.*, 1988]. Simulations were run with the ratio of hydrogen to electron mass equal to 100 to conserve computing time [*Barnes et al.*, 1985], while the oxygen to hydrogen mass ratio was 16. The plasma species parameters for the four-plasma species cases are shown in Table 6.2 and were chosen to follow the parameters recently observed [*McFadden et al.*, 1999c]. The parameters used for the three-species cases are identical, except that all of the helium particles are replaced by oxygen, and for the two-species case, all of the helium and oxygen are replaced by hydrogen. In the simulations all values are normalized, and the physical units matching these choices were as follows. The electron temperature was initially 0.5 keV, while both ion species had temperatures of 0.1 keV. The ion beams were chosen to have drift energies ranging from 2 to 32 keV. Some of these drift energies are higher than the range from 0.8 to 10 keV seen by FAST [*McFadden et al.*, 1999c], but the higher values were used so that there would be a wider range over which to determine

	Electron	Proton	Helium	Oxygen
Number of particles	13,1072	65,536	32768	32768
Temperature (T_e)	1	0.2	0.2	0.2
Beam speed (v_{te})	0	0.2-0.8	0.1-0.4	0.05-0.2

Table 6.2: Species-Dependent Parameters

the effects of changing the beam energy.

6.3 Simulation Results

Results of a simulation with a hydrogen beam of speed 0.4 v_{te} and an oxygen beam speed of 0.1 v_{te} are shown in Figure 6.1, where v_{te} is the electron thermal speed. The solitary waves can be identified as nearly circular depressions in the electrostatic potential in these simulations (see Figures 6.1e and 6.1f). At the beginning of a simulation run, the potential is flat, but electrostatic ion cyclotron wave perturbations in the potential begin to build up. These perturbations occur at both the hydrogen and oxygen cyclotron frequencies. These waves may be caused by the two-stream instability between the hydrogen and oxygen beam, since the two-stream instability is expected to excite obliquely propagating ion cyclotron waves [*Bergmann et al.*, 1988; *Gray et al.*, 1990], though not parallel propagating ion cyclotron waves [*Bergmann and Lotko*, 1986], in the conditions presented in these simulations. In fact, linear dispersion relation calculations performed for these conditions yield unstable ion cyclotron modes. These ion cyclotron waves may be a generation mechanism for the solitary waves.

Solitary structures begin to form after $\sim 400\ \omega_{pe}^{-1}$. They propagate in the beam direction and last between 150 and 2000 ω_{pe}^{-1}, with typical lifetimes of $\sim 400\ \omega_{pe}^{-1}$. The solitary structures are circular in shape with radii of the order of 20 λ_D. The size of the structures changes during their lifetime, with a typical solitary wave starting out small both in amplitude and spatial size, growing for a time, then shrinking and dissipating. The shapes vary somewhat between solitary waves in the same run, with the shapes having a range of oblateness.

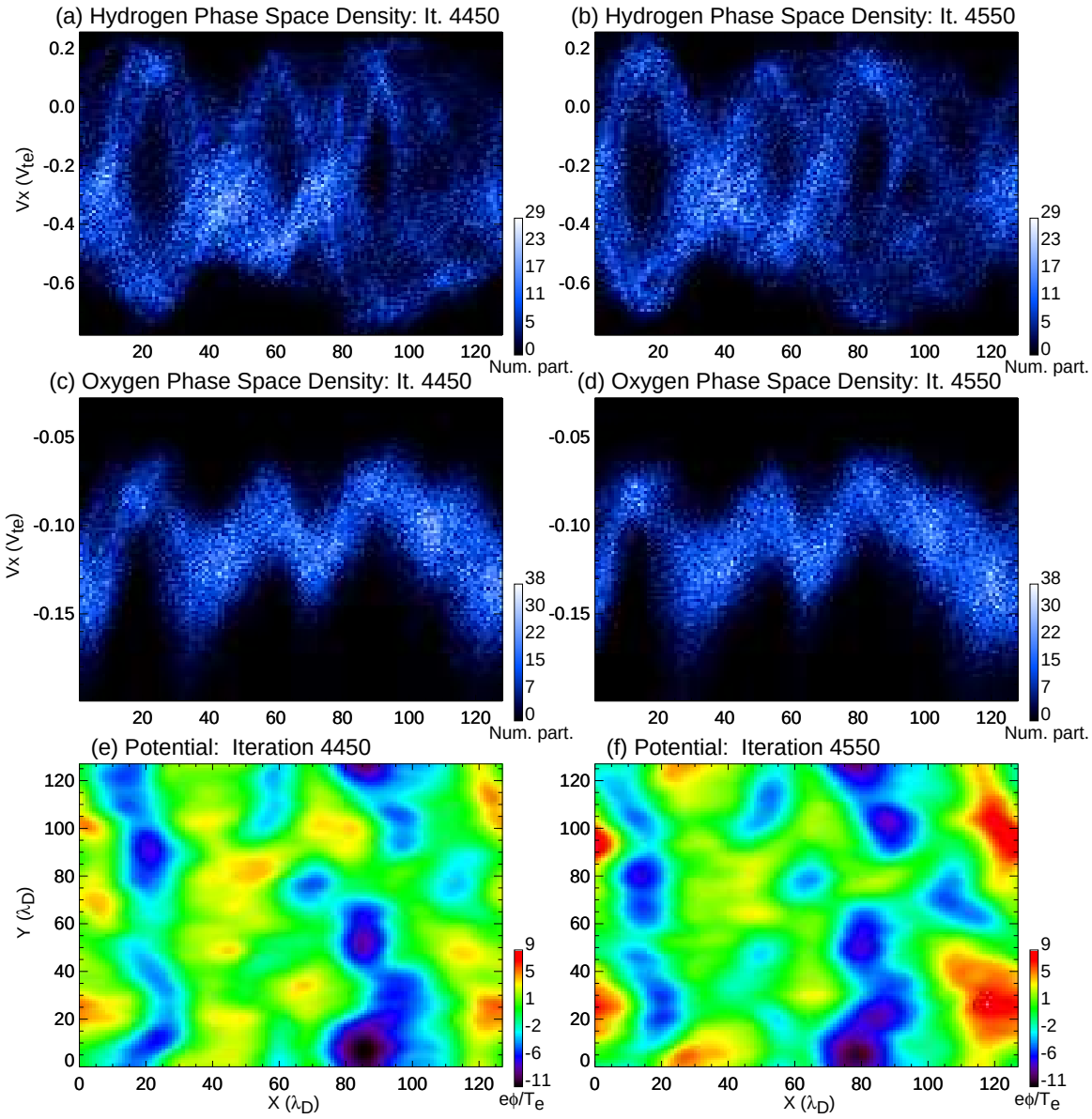

Figure 6.1: Phase space densities for (a,b) the hydrogen ions and (c,d) the oxygen ions, as well as (e,f) the electrostatic potential, for iterations 4450 (1335 ω_{pe}^{-1}) and 4550 (1365 ω_{pe}^{-1}). The electrostatic potential are in units of kT_{e_0}/e, where T_{e_0} is the original electron temperature. The phase space density plots are in particles per phase space grid box, where the phase space grid is divided into 128 in the *X* direction and 100 in the V_X direction. These plots are from the 8-keV beam run, which corresponds to beam speeds of 0.4 v_{te} and 0.1 v_{te} for the hydrogen and oxygen beams, respectively. The electrostatic potential shown is averaged over 100 iterations (30 ω_{pe}^{-1}) to remove high-frequency oscillations. The solitary waves are the dark, circular areas of negative potential, and they move from right to left with ion beams. This is the same direction as the ion beams and applied electric field and the opposite direction from the background magnetic field.

The development of the solitary structures is also evident in the phase space densities of the plasma species (see Figures 6.1a-6.1d). Initially, all species are Maxwellians, but the distributions begin to show sizeable fluctuations at about the same time that solitary structures first appear in the potential. These fluctuations tend to be in phase spatially between species, with the major peaks and troughs of the phase space density tending to line up across species. These fluctuations move in the ion beam direction, as the potential structures do. As the simulation progresses, the phase space fluctuations become more pronounced. The simple sinusoidal forms of the early fluctuations are replaced by more complicated forms. The two-stream instability leads to an interesting phase space structure in the hydrogen ions (see Figures 6.1a and 6.1b), with a pattern resembling a standing wave. At the antinodes there is a peak in both the negative and positive sides of the velocity axes in the phase space density at the same x value, with a hole in the phase distribution between. At the nodes the phase density reaches its highest values, and particles are spread over a smaller range of speeds. We believe this complex pattern is caused by the balance of the two-stream interaction which tends to bring the hydrogen drift speed down to the oxygen drift speed, and the electric field which tends to accelerate the hydrogen ions more quickly than the oxygen ions. Phase space densities of this type are seen only in the three-species cases. In the two-species cases the hydrogen phase space densities resemble those seen in the oxygen phase space density shown in Figures 6.1c and 6.1d. No standing wave patterns are formed in these cases, though sinusoidal phase space oscillations do occur. It is likely that the extra complexity seen in the three-species cases is due to the two-stream interaction. In the four-species cases, the hydrogen phases space densities look similar to those in the three-species cases, and the helium and oxygen phase space densities look similar to the oxygen phase space density in the three-species case.

The effect of the two-stream interaction is evident in the behavior of the ion species drift speeds, as shown in Figure 6.2. The momentum transfer between the ion species is evident in the sharp fall in the hydrogen drift speed and the rise in the oxygen drift speed centered around iteration 4000 (1200 ω_{pe}^{-1}). This time period is also when the solitary wave activity is greatest.

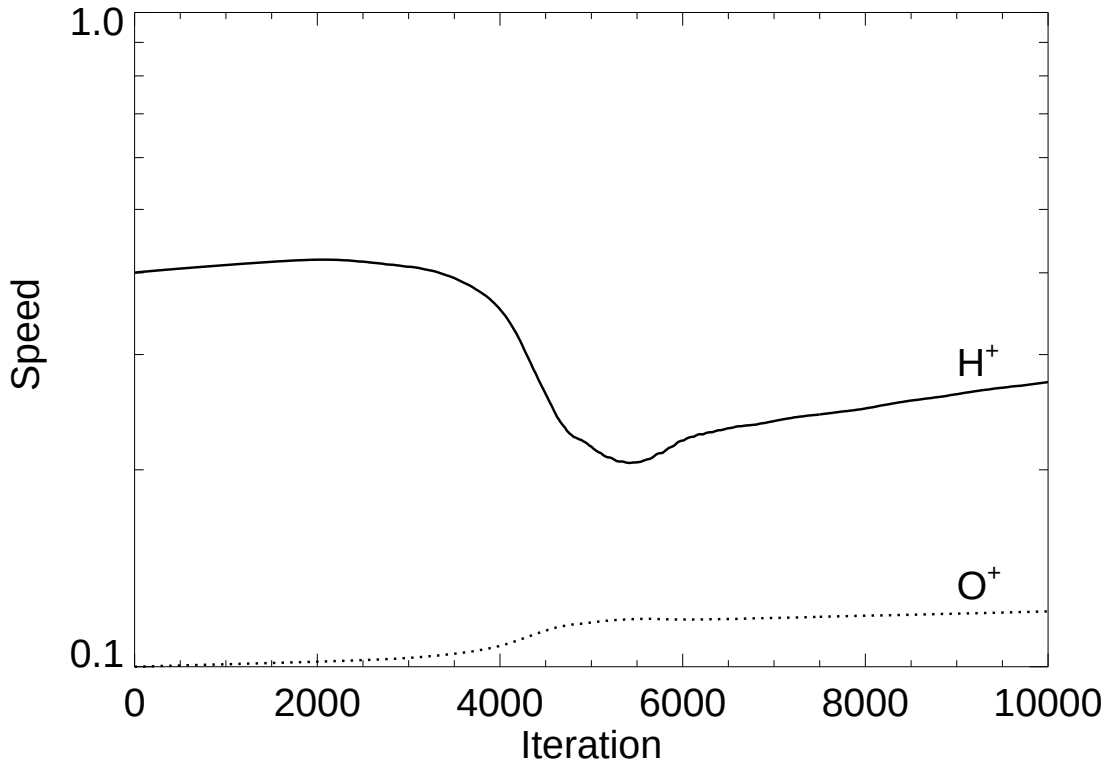

Figure 6.2: Plot showing the ion drift speeds, with a logarithmic scale in units of the initial electron thermal speed (v_{te}), versus iteration, where each iteration is 0.3 ω_{pe}^{-1}. Figure 6.2 is for the case where the initial hydrogen drift speed was 0.4 v_{te} and the initial oxygen drift speed was 0.1 v_{te}.

Though the two-stream instability works to equalize the beam speeds of the two ion species, the applied electric field prevents the complete equalization. After iteration 5000 (1500 ω_{pe}^{-1}) the solitary wave activity begins to dissipate, the effects of the applied electric field dominate, and both ion species increase their drift speeds. As with the drift speeds, the effects of the solitary waves are also evident in the parallel (Figure 6.3) and perpendicular (Figure 6.4) drift energies of the plasma species. The ion species both have peak heating rates parallel to the magnetic field around iteration 4000, owing to the interaction of the ions with the solitary waves. After the solitary waves dissipate, the parallel thermal energies of the ion species level off, and the hydrogen ions even cool slightly. The electron heating rate is more constant, though the heating rate does peak when the solitary waves are dominant. The heating rate perpendicular to the magnetic field for the ions also peaks while the solitary waves are dominant (Figures 6.4b and 6.4c). The ions show the effects of ion cyclotron waves, with oscillations at the corresponding ion cyclotron frequency evident in both ion species. The electrons show very little heating in the perpendicular direction because the time step size of 0.3 ω_{pe}^{-1} does not resolve oscillations of the order of the electron cyclotron period, $\sim 0.1\ \omega_{pe}^{-1}$.

Some of the physical parameters used for the runs presented here were varied in other runs to examine their effects on the results. The applied electric field was varied, in order to see how it affected the solitary waves. Solitary waves do not develop in this simulation if the field is omitted, probably because the instabilities which lead the solitary waves quench too quickly without the constant drive of the applied electric field. Decreasing the value used for the electric field increased the length of time it took for the solitary waves to develop and decreased the potential drop seen in the solitary waves. Utilizing $\Omega_{ce}/\omega_{pe} = 9$ leads to a highly magnetized plasma, which previous studies with cold plasma [*Barnes et al.*, 1985] indicated was necessary for solitary wave formation. To test whether this was the case when there was no cold plasma, several runs with lower magnetic fields (i.e., $\Omega_{ce} = 1\ \omega_{pe}$ and $0.1\ \omega_{pe}$, compared to the original value of $9\ \omega_{pe}$) were done. These runs still had solitary waves, though they were smaller in potential amplitude and slightly more oblate in the perpendicular direction.

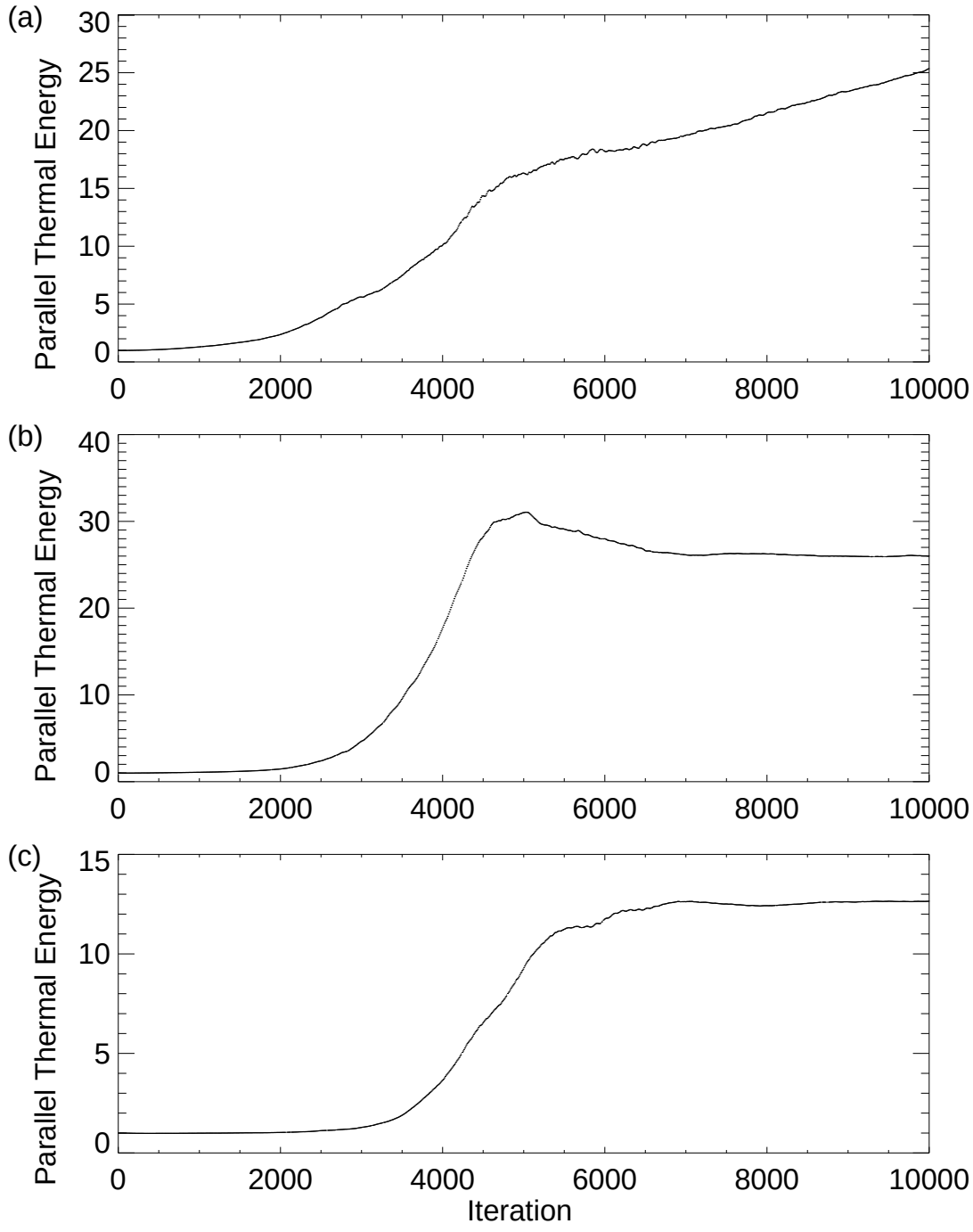

Figure 6.3: The parallel thermal energy, normalized to the species initial thermal energy, versus iteration, where each iteration is 0.3 ω_{pe}^{-1}, shown for the (a) electrons, (b) hydrogen ions, and (c) oxygen ions. Figure 6.3 is for the case where the initial hydrogen drift speed was 0.4 v_{te} and the initial oxygen drift speed was 0.1 v_{te}.

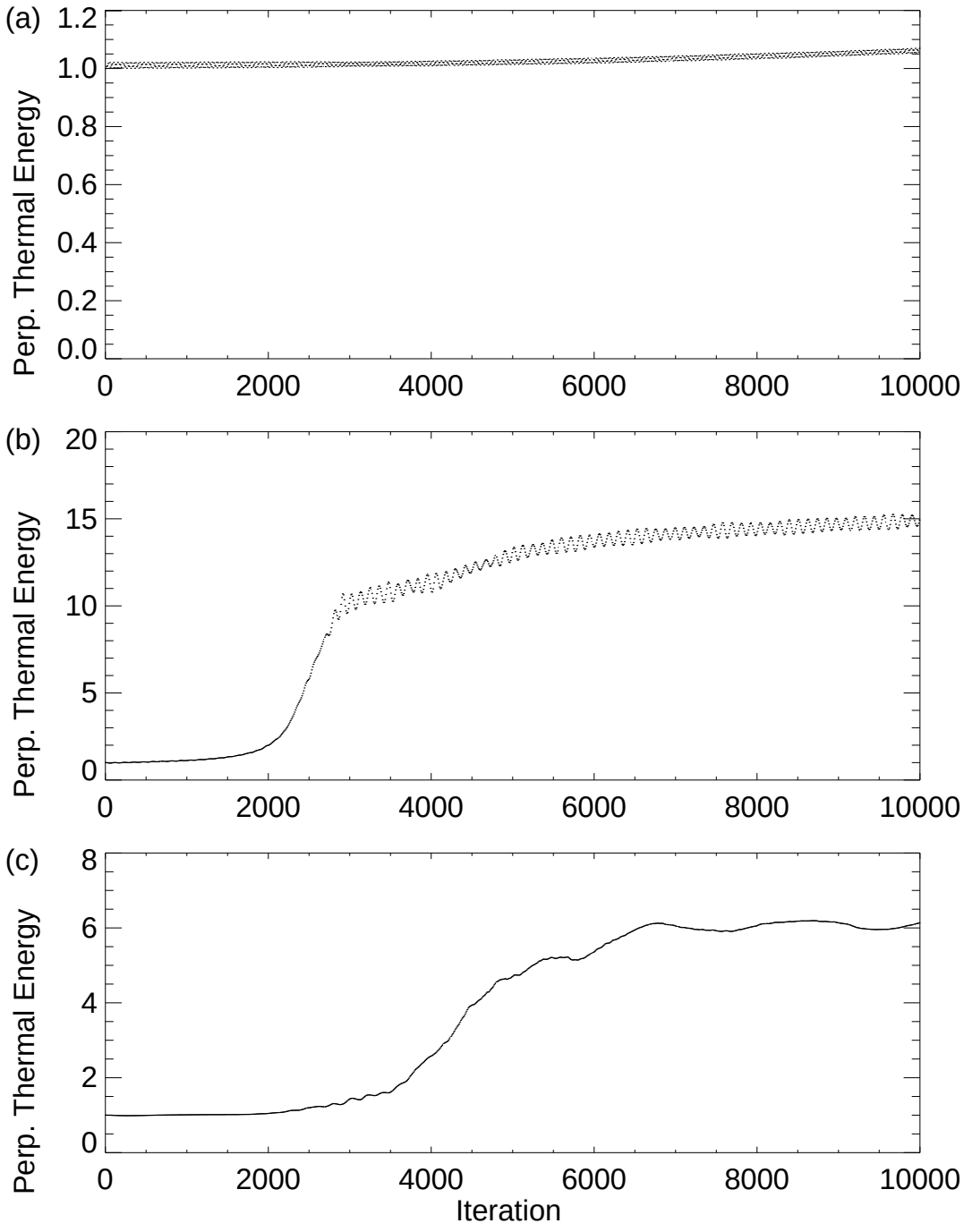

Figure 6.4: The perpendicular thermal energy, normalized to the species initial thermal energy, versus iteration, where each iteration is 0.3 ω_{pe}^{-1}, shown for the (a) electrons, (b) hydrogen ions, and (c) oxygen ions. Figure 6.4 is for the case where the initial hydrogen drift speed was 0.4 v_{te} and the initial oxygen drift speed was 0.1 v_{te}.

Several computational parameters were varied in order to isolate any numerical effects on the simulated solitary waves. Additional runs were performed with grid sizes up to 1024 λ_D along the magnetic field line to ensure that particle recycling due to the periodic boundary conditions did not alter the results. These runs gave results which were equivalent to those shown here. The effects of the time step size were also tested by using a time step that was a factor of 10 smaller in one case (0.03 ω_{pe}^{-1} instead of 0.3 ω_{pe}^{-1}). This change had no noticeable effect on the solitary wave behavior, though electrons did heat more in the perpendicular direction than in Figure 6.4a, since this time step size resolved the electron cyclotron time scale. In the cases with a time step of 0.3 ω_{pe}^{-1} the electrons essentially move on their guiding center orbits with no cyclotron motion. The effects of the number of simulation particles per grid cell were also tested by performing a simulation run with 8 times as many particles per grid cell. The behavior of the solitary waves was not changed in this run, though there was a decrease in noise which allowed for averaging over fewer iterations.

In order to see how the solitary wave behavior varied with ion beam characteristics, simulation runs were performed for a range of ion beam energies, which were equivalent to initial hydrogen beam drift speeds between 0.2 and 0.8 v_{te}. The speeds at the lower end of this range are more typical of what is observed in the auroral region, but a wide range of drift speeds was examined in order to study the relationship between beam drift speed and solitary wave speed. Runs with this range of beam energies were made with hydrogen, oxygen and helium beam, as well as with hydrogen and oxygen beams, and with hydrogen beams, in order to assess the effects of the multiple species beams on the solitary waves. The speeds of the solitary waves were determined by following the minimum potential of a structure between iterations to determine how far the structure moved. The solitary wave structures are not always symmetrical, so the minima of the potential do not always fall at the location that is the center of the structure. This leads to uncertainty in the solitary wave speeds, which necessitates averaging the speeds over several frames of the electrostatic potential, or at least 150 ω_{pe}^{-1}, in order to get accurate speeds. These average speeds for each solitary wave are then averaged for a few separate solitary waves

to find typical speeds for a run, and they are plotted against beam speeds in Figure 6.7. The average solitary wave speeds for all runs lie below the hydrogen beam speed. In the cases with both hydrogen and oxygen the solitary wave speeds are between the two beam speeds. In the cases with hydrogen, oxygen, and helium all of the solitary wave speeds except one were above the helium beam speed and all are above the oxygen beam speed. This result matches what has been observed by the Polar spacecraft in the auroral acceleration region. *Bounds et al.* [1999] found, using Hydra ion distribution data and assuming that both H^+ and O^+ had equal energies, that the solitary waves had speeds between the beam speeds of H^+ and O^+. Further Polar spacecraft studies found [*Dombeck et al.*, 2001], using H^+ and O^+ distribution data from TIMAS, that the ion solitary waves had speeds between the measured H^+ and O^+ beam speeds. The TIMAS data used to find the ion beam speeds is shown in Figure 6.5. Note that the ion beams in Figure 6.5 have very spread distributions which suggests that the beams were heated by waves. The plot of the solitary wave speeds versus potential amplitude for the Polar observations in Figure 6.6 shows that the solitary wave speeds are between the ion beam speeds.

The electrostatic potential amplitude also shows dependence on the initial beam energies, as shown in Figure 6.8. The dependence shown is basically linear, though there is scatter. The scatter is to be expected since the plotted potential amplitudes are the average amplitude of a particular solitary wave for a given simulation run. The general trend of having larger amplitudes when larger beam speeds are used can be explained by the greater free energy made available by the more energetic beams, which is converted into electrostatic potential energy by the solitary structures.

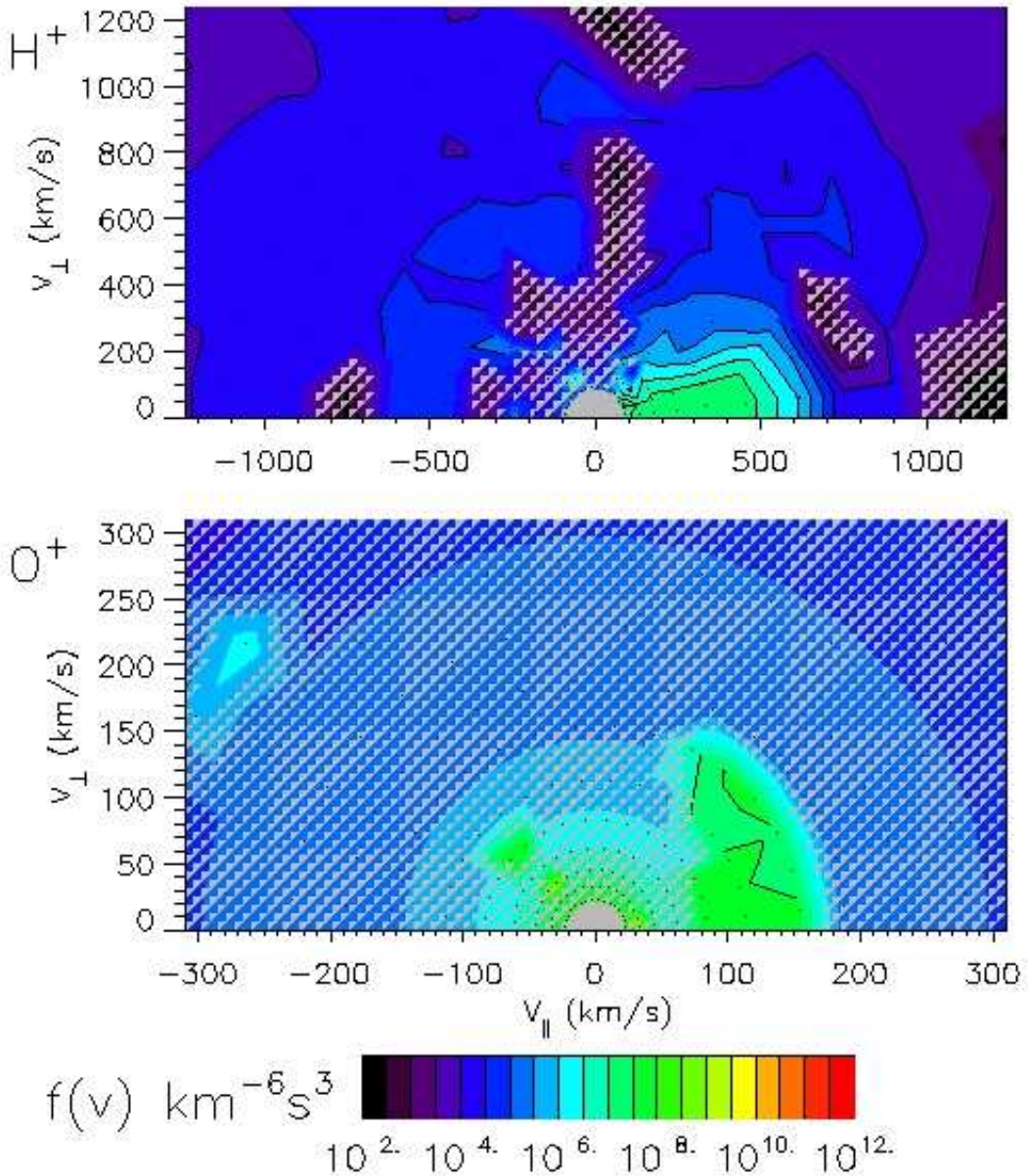

Figure 6.5: The TIMAS distribution plot for a region where solitary waves were detected. The top panel show the hydrogen ion beam with a speed of approximately 400 km s^{-1} and the bottom shows the oxygen beam with a beam speed of roughly 100 km s^{-1}. This plot is from *Dombeck et al.* [2001].

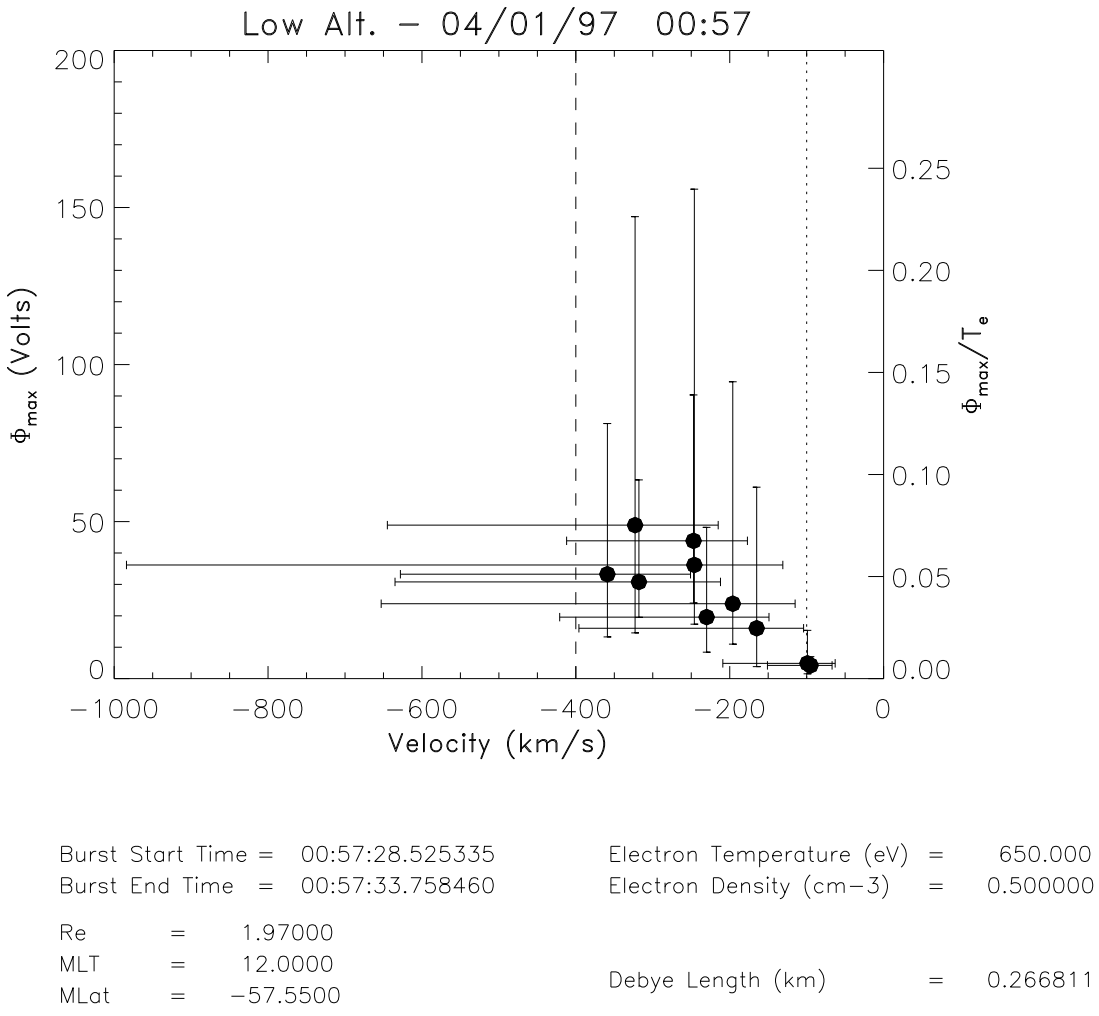

Figure 6.6: Solitary potential amplitude versus potential amplitude observations from Polar. The techniques used to make these observations is described in Chapter 5 and more detailed results of this type are presented in Chapter 7. The dashed and the dotted line in this plot represent the hydrogen and oxygen beam speeds respectively. This figure shows that the solitary wave speeds lie between the beam speeds. This plot is from *Dombeck et al.* [2001].

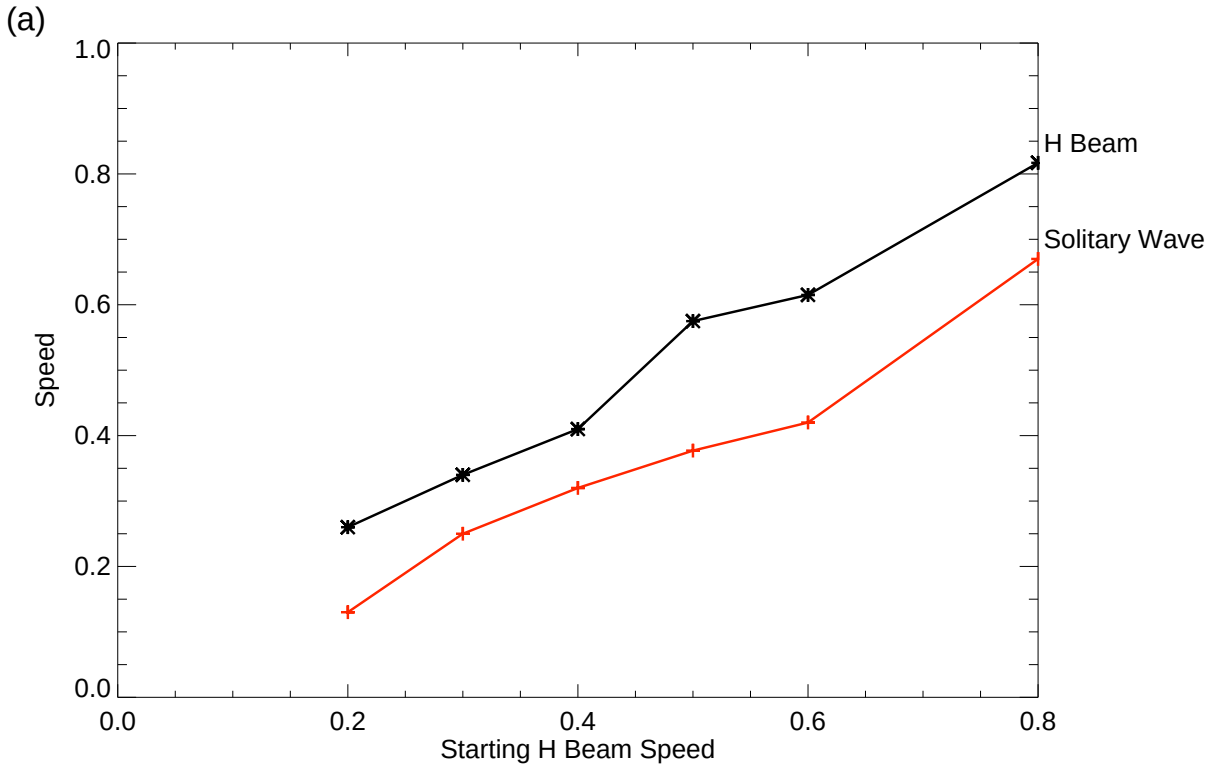

Figure 6.7: Plots showing solitary wave speeds and beam speeds at the time of the measured solitary waves versus starting hydrogen beam speed for (a) hydrogen beam only runs, (b) hydrogen and oxygen beam runs, (c) and hydrogen, helium, and oxygen runs ((b) and (c) are on following page). All speeds are normalized to the starting electron thermal speed. The beam speeds plotted are taken from the time when the solitary waves are present in the simulations. The beam speeds change during the simulation runs owing to interaction with the other species and with the applied electric field.

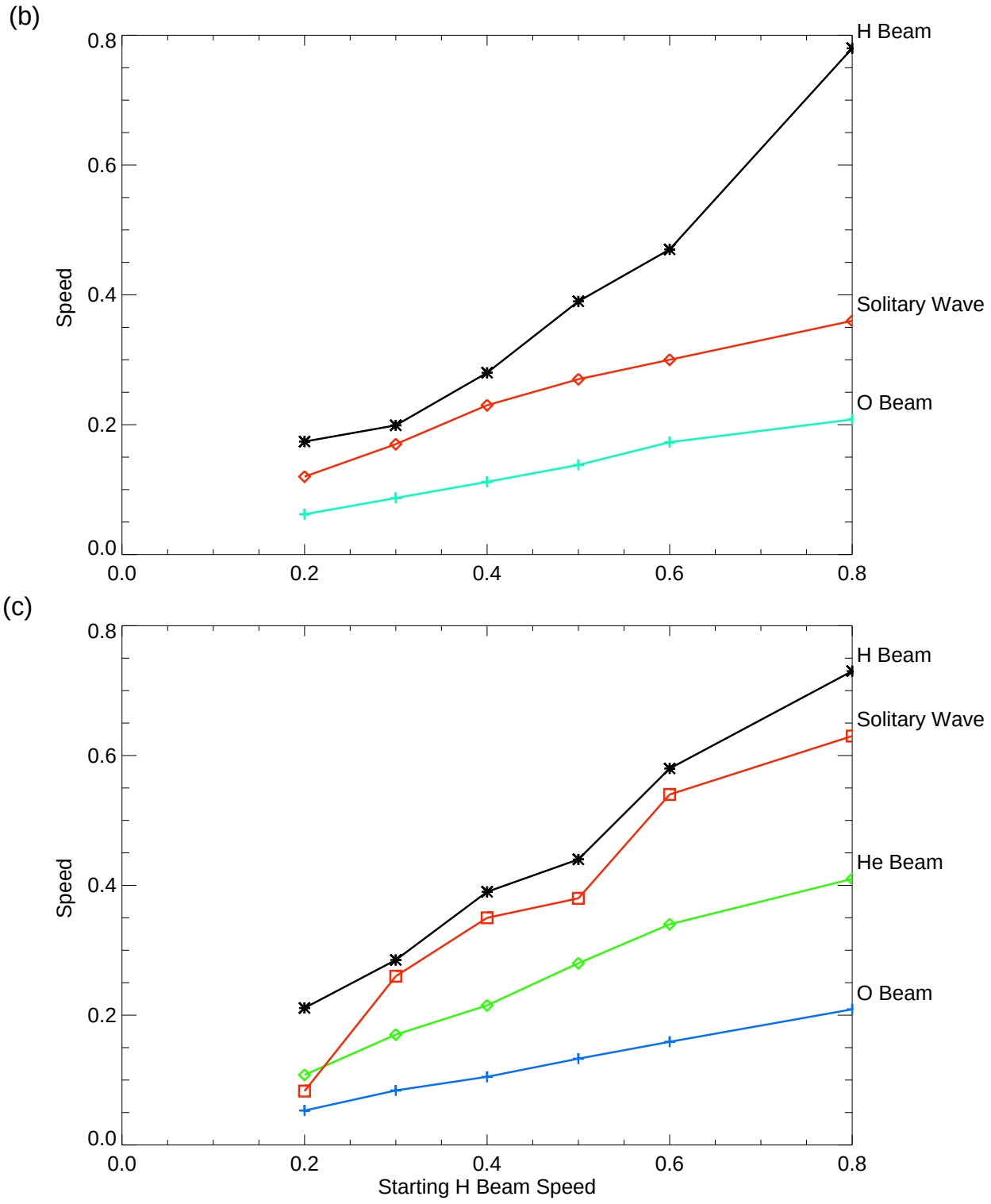

Figure 6.7 (continued)

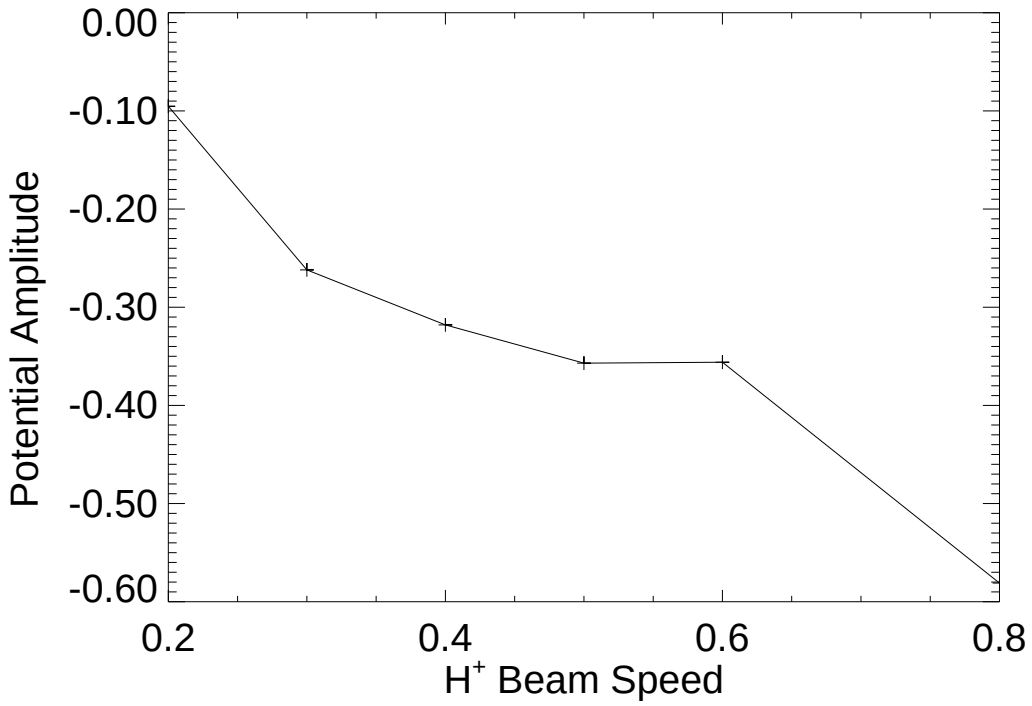

Figure 6.8: The electrostatic potential amplitude, in units of kT_e/e, versus starting hydrogen beam velocity, in units of v_{te}, plotted for each of the two beam cases that are plotted in Figure 6.7a. The electrostatic potential amplitudes plotted are the average amplitudes that developed for one solitary wave studied in each run, and they are normalized by the electron temperature at the time the solitary waves were present.

6.4 Discussion

6.4.1 Comparison to Theory

We have presented new results on ion solitary structures which differ from previous studies because the plasma parameters in the simulation are based on recent Polar and FAST data. The absence of cold plasma and the inclusion of oxygen ions distinguish this work from previous studies [*Barnes et al.*, 1985; *Marchenko and Hudson*, 1995]. Previous 1-D simulations which included cold plasmas and one ion beam found that solitary waves can form from linear ion acoustic waves that are pumped by the decay of ion beam modes [*Gray et al.*, 1991]. In our H^+ beam cases similar processes may be occurring, with the hot electrons providing the background population in place of the cold plasma. For the H^+ and O^+ beam cases, comparison with studies including both species is enlightening. Linear analysis of H^+ and O^+ beams of equal energies showed that two-stream instabilities can excite modes that propagate both parallel to [*Bergmann and Lotko*, 1986] and oblique to [*Bergmann et al.*, 1988] the background magnetic field. The modes excited by the two-stream instability are related to the acoustic and cyclotron modes of hydrogen and oxygen. The 1-D simulation studies including cold H^+ and O^+ beams found that the ion two-stream instability led to ion acoustic turbulence which grew nonlinearly into solitary waves [*Gray et al.*, 1992]. Similar processes are at work in the H^+/O^+ beam cases presented here, so that the solitary waves from both H^+ and H^+/O^+ cases are likely being formed from ion acoustic turbulence, and we classify these structures as "ion acoustic solitary waves." The term "ion acoustic solitary wave" is used instead of "ion acoustic soliton" because it is not clear that these structures meet the strict mathematical definition of the term "soliton."

The propagation speeds of the solitary waves in this study fit reasonably well with theory. Ion acoustic soliton theory predicted that the solitary waves should have a velocity equal to the ion acoustic speed relative to the reference frame of the cold ion species [*Lotko*, 1983], which is the same as the phase velocity of linear ion acoustic waves. This idea was later extended to

allow for the replacement of the cold background population by an ion beam of another species [*Qian et al.*, 1989]. When this theory was applied to simulation studies, it was found that the solitary structures slow down as their amplitude increases [*Hudson et al.*, 1983] (though the solitary waves shown here do not seem to slow down as they grow). So the difference between the speed of the solitary waves and the population they are riding on is expected to be less than the ion acoustic speed. Applying these principles to the H^+ beam case, it would be expected that the solitary waves would move with a speed somewhat less than 0.1 v_{te} slower than the hydrogen beam speed, since the hydrogen acoustic speed is 0.1 v_{te}. From Figure 6.7a it can be seen that the speed difference between the solitary waves and the hydrogen beam is of the order of the hydrogen acoustic speed, but for the higher speed beams the difference tends to be substantially greater than 0.1 v_{te}. The speed discrepancies for high initial beam speeds may be a result of the fact that the electrons are heated during the simulation, with this heating being more pronounced in the higher beam speed cases, which causes an increase of the hydrogen acoustic speed from its starting value. The solitary wave speeds in the H^+ and O^+ beam cases are also consistent with describing the structures as ion acoustic solitary waves. The speeds of the solitary waves are between the beam speeds of hydrogen and oxygen beams, as would be expected since the most unstable linear modes are in this region [*Bergmann et al.*, 1988]. Some shift in the phase velocities is expected in the context of these nonlinear simulations, but a reasonable first approximation is to expect that the solitary structures will propagate at speeds about equal to the hydrogen acoustic speed relative to one of the beam species. As shown in Figure 6.7b, for low beam speeds, the solitary wave speeds relative to the hydrogen beam speed are less than 0.1 v_{te}, while for the higher beam speeds they are much more than 0.4 v_{te}. The solitary wave speed and the oxygen beam speed lines track each other more closely, so it is possible that the solitary structures are hydrogen modes riding on the oxygen beam, instead of the hydrogen beam. This result is consistent with speculation that a second ion species could take the place of a cold background ion population [*Cattell et al.*, 1999]. The 0.05 - 0.15 v_{te} between the oxygen beam and the solitary waves is very similar to the velocity differences seen

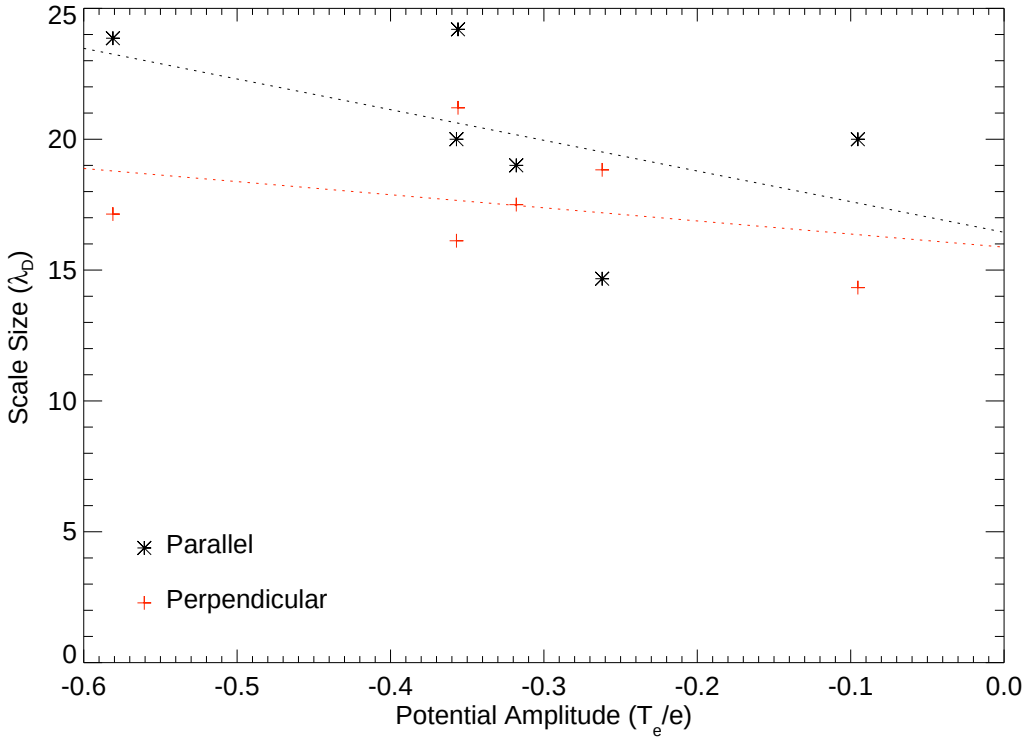

Figure 6.9: This plot shows the parallel (black asterisks and line) and perpendicular (red pluses and line) scale size in Debye lengths versus the potential amplitude. The results shown are for the same solitary waves shown in Figure 6.8. The dotted lines are linear fits to the results.

between the hydrogen beam and the solitary structures in the H^+ beam case.

The scale sizes for the observed solitary waves are not consistent with ion acoustic soliton theory. The scale sizes seen here were $\sim$ 20 λ_D in both directions, though on average the perpendicular scale sizes were somewhat smaller than the parallel. From *Zakharov and Kuznetsov* [1974] it is expected that these solitary waves would have scale sizes that scale as:

$$\frac{l_\perp}{l_\parallel} = \sqrt{1 + \frac{\rho_s^2}{\lambda_D^2}} = \left(1 + \frac{m_i}{m_e}\left(\frac{\omega_{pe}}{\Omega_e}\right)^2\right)^{\frac{1}{2}} \tag{6.1}$$

$\rho_s = c_s/\Omega_i$ is the ion acoustic scale size. *Marchenko and Hudson* [1995] pointed out that care must be taken when comparing scale size results to observations in cases like this when an artificial electron to proton mass ratio is used. So substituting into equation 6.1 for the case

of the simulation mass ratio yields a perpendicular to parallel scale size ratio of 1.49, while using the real mass ratio gives 4.86. So the predicted simulation value for the scale size ratio is greater than the simulation results of $\lesssim 1$. Also, if the solitary structures in these simulations were ion acoustic solitons, it would be expected that the physically observed solitary structures would be much larger in the perpendicular direction ($\sim 100\ \lambda_D$) than in the parallel direction. Another important consideration is that since the potential is averaged over time, the parallel size of the solitary waves may be exaggerated owing to the motion of the solitary waves along the magnetic field during the time period in which the averaging takes place.

Soliton theory predicts that the potential amplitude and scale size will be inversely related, but these simulation results (Figure 6.9) do not follow this relation. In Figure 6.9 both parallel and perpendicular scale sizes are directly proportional to the potential amplitude. The trend is not strong and it could be argued that the scale size is independent of the potential amplitude, but the trend is definitely not inversely proportional. These results are consistent with Polar observations of the potential amplitude/width relation which showed a definite trend of the solitary wave scale size being proportional to its width [*Dombeck et al.*, 2001]. Also, note that in Figure 6.9 the perpendicular scale sizes tend to be somewhat smaller than the parallel scale sizes. This may be an artifact of averaging over several iterations for the potential plots that are used to determine the scale size.

In contrast to previous results, solitary waves formed for cyclotron frequencies less than the electron plasma frequency [*Barnes et al.*, 1985; *Marchenko and Hudson*, 1995]. The difference in plasma parameters probably explains this discrepancy. The earlier work did not include O^+ or He^+ and did include cold plasma, which had a smaller gyroradius. The cold plasma would have been more strongly affected by the magnetic field, so that in those previous studies the magnetic field may have played a more important role in sustaining the solitary waves as seen in simulations of electron holes.

Since a cold background population was required to support BGK ion phase space holes in formulations where thermal fluctuations are invoked as a generation mechanism [*Tetreault*,

1991], it is unlikely that the solitary waves shown herein are BGK phase space holes of that type. Although it is possible that the oxygen beam could act as a cold population for the hydrogen beam, this would still not explain the structures seen in the hydrogen-only beam case. So we believe that it is unlikely that the structures we see are BGK ion phase space holes caused by thermal fluctuations in cold plasma. However, the results for the H^+ and O^+ beam cases do show structures that appear to be phase space vortices. It is possible that a cold population is not required and that thermal fluctuations in a hot plasma can generate phase space holes, though we are unaware of any theoretical work on this mechanism. It is also possible that the structures that we see are BGK phase space holes that have been generated by the two-stream interaction, by ion acoustic waves, or by ion cyclotron waves.

6.4.2 Comparison to Observations

The solitary waves observed in the simulations described herein are in agreement with recent Polar observations on a number of points. The speeds of the simulated solitary waves presented here are intermediate between the O^+ and H^+ beam speeds, consistent with those seen by Polar [*Dombeck et al.*, 2001]. This result is in contrast to previous simulation studies of ion-related solitary waves including cold plasma [*Marchenko and Hudson*, 1995], which resulted in much lower speeds. These lower speeds are not surprising, since there was a cold population to support them, and speeds of the order of bulk velocity or beam velocities would be expected when there is no cold plasma present. The speeds found in those simulations matched the observational results of *Boström et al.* [1988] from Viking which gave the solitary wave speeds as being between 5 and 50 km s^{-1}, much less than the ion beam speed. Note that recent FAST observations found that some of the highest amplitude solitary waves had speeds above the hydrogen beam speed [*McFadden et al.*, 1999b, 2002]. This is not observed in our simulations. The size of the simulated ion solitary structures, $\sim 10\ \lambda_D$ parallel to the magnetic field, is also consistent with the structure sizes seen by Polar [*Bounds et al.*, 1999; *Dombeck et al.*, 2001]. Although scale sizes perpendicular to the magnetic field have not been observed in as much

detail, owing to difficulties in determining sizes transverse to the direction of the motion, preliminary results [*Dombeck et al.*, 2001] suggest that the scale size in the perpendicular direction is slightly larger ($\sim$ 15 λ_D) than in the parallel direction. This result contradicts the scaling expected if these structures are ion acoustic solitons ($\sim$ 100 λ_D due to the artificial mass ratio), but it roughly agrees with the size directly measured in the simulations. The potential amplitudes, $e\phi/kT_e$, for the lower beam speeds presented here are of the order of 0.1, as has been seen by Polar [*Bounds et al.*, 1999; *Dombeck et al.*, 2001]. The potential amplitude was $\sim$ 0.1 in the lowest beam energy (0.2 v_{te} - 2 keV) case presented here. For the larger beam speeds the simulated potential amplitudes ($e\phi/kT_e \gtrsim 0.1$) are somewhat larger than the typical values seen by Polar ($e\phi/kT_e \lesssim 0.1$) [*Dombeck et al.*, 2001], but the beam speeds in those simulation runs were also greater than the Polar observations. The potential amplitudes for similar beam speeds are consistent between the simulations and the Polar data. Further comparison of these simulation results will be made in Chapter 7.

6.5 Conclusions

Recent spacecraft observations of ion solitary waves and plasma parameters in the auroral zone suggested the need to perform new simulations. When input parameters for the simulations are updated to exclude cold plasma, as determined from recent FAST observations, and include hydrogen and oxygen beams, solitary structures result which resemble the observed structures in the following ways:

1. The solitary wave speeds fall between the beam speeds of the hydrogen and oxygen beams, as would be expected if the two-stream instability was involved. Ion cyclotron waves, which may be generated due to the two-stream instability, are also present before the solitary waves form as would be expected if the solitary waves are caused by the two-stream instability.

2. The structure sizes observed in the simulation are $\sim$ 20 λ_D both parallel to and perpendicular to the magnetic field line. If these structures are assumed to be ion acoustic solitons, the perpendicular scale size to compare to the observations would be $\sim 100\ \lambda_D$, owing to the effects of the artificial mass ratio used in this study. Observations find the sizes to be of the order of $10\ \lambda_D$.

3. The potential amplitude of these ion solitary waves is similar to what has been seen in the observations, $e\phi/kT_e \sim 0.1$.

Further work needs to be done to better understand ion solitary waves in the magnetosphere. Among the unanswered questions is why ion solitary waves have only been observed in the auroral zone, while electron solitary waves have been observed in many regions. Earlier speculation that ion solitary waves were not observed at high altitudes owing to the lower ratio of Ω_e/ω_{pe} [*Cattell et al.*, 1999] has not been borne out by this study, though it is possible that differences in plasma distribution function shape explain the lack of observations of ion solitary waves in other regions. Simulations with smaller time steps and spatial scales need to be performed, in order to better see how the spatial structure of ion solitary waves evolves. Studies including He^+ and hot plasma sheet ions should be performed as well, since these populations are observed in upward beam regions.

Chapter 7

Polar Spacecraft Solitary Wave Survey

7.1 Introduction

In this chapter, results from a survey of solitary waves observed in the Polar EFI data will be presented. Previous observational studies of solitary waves have looked at smaller samples of solitary waves and have usually concentrated on either ion or electron solitary waves or looked at solitary waves in a specific region of the magnetosphere.

In this survey, all Polar spacecraft high-time resolution bursts for the year 1997 were searched for solitary waves. This year was chosen because 1997 was the year when the most high-time resolution bursts were taken. A year's worth of data was analyzed both to allow for a high number of bursts and to cover a range of regions of the magnetosphere (see Figures 5.1 and 7.1).

This survey of SW burst data lends itself to several types of analysis. In section 7.2 the spatial distribution of the bursts is examined. In section 7.3, properties of the solitary waves themselves are discussed. In particular, results for the velocities, potentials, and scale sizes of both low altitude ion solitary waves and high altitude electron solitary waves are presented.

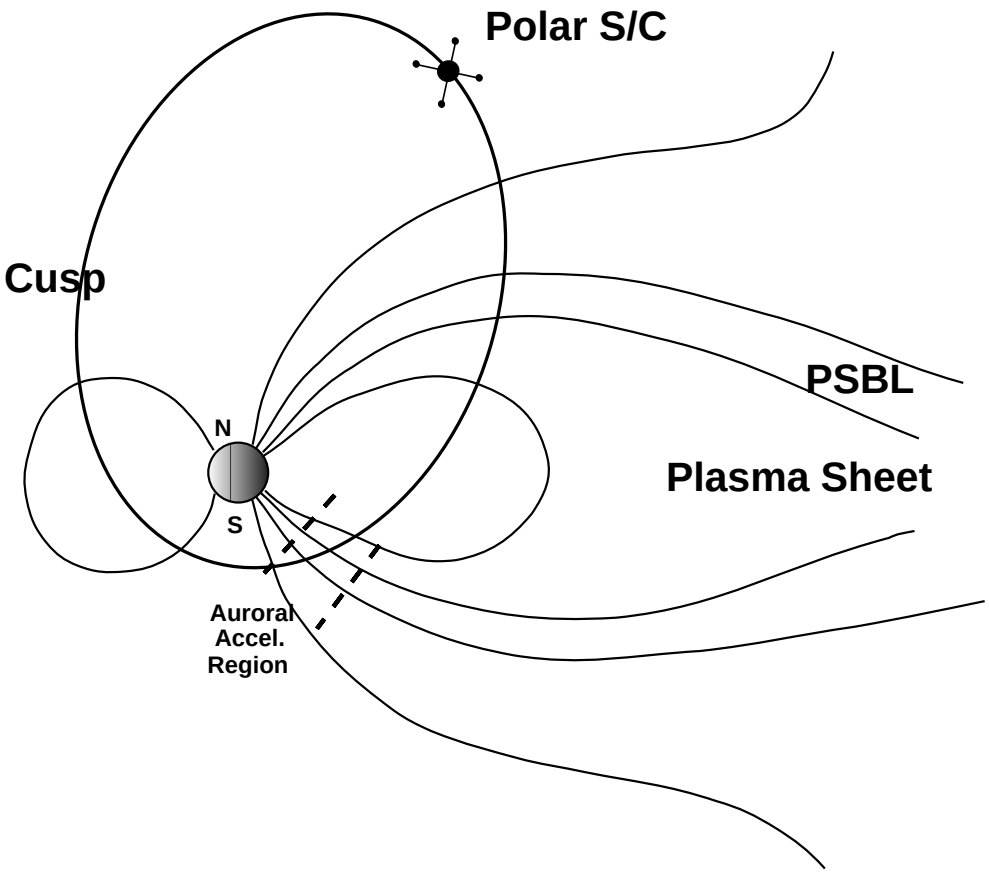

Figure 7.1: This figure shows the Polar spacecraft's approximate orbit in 1997 superimposed on a diagram of the magnetosphere (adapted from A. Keiling).

7.2 Spatial Distributions of Bursts

The spatial distribution of bursts examined in this study are shown in Figure 7.2 for the equatorial plane, Figure 7.3 for the XZ plane, and Figure 7.4 for the YZ plane in Geocentric Solar Ecliptic (GSE) coordinates (the plot of the YZ plane looks similar to the plot of the XZ plane). In GSE coordinates, the origin of the coordinate system is the center of the Earth, the X axis is defined by the line from the Earth to the Sun, the Z axis is defined as being perpendicular to the ecliptic plane, and the the Y axis points opposite the direction of the motion of the Earth around the Sun.

The most striking feature of these plots is the regular circular patterns in Figure 7.2. These patterns are the artifacts of Polar EFI's burst selection criteria. EFI takes high-time resolution data constantly and stores the data in an onboard memory buffer, but due to telemetry constraints that data is sent back to Earth for only selected bursts [*Harvey et al.*, 1995]. In the burst selection mode that EFI was in for 1997, three high-time resolution bursts were saved per orbit. In order to ensure that high-time resolution data were saved for multiple regions of the magnetosphere, one of the burst selection criteria divides Polar's orbit (see Figure 7.1) into three regions and requires one burst in each of these regions in each of Polar's orbits. One region is the low altitude portion of Polar's orbit in the auroral zone and the other two portions equally divide the high altitude portion, with these two portions corresponding to dayside and nightside or dawnside and duskside depending on the plane of Polar's orbit. Within a given region the time period with the largest amplitude electric field is The circular patterns are a results of the interaction of the burst selection criteria and the precession of Polar's orbit.

The circular pattern in the center of Figure 7.2 is the low altitude bursts, while the outer two circles are the high altitude bursts. The precession of Polar's orbit in the XY GSE plane takes less than a year, which causes the circular patterns to overlap. The high altitude circular patterns do not close on themselves because besides precessing in the XY GSE plane, Polar's orbit also precesses toward the XY plane. Figure 7.5 shows the GSE position of the bursts plotted against time. The three separate burst selection regions and the periodic nature of the X

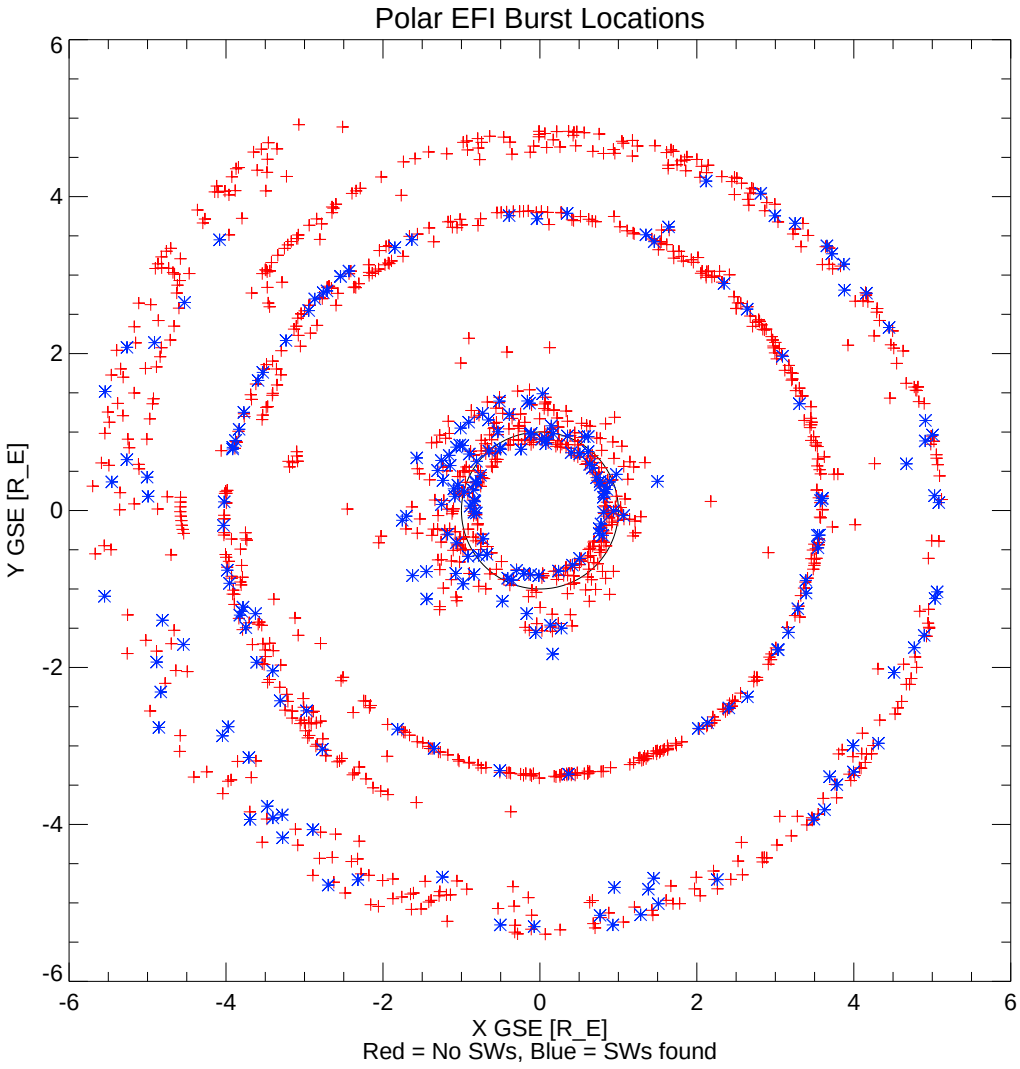

Figure 7.2: Distribution of Polar spacecraft high-time resolution bursts in the XY plane in GSE coordinates. The positions of the bursts are plotted in units of the radius of the Earth (R_E). The red +'s stand for bursts where no solitary waves were found and the blue *'s standing for burst where solitary waves were found.

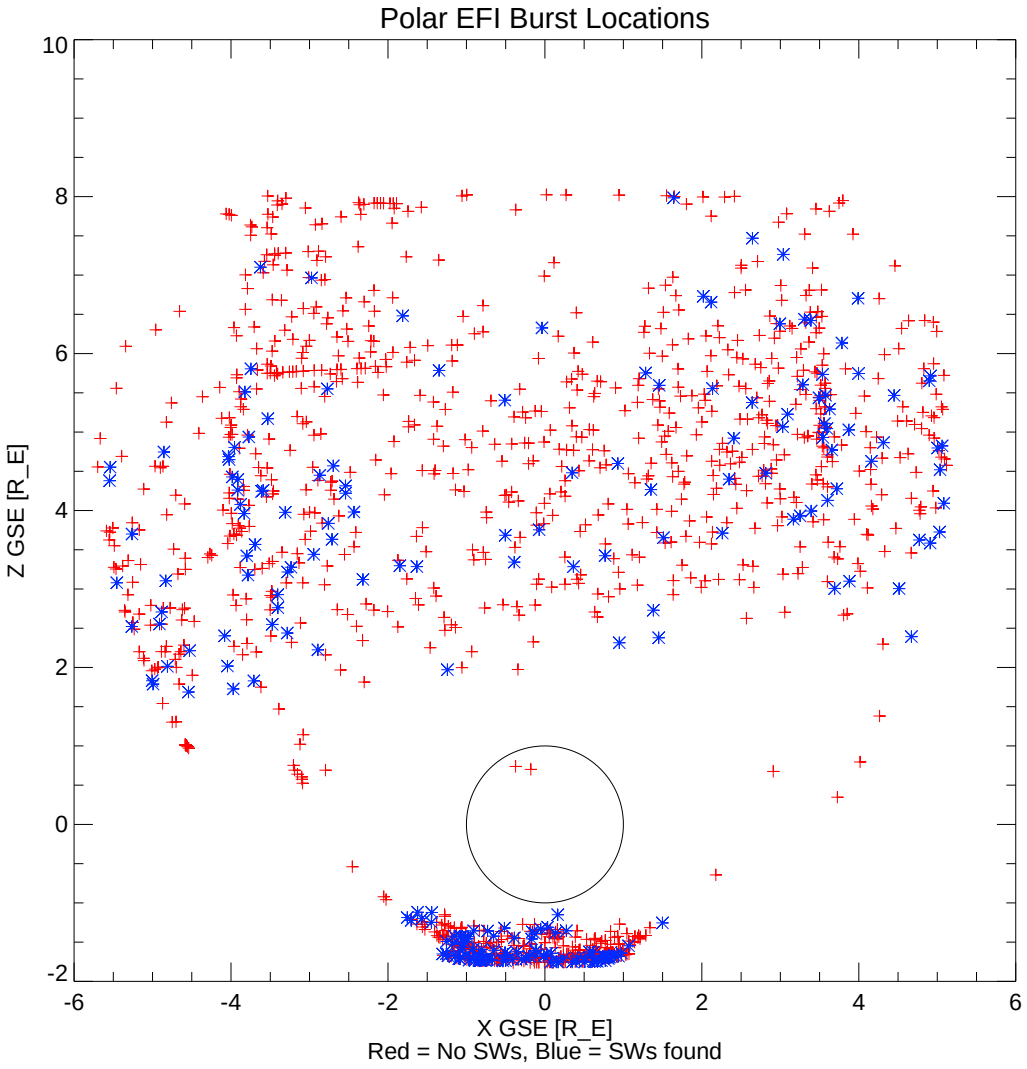

Figure 7.3: Distribution of Polar spacecraft high-time resolution bursts in the XZ plane in GSE coordinates. The positions of the bursts are plotted in units of the radius of the Earth (R_E). The red +'s stand for bursts where no solitary waves were found and the blue *'s stand for bursts where solitary waves were found.

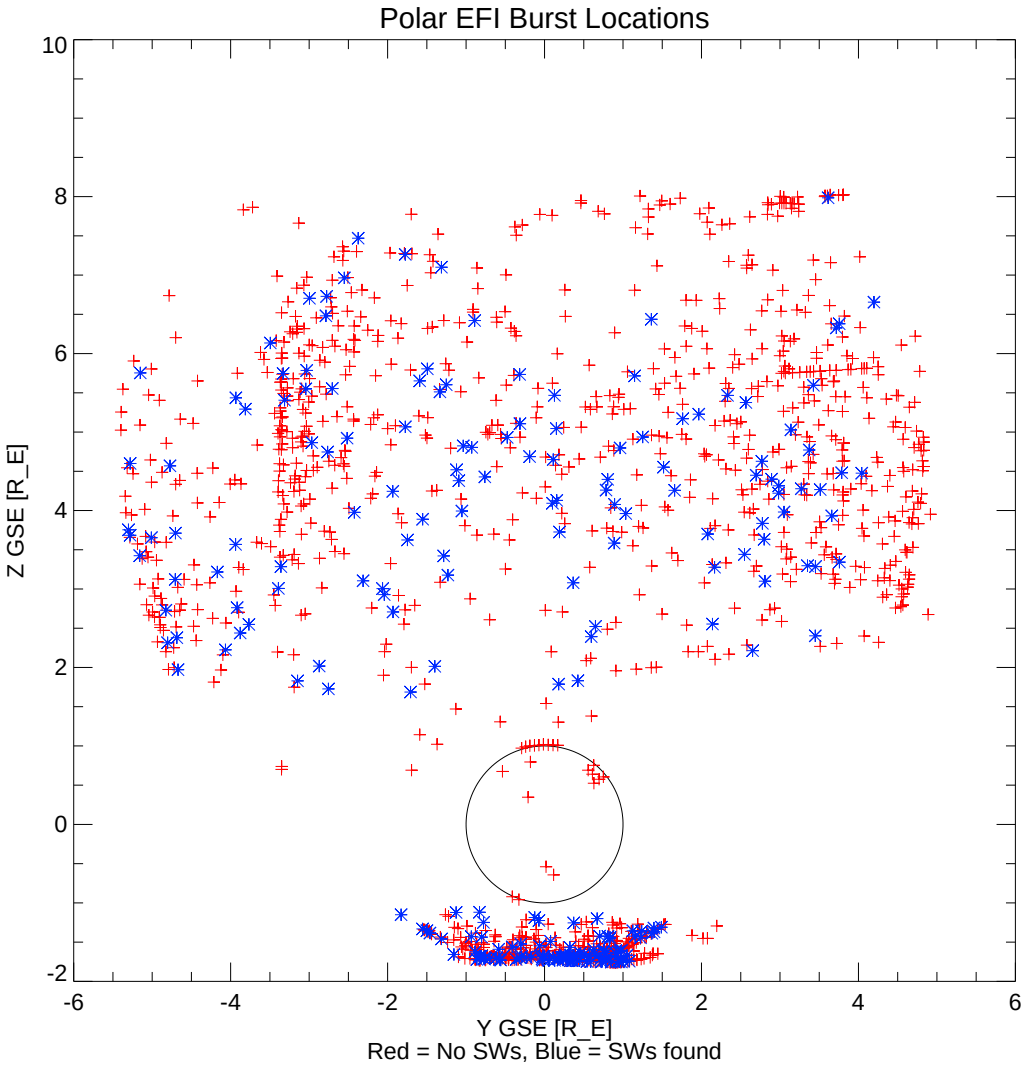

Figure 7.4: Distribution of Polar spacecraft high-time resolution bursts in the YZ plane in GSE coordinates. The positions of the bursts are plotted in units of the radius of the Earth (R_E). The red +'s stand for bursts where no solitary waves were found and the blue *'s stand for bursts where solitary waves were found.

Group of Bursts	Number of Bursts
All bursts in survey	1367
High altitude bursts	935
Low altitude bursts	432
High altitude burst with solitary waves	126
Low altitude bursts with solitary waves	103

Table 7.1: Statistics of Burst Survey

and Y coordinates of the bursts are evident in this figure.

Besides showing where Polar's bursts occurred, Figures 7.2 – 7.5 also show in which bursts solitary waves were detected by the automatic program, Delaytime, described in Chapter 5. Some summary statistics about the bursts are also presented in Table 7.1. It is apparent that low altitude bursts were more likely to have solitary waves detected by Delaytime than high altitude bursts. The selection criteria used by Delaytime explain at least part of the difference. Waves seen at high altitude are on average smaller at high altitudes than at low altitudes, so it less likely for high altitude waves to meet the minimum amplitude requirement. The angle requirements are also easier to meet in the low altitude case because Polar's spin plane tends to stay closer to the plane of the magnetic field at low altitudes. Since the selection criteria places constraints on the total angle between the spin plane booms and the magnetic field, minimizing the angle between the magnetic field and the spin plane allows for a larger range of allowed angles with in the spin plane for the booms. Due to these differences in the effects of the selection criteria between the high and low altitudes, it is difficult to make any conclusion about the relative detection frequency of solitary waves in high and low altitudes.

Spatially within the low and high altitude regions the distribution of bursts is fairly random. Some regions seem to have either an excess or deficit (such as the region around y=4 in Figure 7.2) in the number of bursts containing solitary waves, but for several regions it is difficult to make any conclusions based on these clusters of burst. First, there is limited coverage of any

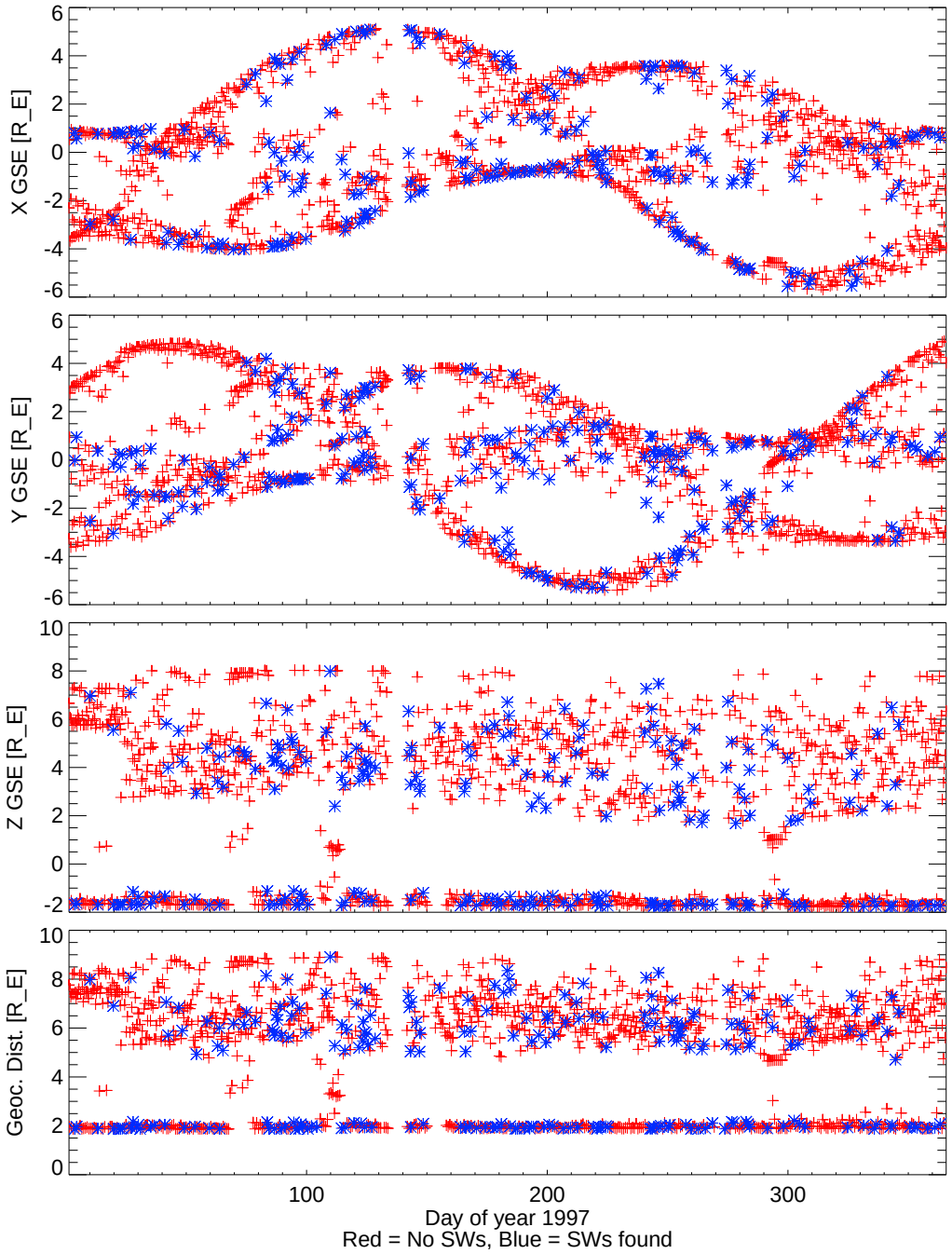

Figure 7.5: Plots of the location of Polar spacecraft bursts in GSE coordinates and total geocentric distance (distance from the center of the Earth) versus time in the year 1997. The positions of the bursts are plotted in units of the radius of the Earth (R_E). The red +'s stand for bursts where no solitary waves were found and the blue *'s standing for burst where solitary waves were found.

particular region, so the statistics involved in breaking the plots down and focusing on a particular small region are not very convincing. It is quite likely that the visible clusters were caused by simple statistical fluctuations. Furthermore, no attempt to normalize for magnetospheric conditions has been made in these plots. Since the magnetosphere is a dynamic system in which the coordinates of magnetospheric regions vary depending on a variety of factors, ideally the burst locations would be mapped to their invariant regions with the magnetosphere, instead of using their physical coordinates. In this study, no attempt was made to track the global state of the magnetosphere, so further analysis of the locations of bursts within the magnetosphere will have to wait for further study.

7.3 Solitary Wave Results

The solitary waves from this burst survey have been divided based on two criteria: altitude and whether they are associated with ions or electrons. The cut between low and high altitude was set at a geocentric distance of 3 R_E for this survey, since that was a natural cut in the burst location data (See the bottom panel of Figure 7.5).

Separating ion solitary waves from electron solitary waves is a more difficult task. Several methods were attempted before the following system was arrived at. First, negative potential was required for ion solitary waves since ion solitary waves are expected to have negative potentials. Next, since solitary waves are expected to have lower speeds, ion solitary waves were required to have speeds and uncertainties that were finite and had the same sign. The reasoning behind why the ion solitary waves are determined this way goes back to how solitary wave velocities are determined (see Section 5.2.2). The velocities depend on the inverse of the time delay determined from cross correlation and the time delay is only allowed to take on discrete multiples of 25 μs. So, the fastest solitary waves for which a speed determination can be made have time delays of $\pm$ 25 μs (depending on the direction of propagation of the solitary wave) and time delays of 0 s are not uncommon. For the fastest measured solitary

	Ion solitary waves	Electron solitary waves	Total solitary waves
Low Altitude	153	213	366
High Altitude	30 (18)	1286	1316
Total	183	1499	1682

Table 7.2: Solitary Wave Types in Survey

waves, it is common for the error ranges on the speeds to extend to both positive and negative values, which means that the direction of propagation of the solitary wave is uncertain. From the dependence of the potential amplitude on the solitary wave speed (Equation 5.8), it is clear that if the direction of the solitary wave is uncertain, then the polarity of the potential amplitude is also uncertain. So the velocity criterion is equivalent to requiring that, up to the limits of the uncertainty on its velocity, the solitary wave has a negative potential amplitude. Edge case solitary waves with lower limits on time delay of one point typically have measured speeds of $\sim$ 1000 km s^{-1}, which is a higher speed than is expected for ion solitary waves. Solitary waves with speeds of 1000 km s^{-1} that are classified as ion solitary waves, may have been misclassified or there may be very energetic ion beams, but in either case Figure 7.6 shows that there are few of them. Under this system, any solitary waves that do not meet the potential amplitude and velocity criteria outlined above are classified as electron solitary waves. Other velocity constraints were experimented with, including dividing the solitary waves into slow (definitely ion), intermediate (mixture of ion and electron), and high (definitely electron) speed solitary waves, but the results were not any more informative.

The numerical results of how this classification scheme divides the solitary waves are summarized in Table 7.2. Notice that 30 solitary waves are classified as high altitude ion solitary waves. High altitude ion solitary waves have not been reported previously, so these solitary waves were examined more closely. When examined more closely, 12 of the 30 were classified as questionable solitary waves based on their wave forms or the likelihood that they were part of a periodic wave based on the nearby electric field signature. Of these 18 high altitude ion

solitary waves, 12 had speeds higher than 900 km s^{-1}. Though their error bars did not reach the border line of 0 s time delay that is used for separation of ion solitary waves, the error bars are close. So it is likely that these solitary waves that have been classified as high altitude ion solitary waves are actually misclassified electron solitary waves. The misclassification would be due to incorrect signs on the velocities of these solitary waves, which also flipped the sign on the potential amplitude. The remaining 6 high altitude solitary waves are likely high altitude ion solitary waves, but due to their low number compared to the number of solitary waves in this survey more study of these high altitude ion solitary waves is required. In particular, it would be useful to look at TIMAS and HYDRA data for the most reliable of the ion solitary waves and see if ion beams are present while these solitary waves are present. Examination of the TIMAS data for 2 of the 6 high altitude ion solitary waves has shown shown weak ion beams moving in the correct direction to explain these structures.

In the remainder of this chapter, results for two groups of solitary waves will be presented. Survey results for low altitude ion solitary waves, for which simulation results were presented in Chapter 6, will be shown. Results for high altitude electrons solitary waves, which make up the majority of the solitary waves observed in this study, will also be shown.

7.3.1 Velocity

Velocity is an important feature for characterizing solitary waves for comparison to theory and to other observations of solitary waves. Figure 7.6 shows histograms of the velocity of both the low altitude electron solitary waves and the high altitude electron solitary waves. The average speed of approximately 300 km s^{-1} is consistent with previous studies of ion solitary waves using Polar spacecraft data [*Bounds et al.*, 1999; *Dombeck et al.*, 2001]. Speeds of this order would tend to be between the hydrogen and oxygen beam speeds observed in this region [*McFadden et al.*, 1999a], although detailed ion distribution data has not been analyzed for all of the events in this study.

Since the speeds of the electron solitary waves are so near to the limits of this method of

determining speed, it is more difficult to make definite conclusions about these results. It is clear from Figure 7.6 that the vast majority of the solitary waves that have been classified as electron solitary waves have time delays of 0 or 1 time point (0 or 25 μs). Speeds of this order are consistent with FAST spacecraft observations slightly lower in the auroral acceleration region [*Ergun et al.*, 1998b] and with Polar PWI observations which have higher time resolution but saturate at an amplitude a few mV/m [*Franz et al.*, 1998].

Figure 7.7 shows the potential amplitude versus velocity for the low altitude ion solitary waves in this study. The bulk of the points in this plot fall on a line, making it evident that the solitary wave speed is proportional to the potential amplitude. This matches the previous results for the simulation shown in Figure 6.8. There is some noticeable scatter in Figure 7.7. In particular, most of the solitary waves with positive velocities are probably electron solitary waves that were misclassified due to the incorrect sign on their speed leading to the incorrect sign on their potential. Ion solitary waves are expected to have negative velocities, which correspond to motion away from the ionosphere in our sign convention, since that is the direction that auroral ion beams propagate.

The potential amplitude versus velocity for the high altitude electron solitary waves (Figure 7.8) is less clear. There is quite a bit of scatter, largely due to the fact that the direction of propagation is so uncertain for the high speed solitary waves. Still despite the uncertainty, roughly 75 percent of the electron solitary waves that have positive potentials. The vertical bands evident in this plot are due to the fact that at high speeds the angle constraints on when solitary waves can be detected leads to discrete bands of speeds that can be measured and other ranges that cannot be measured. It is still apparent in this plot that there is a general trend of speed being proportional to potential amplitude.

7.3.2 Potential Amplitude

The potential amplitude of a solitary wave plays an important role in our observations of solitary waves since it is a principal way we discriminate between ion (negative potential amplitude) and

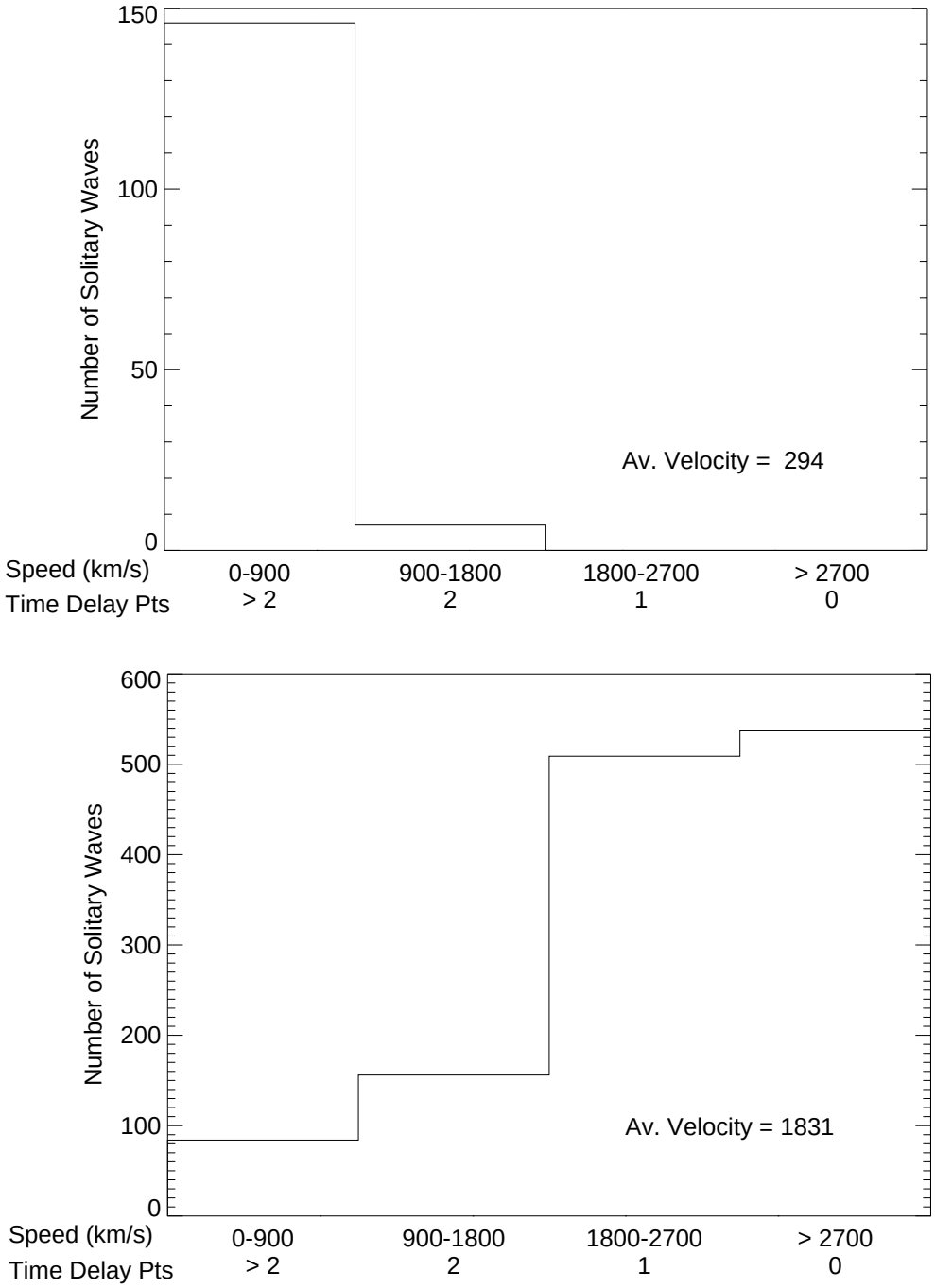

Figure 7.6: These plots show histograms of the absolute value of velocity. The upper panel shows results for the low altitude ion solitary waves, while the lower panel shows results for the high altitude electron solitary waves. The velocities are separated into bins based upon the number of of splined time data points their time delay was equal to. Note that the average velocity does not include any of the zero time delay (infinite speed) solitary waves.

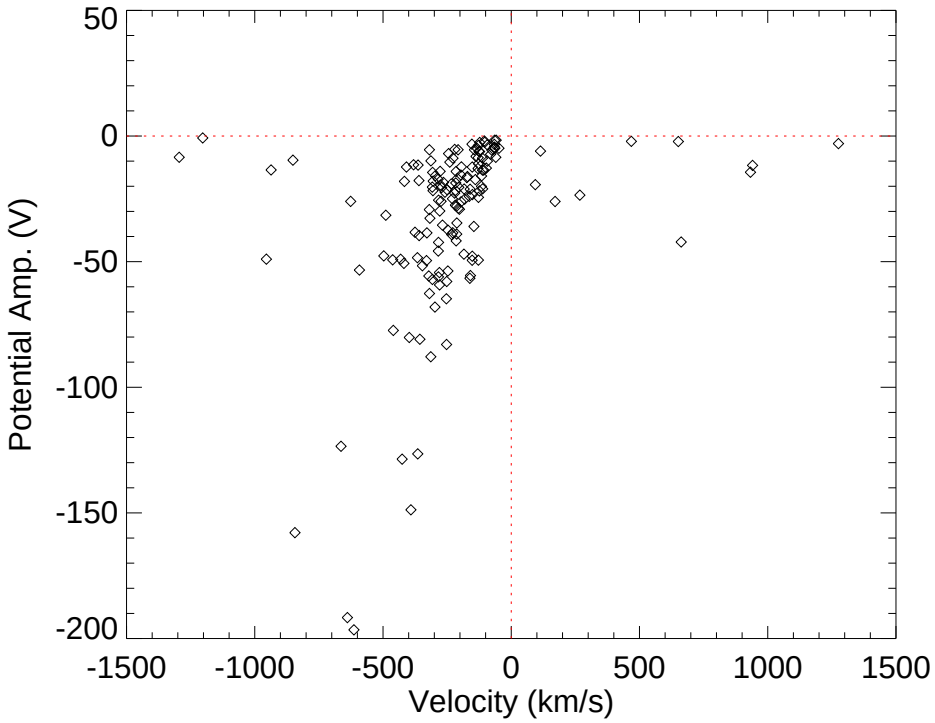

Figure 7.7: This figure shows the solitary wave speed versus potential amplitude for the low altitude ion solitary waves in this survey.

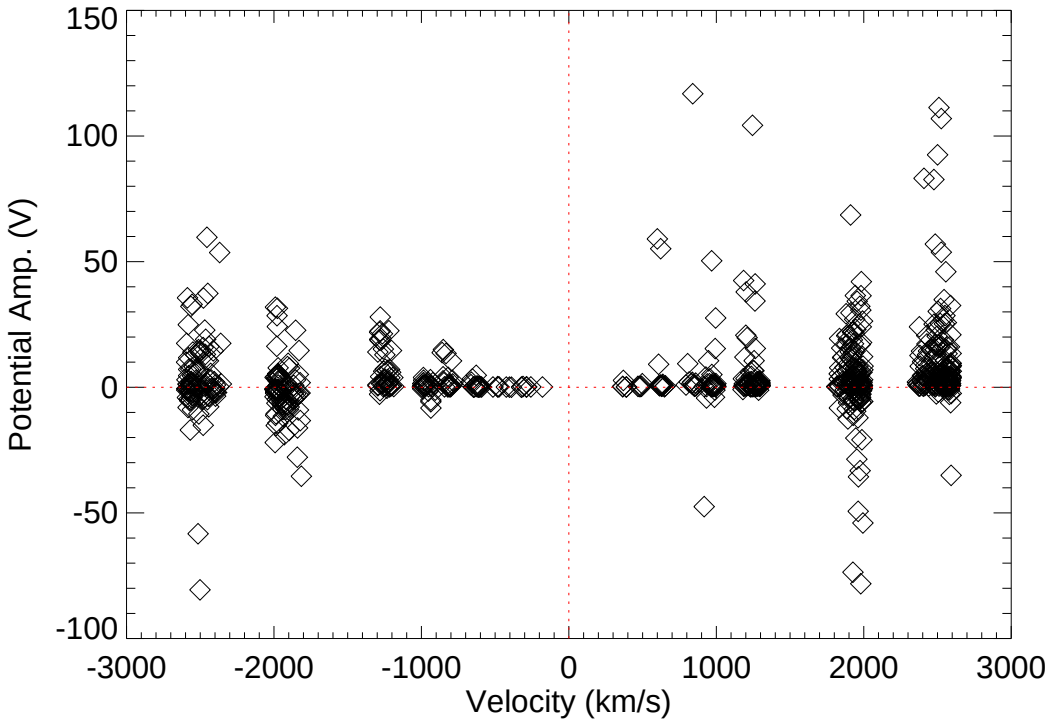

Figure 7.8: This figure shows the solitary wave speed versus potential amplitude for the high altitude electron solitary waves in this survey.

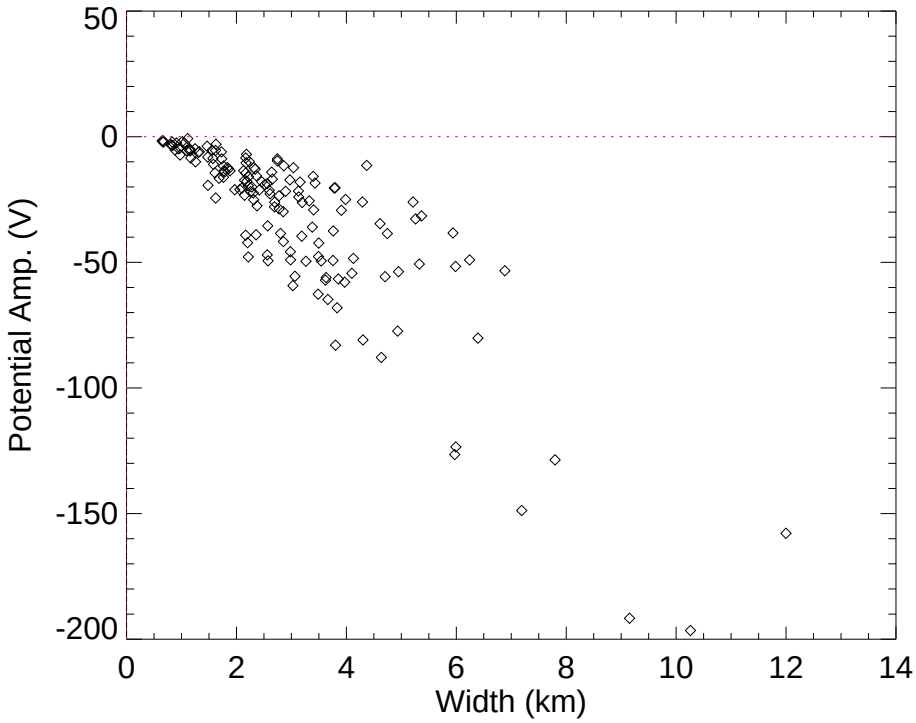

Figure 7.9: This figure shows potential amplitude versus width for the low altitude ion solitary waves.

electron (positive potential amplitude) solitary waves. Figure 7.9 shows the potential amplitude versus width for the low altitude ion solitary waves in this survey. There is a definite trend for the potential amplitude being proportional to the width of the solitary waves, as was the case in previous Polar observations [*Dombeck et al.*, 2001]. These results also agree with the solitary wave simulations (Figure 6.9). This result is important because it directly contradicts ion acoustic soliton theory which predicts that potential amplitude and the width of the soliton structures should be inversely proportional. On the other hand, from BGK theory the potential amplitude and width would be expected to be proportional [*Tetreault*, 1988]. So these results support the idea that ion solitary waves are a BGK mode.

The plot of potential amplitude versus solitary width (Figure 7.10) is not as clean for the

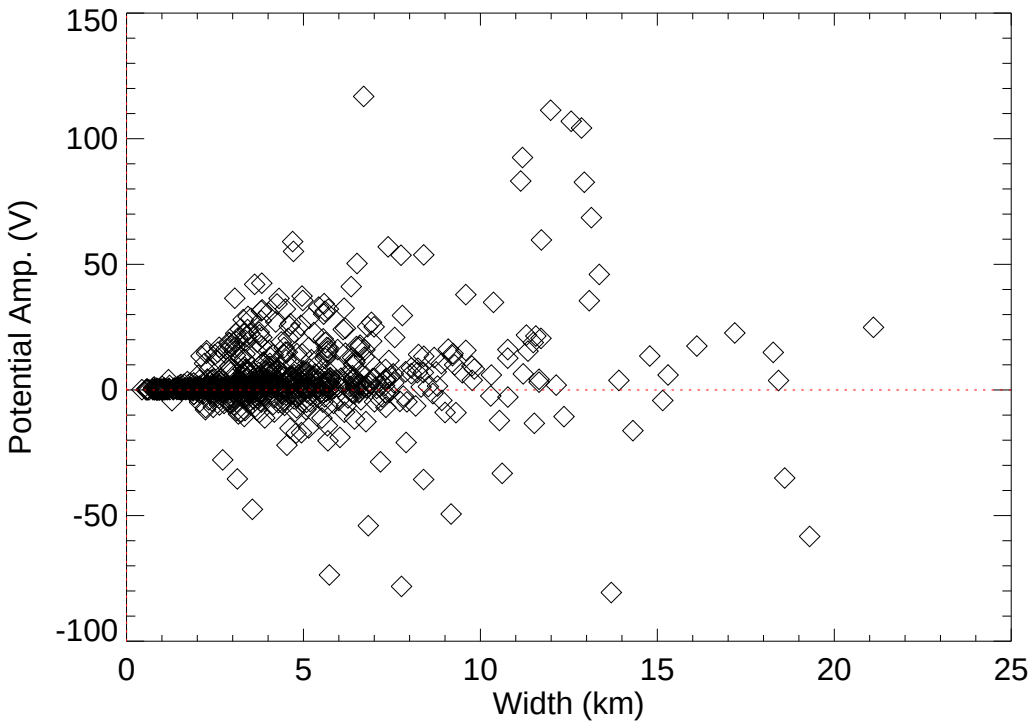

Figure 7.10: This figure shows potential amplitude versus width for the high altitude electron solitary waves.

high altitude electron solitary waves. The negative potentials for this plot are most likely due to solitary waves for which the direction is uncertain and the sign of the potential amplitude is flipped. The trend of direct proportionality between potential amplitude and width is the same as with the ion data, though there is more scatter. These results are consistent with BGK theories and simulations of electron solitary waves [*Muschietti et al.*, 1999b].

7.3.3 Potential Difference

The potential difference across solitary waves plays a prominent role in how the solitary waves are affecting the particles in their surroundings. Figure 7.11 shows histograms of the potential difference measured across the solitary waves observed in this study. Though the distribution

of potential differences is fairly symmetric in the low altitude ion solitary wave case, there is a small tendency toward positive potential differences. Since these ion solitary waves are traveling up the magnetic field line in the auroral acceleration region, a positive potential difference corresponds to the potential being higher after the solitary wave passes. In terms of the solitary wave's position on the magnetic field line, the ion solitary wave's potential is higher on its Earthward side. The sense of this potential difference is the same as the sense of the electrostatic potential drop along the magnetic field line in the auroral acceleration region, so these results suggest that the low altitude ion solitary waves may be weakly supporting this auroral potential drop. Though this nearly symmetric distribution is consistent with previous studies of ion solitary waves that suggested these structures had no little or no net potential [*Bounds et al.*, 1999; *Dombeck et al.*, 2001], it is interesting that there is a tendency towards a small net potential change seen here. These results are very similar to an earlier study of Viking data which also found a small net potential, but concluded that the size was too small to be a significant contributor to the auroral potential drop [*Mälkki et al.*, 1993].

The potential difference for the high altitude electron solitary waves (lower panel of Figure 7.11) is more difficult to interpret. Due to the uncertainty of the direction of propagation of many of the electron solitary waves, the sign of the potential difference is also uncertain. For this reason, the high altitude electron solitary wave results can only be examined in terms of the magnitudes of the potential drops, not in terms of a possible net potential along the magnetic field line caused by these structures. It is interesting to note that the potential differences seen here are approximately the same magnitude seen in the ion solitary waves and that the magnitudes are predominantly negative.

7.3.4 Parallel Size

Figures 7.12 and 7.13 shows the parallel scale size of the solitary waves from this study. The parallel size in this study is taken as the total length along the magnetic field, as opposed to some studies where the Guassian half-width is used. The sizes in kilometers are quite similar

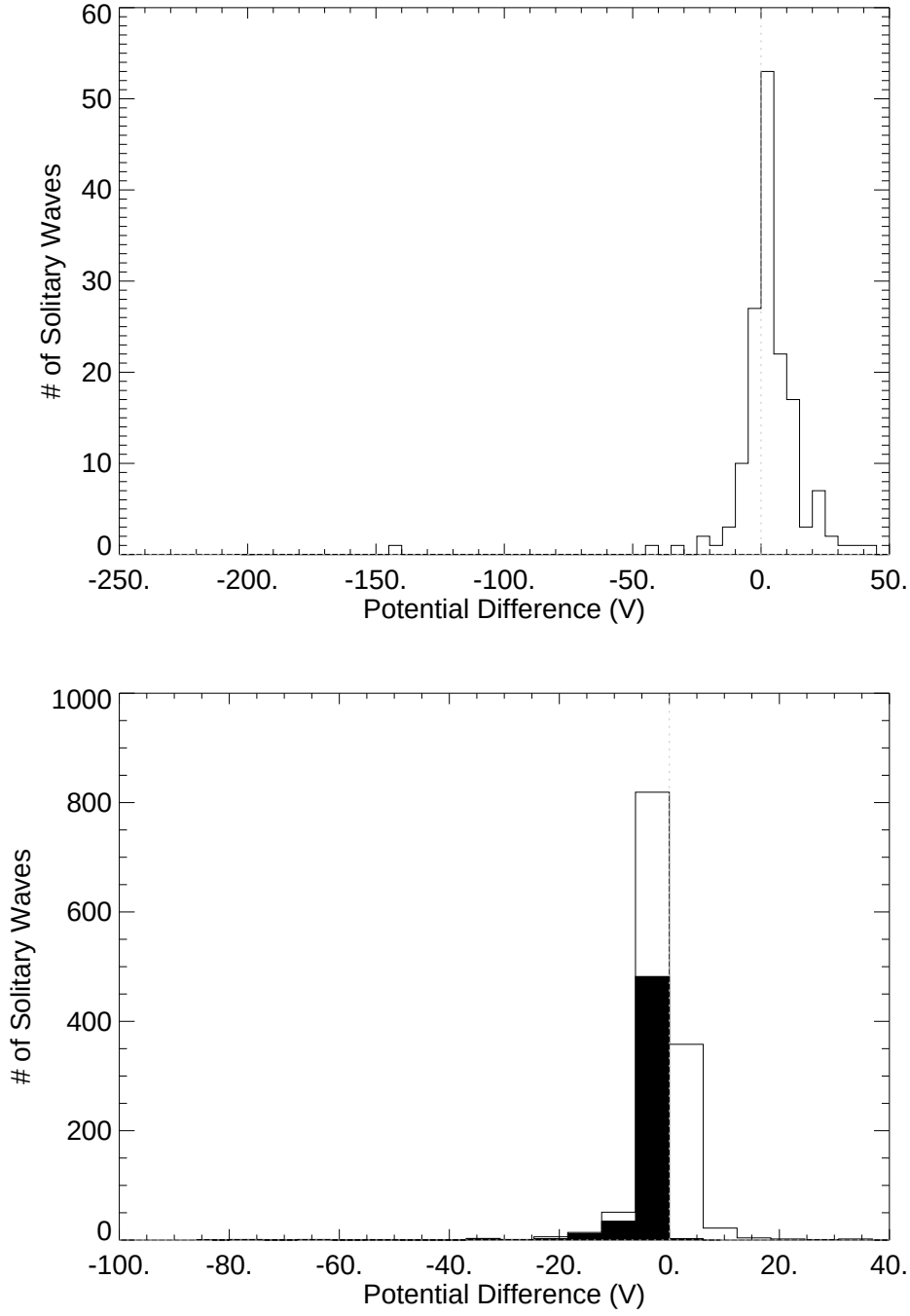

Figure 7.11: This figure is a histogram of the potential difference across solitary waves, with the upper panel being for the low altitude ion solitary waves and the lower panel begin for the high altitude electron solitary waves. The black regions of the histogram represent solitary waves that had a time delay 0 s.

	Max	Min	Mean	Median	Std. Dev.
Low Altitude Ion	122	3.5	27.0	21.9	21
High Altitude Electron	2500	1.3	37.8	13.6	146
All Electron	13100	1.3	46.4	14.8	364

Table 7.3: Statistics for normalized solitary wave parallel sizes (all values in λ_D).

for both the low altitude ion and high altitude electron solitary waves, with typical sizes being about 4 km for both, but the normalized sizes differ. The wider range of the sizes relative to typical values in both the ion and electron cases is likely due to uncertainties in the plasma parameters used to normalize the data. In fact, in the normalized electron cases the plots are cut off at 200 Debye lengths to focus on the majority of the data. The parallel sizes for the electron solitary waves ranges up to 13000 Debye lengths, though only 28 and 33 data points have values above 200 Debye lengths in the high altitude electron and all electron solitary wave cases, respectively. A closer inspection of the data showed that most of the data points with very high sizes came from several bursts, which supports the idea that these high values were caused by errors in the plasma parameters used for normalization. Table 7.3 shows the statistics for the normalized parallel size data. The size of the tails on the distribution for the parallel size make the median values more appropriate than the mean values for use as typical values. So the typical parallel sizes were 22 λ_D, 14 λ_D, and 15 λ_D, for the low altitude ion, for the high altitude ion, and for all electron solitary waves.

These results are consistent with previous estimates of parallel scale sizes for ion solitary waves [*Bounds et al.*, 1999; *Dombeck et al.*, 2001]. Previous studies of electron solitary waves had lower parallel sizes for these structures. A previous Polar spacecraft study using the PWI to examine electron solitary waves reported parallel sizes of 400-4000 m (4-40 λ_D) [*Franz et al.*, 1998]. A FAST study reported sizes of $\sim$ 500 m (8 λ_D), though those results are for low, not high, altitude electron solitary waves so the discrepancy may be due to variation in the plasma parameters [*Ergun et al.*, 1998b, a].

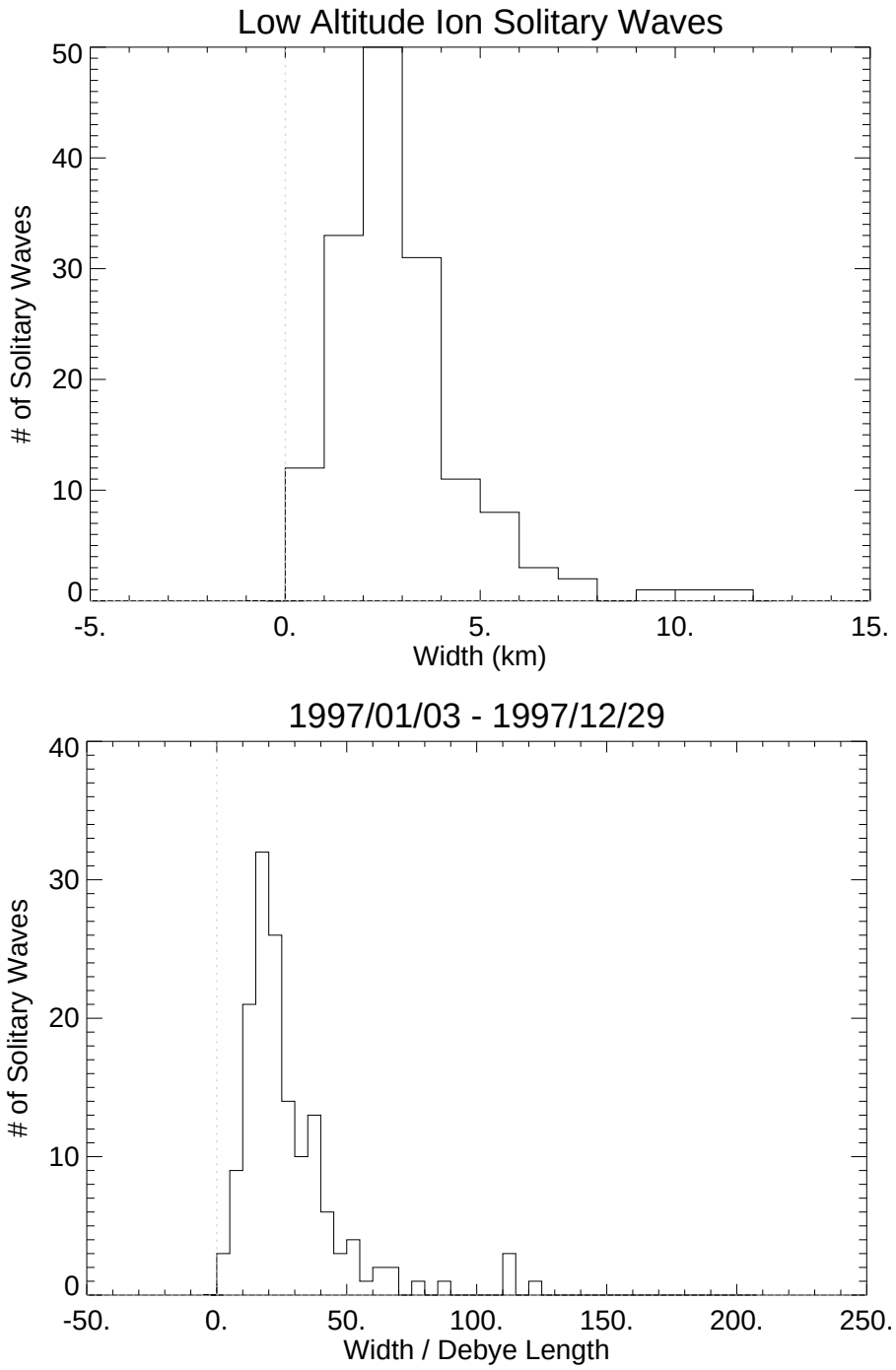

Figure 7.12: This figure shows histograms of the parallel scale size of the low altitude ion solitary waves. The units for the data in the upper panel km, while the lower panel is normalized by the Debye length.

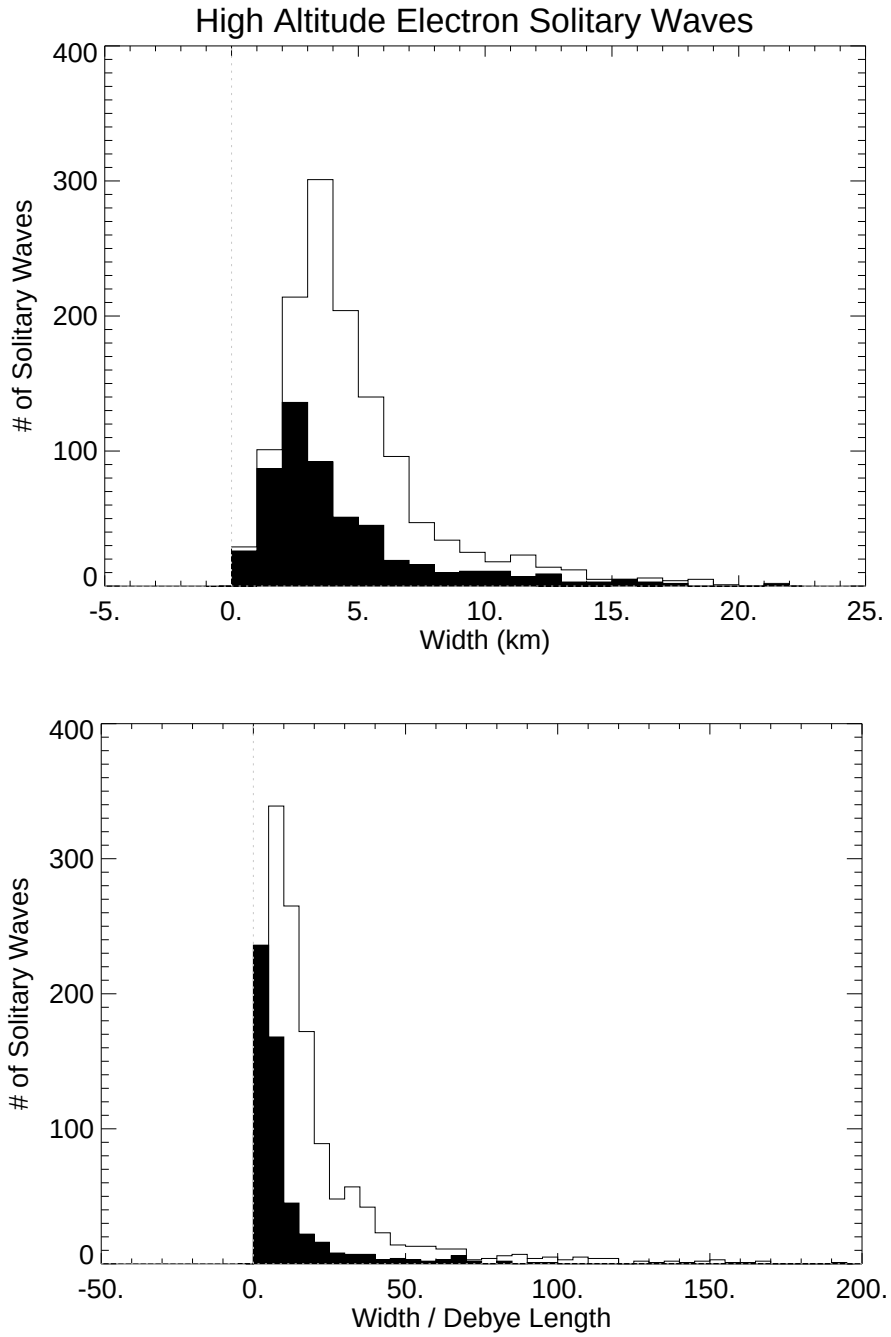

Figure 7.13: This figure shows histograms of the parallel scale size of the electron solitary waves. The top panel on this page show high altitude electron solitary wave results in km, while the bottom panel shows the same results normalized by the Debye length. The plot on the next page shows normalized results for all of the electron solitary waves from this study. The blacked in regions correspond to 0 s time delay solitary waves for which the width is found by using an arbitrary speed of 5000 km s^{-1}.

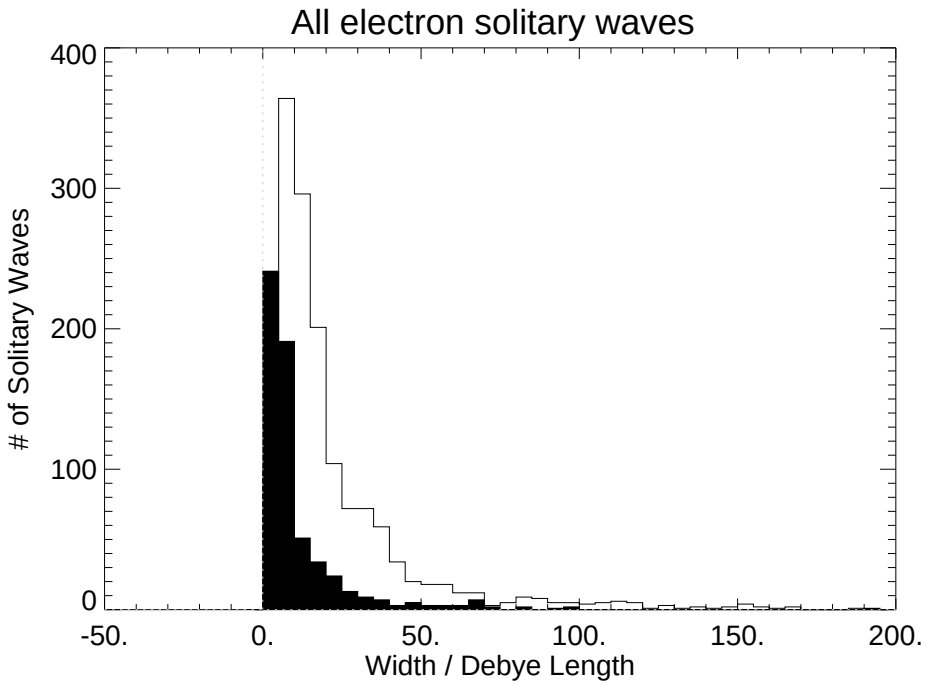

Figure 7.13 continued

7.3.5 Perpendicular Size

Since the perpendicular size of solitary waves cannot be measured directly, two methods of studying the perpendicular size of solitary waves were attempted. One method is to use the ratio of the perpendicular to the parallel electric field as evidence of the perpendicular scale size of the solitary waves. The basic idea is that, neglecting other factors, the smaller the perpendicular size of a solitary wave is, the larger the perpendicular electric field of a solitary wave will be since the charge will be more compressed. One theory gives a specific functional form to this relation for electron solitary waves:

$$\frac{L_{\parallel}}{L_{\perp}} = \frac{E_{\perp}}{E_{\parallel}} = \left(1 + \frac{\omega_{pe}^2}{\Omega_e^2}\right)^{-\frac{1}{2}} \tag{7.1}$$

where $L_{\parallel}$ and $L_{\perp}$ are the parallel and perpendicular scales sizes respectively and $E_{\parallel}$ and $E_{\perp}$ are the parallel and perpendicular electric fields respectively [*Franz et al.*, 2000]. This theory is based on the idea that the spatial gradients on the charge density in the solitary wave will

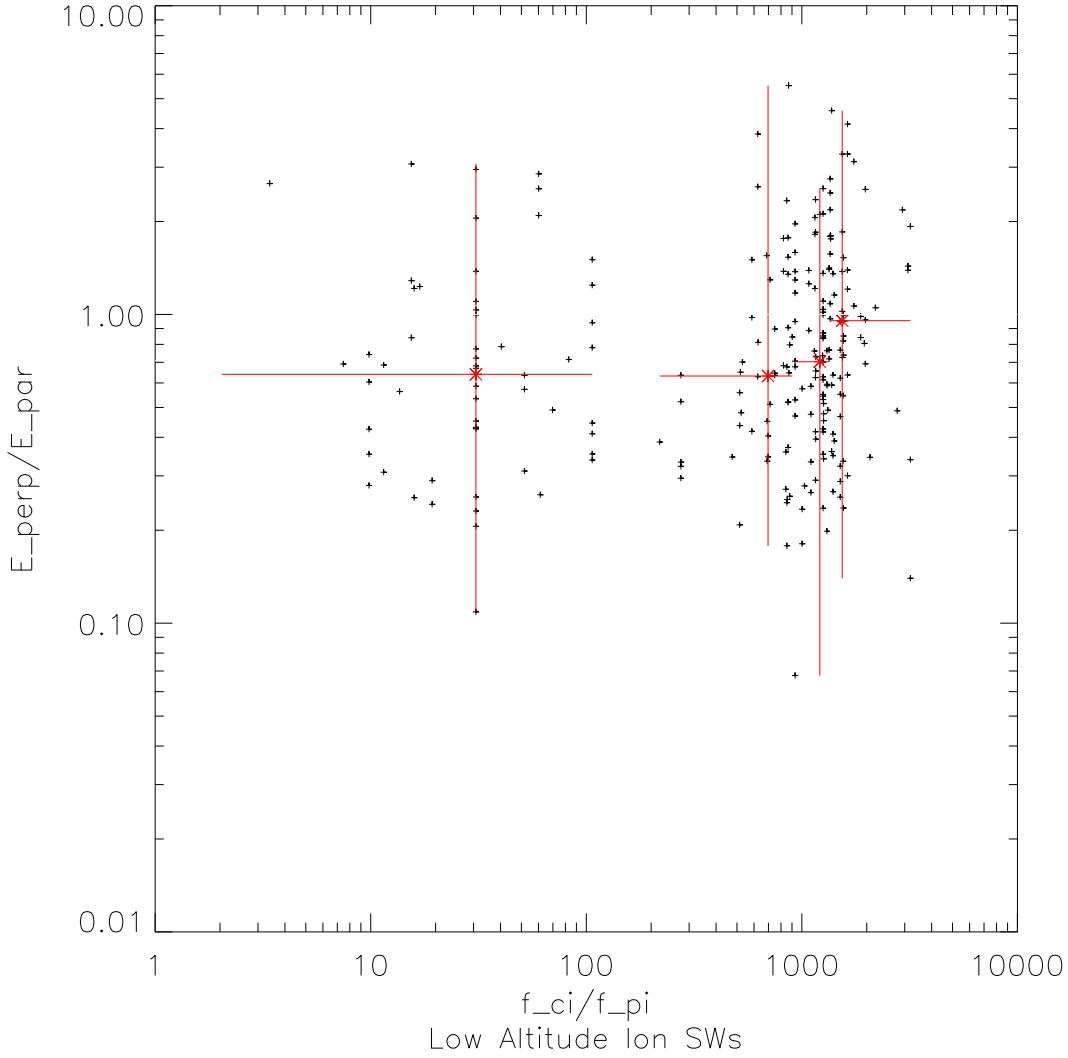

Figure 7.14: This figure shows the ratio of hydrogen cyclotron frequency to the hydrogen plasma frequency (which is roughly equal to the Debye length divided by the hydrogen gyro-radius) versus the ratio of the perpendicular to the parallel electric field. The black dots are for individual solitary waves. The red markers are for the same data separated into bins by the frequency ratio. The medians of the data in bins are plotted with the error bars equal to the limits of the measurements within a bin. This plot is for ion solitary waves observed at low altitude ($< 3\ R_E$ geocentric).

be balanced by gyro-motion effects in the perpendicular direction and Debye shielding effects in the parallel direction. The ratio of the perpendicular to the parallel electric field is plotted against the ratio of the electron cyclotron frequency to the plasma frequency in Figure 7.15 for all electron solitary waves seen in this study. Figure 7.14 is the same type of plot, but without any theoretical line since it is not clear if the theory can be extended to ions. In the case of the electrons, the trend of the data (as denoted by the red crosses) follows Equation 7.1 (as shown by the green lines) reasonably well, though there is quite a bit of scatter. In particular, the results for the high altitude electron solitary waves agree with *Franz et al.* [2000] results which were for a smaller set of data with a more limited range of cyclotron frequency to plasma frequency ratio. The ion results seem to be flat with the ratio being scattered around 1.

The other method of studying the perpendicular structure of the solitary wave involves looking at the shapes of the perpendicular signals of the solitary waves as described in Section 5.2.3. Figures 7.16 and 7.17 show the results of the study of the shapes for the low altitude ion and high altitude electron solitary waves respectively. The majority of both the ion and electron solitary waves have unipolar shaped perpendicular signals, as would be expected for a spacecraft traversing an ellipsoid charge distribution. Previous studies have stated that the perpendicular electric field signal of solitary waves tended to be unipolar, but have not examined these shapes in detail [*Ergun et al.*, 1998b; *Bounds et al.*, 1999; *Franz et al.*, 2000; *Dombeck et al.*, 2001]. The proportion of non-unipolar (bipolar, flat, or unclassified) signals is much higher for the ion solitary waves than the electron solitary waves. Ion cyclotron waves, which are present at low altitudes, have frequencies near the effective frequency of the ion solitary waves and are likely the cause of the higher proportion of non-unipolar signals. These ion cyclotron waves often are apparent in the perpendicular electric field at the same time the solitary waves are observed and they tend to make the perpendicular solitary wave signals much noisier in the low altitude region. So the fact that the results for the solitary wave shapes are not as strongly unipolar for the ion solitary waves is probably more a function of the plasma conditions in the region they were observed than of the ion solitary waves themselves.

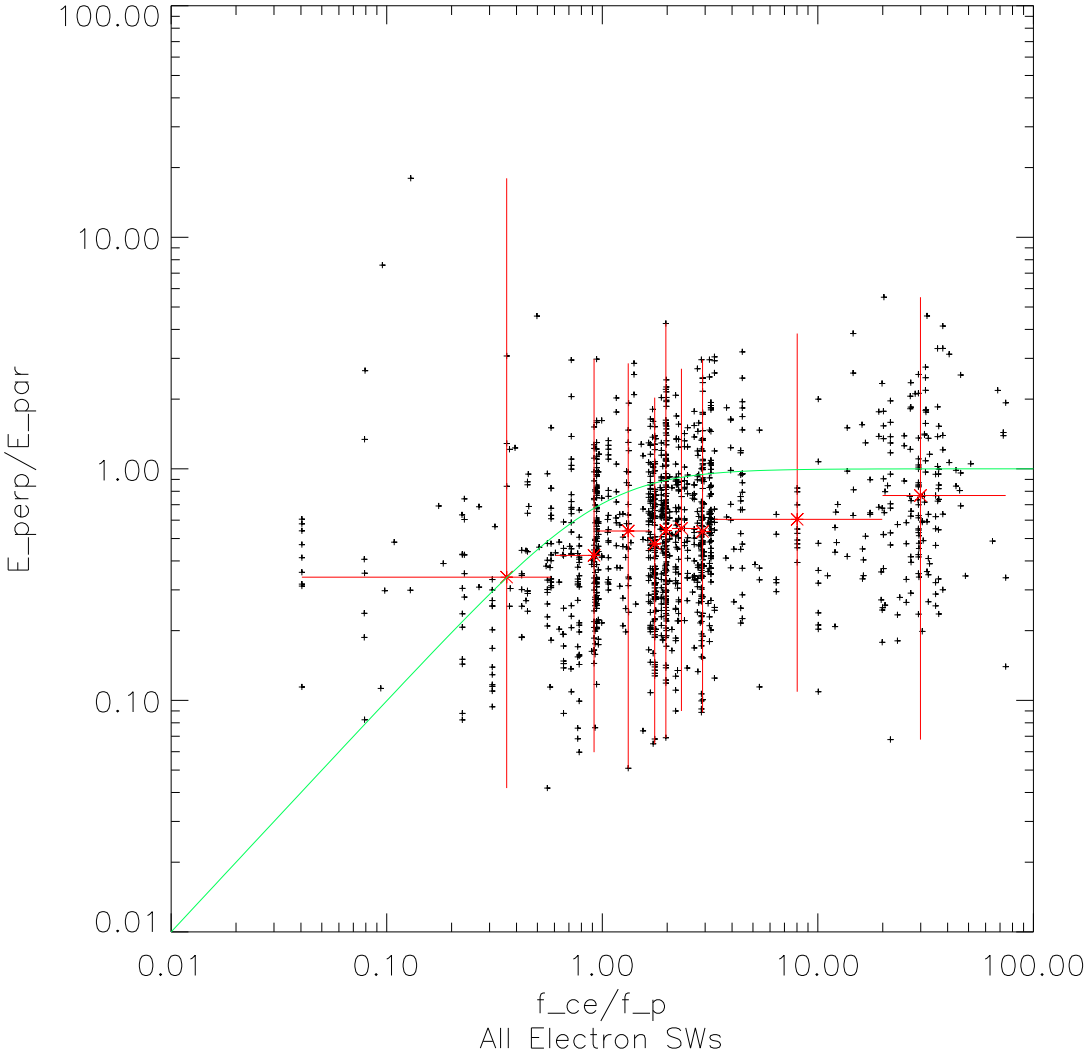

Figure 7.15: This figure shows the ratio of electron cyclotron frequency to the plasma frequency (which is roughly equal to the Debye length divided by the electron gyroradius) versus the ratio of the perpendicular to the parallel electric field. The black dots are for individual solitary waves. The red markers are for the same data separated into bins by the frequency ratio. The medians of the data are plotted with the error bars equal to the limits of the measurements within a bin. The green plotted line shows Equation 7.1 which is a theoretical prediction for this plot. This plot is for all electron solitary waves observed in this study.

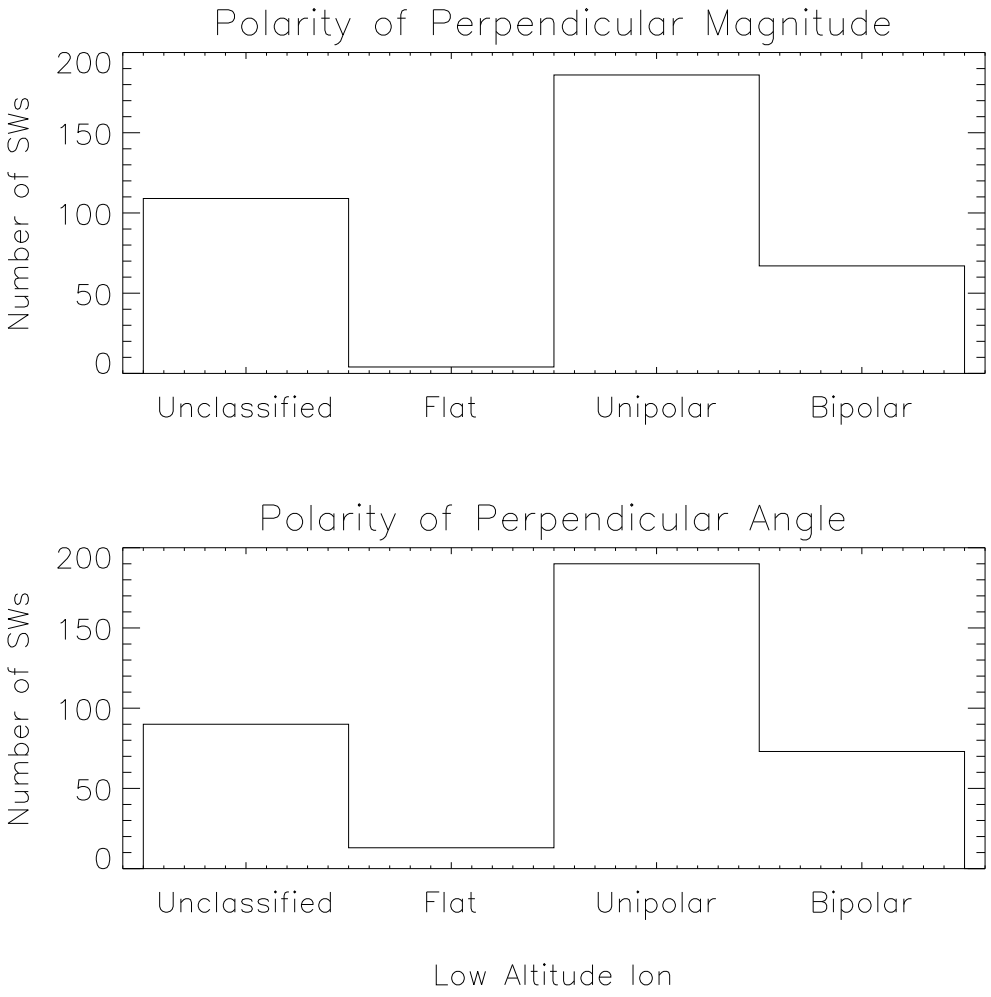

Figure 7.16: This figure shows the polarity classification for the perpendicular electric field signals of the low altitude ion solitary waves in study. The top panel shows the results for the magnitude of the perpendicular electric field, while the bottom panel shows results for the angle of the signal in the perpendicular plane. The classifications of the perpendicular signal are flat, unipolar, or bipolar for signals that had shapes that could be fitted, or unclassified for signals that did not meet any of the above classifications.

It is also interesting to note that within both the ion and electron solitary wave groups the results for the shapes of the magnitude and the angle shapes of the signals were similar. So not only does the magnitude of the perpendicular solitary wave signal change in a unipolar fashion, but the rotation of the angle of the electric field in the perpendicular plane is unipolar as well. There are some slight differences in the results for the angle and magnitude. In particular, the angle results have more signals classified as “flat” and fewer “unclassified” signals than the angle results for both electron and ion solitary waves.

7.4 Conclusions

While solitary waves have been observed by a variety of spacecraft for over twenty years, the Polar spacecraft, due to its instruments and orbit, leads to unique opportunities for studying solitary waves. Polar’s fully three dimensional EFI is well suited to detecting and timing solitary waves. The precession of Polar’s orbit leads to opportunities to observe solitary waves in many regions of the magnetosphere. A survey analyzing all of EFI’s high-time resolution bursts from 1997 was performed to take advantage of Polar’s abilities to observe solitary waves.

Analyzing the spatial distribution of the solitary waves in this survey is complicated by the method by which EFI bursts are chosen. In order to detect the most interesting electric fields in different regions of the magnetosphere, Polar’s orbit is divided into three regions and the time period with the largest amplitude electric fields for each region are saved for each orbit. A very non-uniform distribution of EFI bursts results, though within the bursts a fairly uniform fraction of the bursts have solitary waves. The most apparent asymmetry in the distribution of bursts with solitary waves is that low altitude bursts were twice as likely to include solitary waves as high altitude bursts, though differences in how the solitary wave selection criteria affect high and low altitudes might explain why a smaller fraction of high altitude bursts have solitary waves.

Statistics of the solitary waves in the study were divided into high and low altitude and into

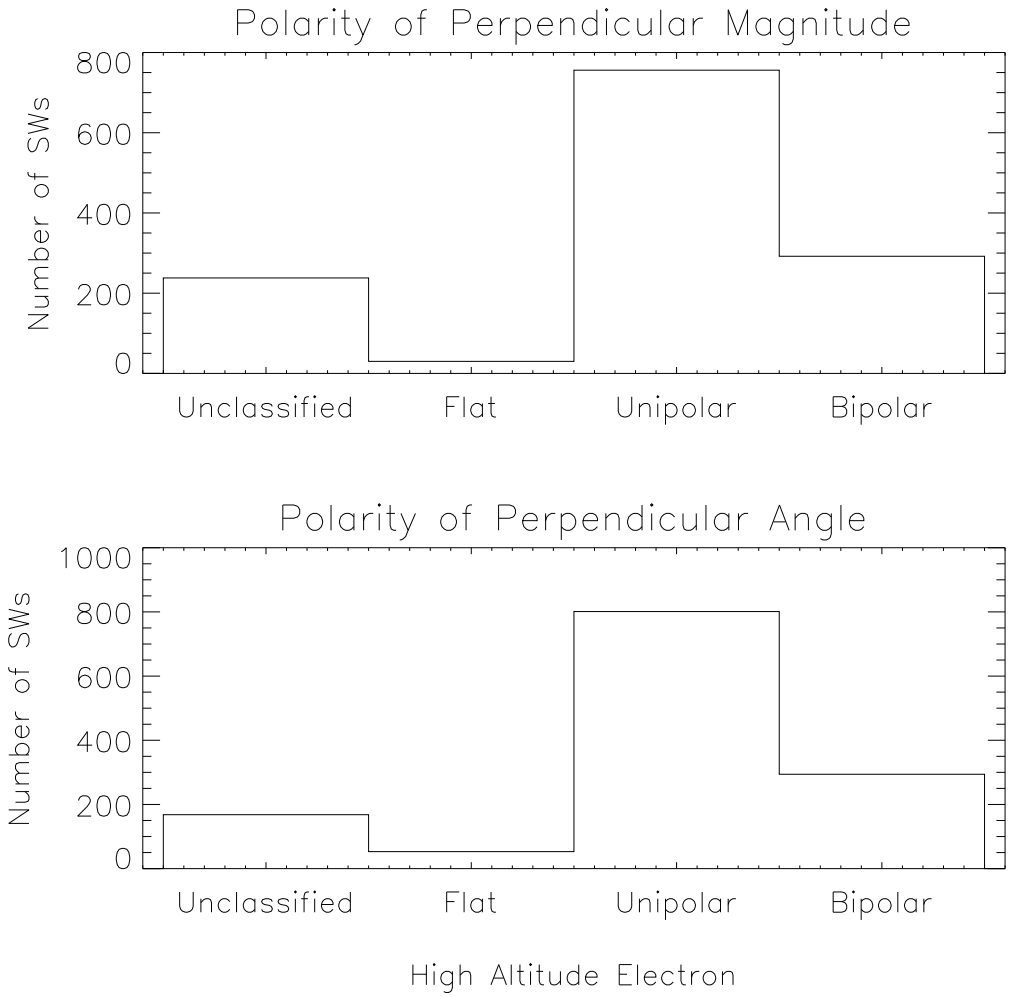

Figure 7.17: This figure shows the polarity classification for the perpendicular electric field signals of the low altitude ion solitary waves in study. The top panel shows the results for the magnitude of the perpendicular electric field, while the bottom panel shows results for the angle of the signal in the perpendicular plane. The classifications of the perpendicular signal are flat, unipolar, or bipolar for signals that had shapes that could be fitted, or unclassified for signals that did not meet any of the above classifications.

electron and ion solitary waves. Thirty solitary waves were classified as being high altitude ion solitary waves, which have not been observed previously. Upon closer examination, the validity of either the classification of these events as solitary waves or the classification of the solitary waves as ion solitary waves was called into question. After this review, 6 solitary waves were left as strong candidates, though further review of the particle data is needed to be certain these are high altitude ion solitary waves.

Statistical results on characteristics of the solitary waves were reported for the low altitude ion and high altitude electron solitary waves observed in this study. The speeds of the low altitude ion solitary waves averaged roughly 300 km s^{-1} and of the high altitude electron solitary waves were on the order of 1000s of km s^{-1}. These results agreed with previous observations. The potential amplitude of both ion and electron solitary waves were proportional to the solitary wave parallel scale size, though there was much more scatter in the electron solitary wave results. Proportionality between the potential amplitude and scale size supports the BGK phase space theories of solitary waves. The potential difference across the ion solitary waves supported the notion that the ion solitary waves make a small contribution to supporting the potential drop along auroral field lines.

The distributions of the scale size parallel to the magnetic field of the solitary waves were very similar for the electron and ion solitary waves, with typical values being about 15 λ_D for the electron solitary waves and about 22 λ_D for the electron solitary waves (roughly 4 km for each). These results matched previous parallel sizes for ion solitary waves and Polar observations of electron solitary waves, but were somewhat larger than FAST results for low altitude electron solitary waves. Since the scale sizes perpendicular to the magnetic field cannot be observed directly, two different methods of probing the perpendicular structure of the solitary waves were discussed. The shape of the perpendicular electric field signatures for the majority of both the electron and ion solitary waves were found to be unipolar as was expected. Also, the ratio of the parallel to perpendicular electric field, which is expected to be proportional to the ratio of the perpendicular to parallel scale size, was found to match the theoretical relation

for the electron solitary waves.

Chapter 8

Conclusions

The work presented here deals with the analysis of linear ion acoustic waves in the auroral zone, as well as simulations of ion solitary waves and Polar observations of ion and electron solitary waves.

8.1 Ion Acoustic Waves

Study of dispersion relations and the related information that dispersion relations provide is an important method for understanding waves observed in the magnetosphere. In the cold approximation of the dispersion relation, the temperature of the plasma particles is assumed to be 0. Because they are relatively easy to solve analytically, cold dispersion relations are useful for providing insight into basic plasma modes. They provide a good starting point for the study of linear plasma waves, but in many cases more detailed analysis requires that the full kinetic dispersion relation must be solved. In most cases, the kinetic dispersion relation must be solved numerically.

The comparison of cold and kinetic dispersion relations is here applied to FAST spacecraft observations of cyclotron waves in auroral zones. Waves with frequencies just above multiples of the ion cyclotron frequency were previously typically classified as EIC waves, since there

were often no observations of magnetic components of these waves and because the observations were consistent with the EIC dispersion relation. Recent FAST observations of these waves show that there are sometimes magnetic components and theoretical work on these waves suggest that their mode is an electromagnetic generalization of EIC waves. The dispersion relation results presented here show that the cold dispersion relation is not sufficient to study these generalized EIC waves, since the ratio of electric to magnetic field does not match the observations. On the other hand, kinetic dispersion relation results do match the FAST observations as well as the theory for generalized EIC waves.

8.2 Solitary Waves

Magnetospheric solitary waves, which are nonlinear structures most often observed in electric field measurements, have been observed throughout the magnetosphere by a variety of spacecraft. In this work, statistical study of Polar observations of electron and ion solitary waves is compared to simulations of ion solitary waves and previous results.

While solitary waves have been observed by a variety of spacecraft for over twenty years, the Polar spacecraft, due to its instruments and orbit, leads to unique opportunities for studying solitary waves. Polar's fully three-dimensional EFI is well suited to detecting and timing solitary waves. The precession of Polar's orbit leads to opportunities to observe solitary waves in many regions of the magnetosphere. A statistical survey analyzing all of EFI's high-time resolution bursts from 1997 was performed to take advantage of Polar's abilities to observe solitary waves.

Analyzing the spatial distribution of the solitary waves in this survey is complicated by the method by which EFI bursts are chosen. Polar's orbit is divided into three regions and the time period with the largest amplitude electric fields for each region is saved for each orbit. A very non-uniform distribution of EFI bursts results, though within the bursts a fairly uniform fraction of the bursts have solitary waves. Roughly 13% of the high altitude bursts and 24% of the low

altitude burst contained solitary waves. The most apparent asymmetry in the distribution of bursts with solitary waves is that low altitude bursts were twice as likely to include solitary waves as high altitude bursts, though differences in how the solitary wave selection criteria affect high and low altitudes might explain why a smaller fraction of high altitude bursts have solitary waves.

Statistics of the solitary waves in the study are divided into high and low altitude and into electron and ion solitary waves. Thirty solitary waves are classified as high altitude ion solitary waves, which have not been observed previously. Upon closer examination, the validity of either the classification of these events as solitary waves or the classification of the solitary waves as ion solitary waves was called into question. After this review, six solitary waves were left as strong candidates, though further review of the particle is needed to be certain these are high altitude ion solitary waves.

8.2.1 Ion Solitary Waves

In this analysis, the low altitude ion solitary wave results from the statistical study were compared to the 2.5D electrostatic PIC simulation results. For both simulations and observations, the solitary wave speeds fall between the speeds of the hydrogen and oxygen beams, as would be expected if the two-stream instability is involved in generating the ion solitary waves. Ion cyclotron waves, which may be generated due to the two-stream instability, are also present before the solitary waves form in the simulations and are often seen in the observations as well. These ion cyclotron waves would be expected if the solitary waves are caused by the two-stream instability. The mechanism for generation of solitary waves from ion cyclotron waves in not completely worked out.

The relationship between potential amplitude and scale size is a strong test of the theories concerning ion solitary waves, since the ion acoustic soliton theory predicts that potential amplitude and scale size are inversely proportional, while the BGK phase space hole explanation for solitary waves predicts that potential amplitude and scale size will be directly proportional.

The simulation and statistical survey results both showed the potential amplitude being directly proportional to the parallel scale size of the ion solitary waves.

The perpendicular scale size of the ion solitary waves leads to another test of the ion acoustic soliton theory, which predicts the perpendicular scale size should be substantially larger than than the parallel scale size, but not for the BGK phase space explanation, which makes no definite prediction regarding the perpendicular scale size. The perpendicular sizes of the ion solitary waves were somewhat smaller than the parallel scale sizes in the simulation results. In the observations, the perpendicular size cannot be directly measured, so the ratio of the parallel electric field to the perpendicular electric field is used. The results from this ratio also suggest that perpendicular scale size of the ion solitary waves is smaller the parallel scale size. So this test also goes against the ion acoustic soliton theory.

Overall, these simulation and observational results suggest that the BGK phase space hole theory is a better explanation of ion solitary waves than the ion acoustic soliton theory. In particular, the ion two-stream instability may function as the generation mechanism for ion solitary waves, since the BGK phase space hole theory does not include a generation mechanism. The two-stream instabilities role as a generation mechanism is supported by the observations of ion cyclotron waves, both in simulations and in space, when the ion solitary waves are present, which theoretical results of the two-stream instability predict. More theoretical exploration of a two-stream/BGK phase space hole explanation of ion solitary waves is needed to be certain that this theory is correct.

8.2.2 Electron Solitary Waves

The statistical survey results for the electron solitary waves were generally in agreement with previous observations and with these structures being BGK phase space holes. The high altitude electron solitary waves speeds are on the order of thousands of km s^{-1}. The potential amplitude is proportional to the solitary wave parallel scale size, though there was a significant amount of scatter. The typical scale size parallel to the magnetic field was about 15 λ_D (4 km).

These results were somewhat larger than previous FAST results for low altitude electron solitary waves, but agreed with previous Polar results. Since the scale sizes perpendicular to the magnetic field cannot be observed directly, two different methods of probing the perpendicular structure of the solitary waves were discussed. The shape of the perpendicular electric field signatures for the majority of the electron solitary waves are unipolar as was expected. Also, the ratio of the parallel to perpendicular electric field, which is expected to be proportional to the ratio of the perpendicular to parallel scale size, was found to be consistent with a theoretical prediction of this relationship.

8.3 Future Work

Many open questions exist concerning solitary waves and their importance in the magnetospheric dynamics. This work suggests several areas that might be beneficial to explore in order to better understand solitary waves.

The first is further exploration of a theory combining the two-stream instability and BGK phase space holes to explain ion solitary waves, as was mentioned above. In particular, the theory laid here does not explain how ion cyclotron waves can form quasi-stable BGK phase space holes. Particularly troubling is explaining how obliquely propagating ion cyclotron waves transform into parallel propagating solitary waves. It is possible that the ion cyclotron waves are being converted to being converted to parallel propagating ion acoustic waves as an intermediate step before the solitary waves form, but this needs to be examined more closely.

For simulations, the obvious next step is to perform a statistical simulation study that is analogous to the Polar observation study presented here. A study of this type would bolster the simulation results, which at this point are based on study of relatively few individual solitary waves for each type of simulation run. Also, more simulations should be done with variations of the simulation parameters such as the mass ratio and the simulation box length should be performed in order to continue to search for differences in results.

For observations, further statistical studies including additional years of data would be informative, since due to the precession of Polar's orbit the more recent time periods sample other regions of the magnetosphere. Further study of this sort could show whether the characteristics of solitary waves in the cusp and the magnetopause are similar to those seen in the plasma sheet boundary layer. Also, further work should be done to confirm the existence of high-altitude ion solitary waves as presented here.

Bibliography

Allen, J. E., The early history of solitons (solitary waves), *Phys. Scripta*, *57*, 436–441, 1998. 3

Bale, S. D., P. J. Kellogg, D. E. Larson, R. P. Lin, K. Goetz, and R. P. Lepping, Bipolar electrostatic structures in the shock transition region: Evidence of electron phase space holes, *Geophys. Res. Lett.*, *25*, 2929–2932, 1998. 3.1

Barnes, C., M. K. Hudson, and W. Lotko, Weak double layers in ion-acoustic turbulence, *Phys. Fluids*, *28*, 1055–1062, 1985. 3.2.1, 6.1, 6.2, 6.3, 6.4.1, 6.4.1

Baumjohann, W., and R. A. Treumann, *Basic Space Plasma Physics*, Imperial College Press, London, 1997. 1, 1.1

Bergmann, R., and W. Lotko, Transition to unstable ion flow in parallel electric fields, *J. Geophys. Res.*, *91*, 7033–7045, 1986. 6.3, 6.4.1

Bergmann, R., I. Roth, and M. K. Hudson, Linear stability of the H^+/–O^+ two-stream interaction in a magnetized plasma, *J. Geophys. Res.*, *93*, 4005–4020, 1988. 6.2, 6.3, 6.4.1

Bergmann, R., J. P. Crumley, C. A. Cattell, R. L. Lysak, and C. Chaston, Electromagnetic generalization of EIC waves, *Trans. Am. Geophys. Union (EOS), 79 (45), Fall Meet. Suppl.*, SM71A–12, 1998. 2.4.2

Bernstein, I. B., J. M. Greene, and M. D. Kruskal, Exact nonlinear plasma oscillations, *Phys. Rev.*, *108*, 546, 1957. 3.2.3

Birdsall, C. K., and A. B. Langdon, *Plasma physics via computer simulation*, Adam Hilger, Bristol, UK, 1991. 4.1, 4.2, 4.3

Borovsky, J. E., Double layers do accelerate particles in the auroral zone, *Phys. Rev. Lett.*, *69*, 1054–1056, 1992. 3

Borovsky, J. E., Auroral arc thicknesses as predicted by various theories, *J. Geophys. Res.*, *98*, 6101–6138, 1993. 3.3, 3.2.2

Boström, R., and R. Anson, A new member of your management team-cwss (meeting support system), *Information Executive*, *1*, 43–46, 1988. 3.2.1

Boström, R., G. Gustafsson, B. Holback, G. Holmgren, H. Koskinen, and P. Kintner, Characteristics of solitary waves and weak double layers in the magnetospheric plasma, *Phys. Rev. Lett.*, *61*, 82–85, 1988. 3.1, 3.1, 6.1, 6.4.2

Bounds, S. R., R. F. Pfaff, S. F. Knowlton, F. S. Mozer, M. A. Temerin, and C. A. Kletzing, Solitary potential structures associated with ion and electron beams near 1 R_E altitude, *J. Geophys. Res.*, *104*, 28,709–28,717, 1999. 3.1, 3.1, 5.1.1, 6.3, 6.4.2, 7.3.1, 7.3.3, 7.3.4, 7.3.5

Cattell, C., J. Wygant, J. Dombeck, F. S. Mozer, M. Temerin, and C. T. Russell, Observations of large amplitude parallel electric field wave packets at the plasma sheet boundary, *Geophys. Res. Lett.*, *25*, 857–860, 1998. 2.3.2, 5.1.1

Cattell, C., J. Crumley, J. Dombeck, J. Wygant, and F. S. Mozer, Polar observations of solitary waves at the Earth's magnetopause, *Geophys. Res. Lett.*, *29*, 10.1029/2001GL014,046, 2002. 3.1, 5.1.1

Cattell, C. A., F. S. Mozer, I. Roth, R. R. Anderson, R. C. Elphic, W. Lennartsson, and E. Ungstrup, ISEE 1 observations of electrostatic ion cyclotron waves in association with ion beams on auroral field lines from approximately 2.5 to 4.5 R_e, *J. Geophys. Res.*, *96*, 11,421–11,439, 1991. 2.1

Cattell, C. A., et al., Comparisons of Polar satellite observations of solitary wave velocities in the plasma sheet boundary and the high altitude cusp to those in the auroral zone, *Geophys. Res. Lett.*, *26*, 425–428, 1999. 3.1, 5.1.1, 6.4.1, 6.5

Chaston, C. C., et al., Characteristics of electromagnetic proton cyclotron waves along auroral field lines observed by FAST in regions of upward current, *Geophys. Res. Lett.*, *25*, 2057–2060, 1998. 2.1, 2.4.2

Crumley, J. P., C. A. Cattell, R. L. Lysak, and J. P. Dombeck, Studies of ion solitary waves using simulations including hydrogen and oxygen beams, *J. Geophys. Res.*, *106*, 6007–6015, 2001. 1

Dombeck, J. P., C. A. Cattell, J. P. Crumley, W. K. Peterson, H. L. Collin, and C. A. Kletzing, Observed trends in auroral zone ion-mode solitary wave structure characteristics using data from Polar, *J. Geophys. Res.*, *106*, 19,013–19,021, 2001. 3.1, 3.1, 3.2.1, 5.1.1, 5.2, 5.3, 5.2.1, 5.6, 6.3, 6.5, 6.6, 6.4.1, 6.4.2, 7.3.1, 7.3.2, 7.3.3, 7.3.4, 7.3.5

Dubouloz, N., R. Pottelette, M. Malingre, and R. A. Treumann, Generation of broadband electrostatic noise by electron acoustic solitons, *Geophys. Res. Lett.*, *18*, 155–158, 1991. 6.1

Dupree, T. H., Theory of phase-space density holes, *Phys. Fluids*, *25*, 277–289, 1982. 3.2.3, 6.1

Ergun, R. E., C. W. Carlson, J. P. McFadden, F. S. Mozer, L. Muschietti, I. Roth, and R. J. Strangeway, Debye-scale plasma structures associated with magnetic-field-aligned electric fields, *Phys. Rev. Lett.*, *81*, 826–829, 1998a. 3.1, 5.2.1, 7.3.4

Ergun, R. E., Y.-J. Su, L. Andersson, C. W. Carlson, J. P. McFadden, F. S. Mozer, D. L. Newman, M. V. Goldman, and R. J. Strangeway, Direct observation of localized parallel electric fields in a space plasma, *Phys. Rev. Lett.*, *87*, 1–4, 2001. 3.1, 3.2.2

Ergun, R. E., L. Andersson, D. S. Main, Y. J. Su, C. W. Carlson, J. P. McFadden, and F. S. Mozer, Parallel electric fields in the upward current region of the aurora: Direct observations

of oblique double layers, *Trans. Am. Geophys. Union (EOS), 83 (19), Spring Meet. Suppl., Abstract SM21B-03*, 2002. 3.2.2

Ergun, R. E., et al., FAST satellite observations of large-amplitude solitary structures, *Geophys. Res. Lett., 25*, 2041–2044, 1998b. 3.1, 4.2, 7.3.1, 7.3.4, 7.3.5

Ergun, R. E., et al., FAST satellite observations of electric field structures in the auroral zone, *Geophys. Res. Lett., 25*, 2025–2028, 1998c. 1.2, 3, 3.1

Eriksson, A. I., and R. Boström, Are weak double layers important for auroral acceleration?, in *Auroral Plasma Dynamics, Geophysical Monograph Series*, edited by R. L. Lysak, pp. 258–264, AGU, 1993. 3.6, 3.3

Eriksson, A. I., A. Mälkki, P. O. Dovner, R. Boström, G. Holmgren, and B. Holback, A statistical survey of auroral solitary waves and weak double layers. ii. measurement accuracy and ambient plasma density, *J. Geophys. Res., 102*, 11,385–11,398, 1997. 3.2.1

Franz, J. R., P. M. Kintner, and J. S. Pickett, POLAR observations of coherent electric field structures, *Geophys. Res. Lett., 25*, 1277–1280, 1998. 3.1, 5.1.1, 7.3.1, 7.3.4

Franz, J. R., P. M. Kintner, C. E. Seyler, J. S. Pickett, and J. D. Scudder, On the perpendicular scale of electron phase-space holes, *Geophys. Res. Lett., 27*, 169–172, 2000. 3.1, 7.3.5, 7.3.5

Goldman, M. V., M. M. Oppenheim, and D. L. Newman, Nonlinear two-stream instabilities as an explanation for auroral bipolar wave structures, *Geophys. Res. Lett., 26*, 1821–1824, 1999. 6.1

Gray, P. C., M. K. Hudson, R. Bergmann, and I. Roth, Simulation study of ion two-stream instability in the auroral acceleration region, *Geophys. Res. Lett., 17*, 1609–1612, 1990. 6.3

Gray, P. C., M. K. Hudson, W. Lotko, and R. Bergmann, Decay of ion beam driven acoustic waves into ion holes, *Geophys. Res. Lett., 18*, 1675–1678, 1991. 6.4.1

Gray, P. C., M. K. Hudson, and W. Lotko, Acoustic double layers in multispecies plasma, *IEEE Trans. Plasma Sci.*, *20*, 745–755, 1992. 6.1, 6.4.1

Harten, R., and K. Clark, The design feature of the GGS Wind and Polar spacecraft, in *The Global Geospace Mission*, edited by C. T. Russell, pp. 23–40, Kluwer Academic Publishers, Dordrecht, Netherlands, 1995. 5.1

Harvey, P., et al., The electric field instrument on the POLAR satellite, *Space Sci. Rev.*, *71*, 583–596, 1995. 5.1.2, 5.2, 7.2

Hudson, M. K., W. Lotko, I. Roth, and E. Witt, Solitary waves and double layers on auroral field lines, *J. Geophys. Res.*, *88*, 916–926, 1983. 6.4.1

Hudson, M. K., T. L. Crystal, W. Lotko, and C. Barnes, Weak double layers in the auroral ionosphere, in *Laser & Particle Beams*, vol. 5, pp. 295–313, Cambridge University Press, Cambridge, UK, 1987. 6.1

Iijima, T., and T. A. Potemra, Field-aligned currents in the dayside cusp observed by Triad, *J. Geophys. Res.*, *81*, 5971–5979, 1976. 1.4

Johnson, M. T., Large scale thermal plasma structure of the magnetosphere using floating potential measurements from the Polar spacecraft, Ph.D. thesis, University of Minnesota, 2002. 5.2

Kelley, M. C., and R. A. Heelis, *The Earth's Ionosphere: Plasma Physics and Electrodynamics*, Academic Press, San Diego, 1989. 1, 1.2

Kintner, P. M., M. C. Kelley, R. D. Sharp, A. G. Ghielmetti, M. Temerin, C. Cattell, P. F. Mizera, and J. F. Fennell, Simultaneous observations of energetic (keV) upstreaming and electrostatic hydrogen cyclotron waves, *J. Geophys. Res.*, *84*, 7201–7212, 1979. 2.1

Kivelson, A., M. G. Kivelson, and C. T. Russell, *Introduction to Space Physics*, Cambridge University Press, London, 1995. 1

Kojima, H., H. Matsumoto, S. Chikuba, S. Horiyama, M. Ashour-Abdalla, and R. R. Anderson, Geotail waveform observations of broadband/narrowband electrostatic noise in the distant tail, *J. Geophys. Res.*, *102*, 14,439–14,455, 1997. 3.1

Korteweg, D. J., and G. de Vries, On the change of form of long waves advancing in a rectangular canal and on a new type of long stationary waves, *Philosophical Magazine*, *36*, 422–443, 1895. 3

Koskinen, H. E., and A. M. Mälkki, Auroral weak double layers: A critical assessment, in *Auroral Plasma Dynamics*, *Geophysical Monograph Series*, edited by R. L. Lysak, pp. 97–104, AGU, 1993. 3.1

Koskinen, H. E. J., R. Lundin, and B. Holback, On the plasma environment of solitary waves and weak double layers, *J. Geophys. Res.*, *95*, 5921–5929, 1990. 3.1

Koskinen, H. E. J., R. E. Lopez, R. J. Pellinen, T. I. Pulkkinen, D. N. Baker, and T. Bosinger, Pseudobreakup and substorm growth phase in the ionosphere and magnetosphere, *J. Geophys. Res.*, *98*, 5801–5813, 1993. 3.2.3

Krasovsky, V. L., H. Matsumoto, and Y. Omura, Bernstein-greene-kruskal analysis of electrostatic solitary waves observed with Geotail, *J. Geophys. Res.*, *102*, 22,131–22,139, 1997. 3.2.3

Lawson, W. S., and P. C. Gray, PDW1/PDW2 user's manual, 1989, unpublished. 4.3, 4.4

Lotko, W., Reflection dissipation of an ion-acoustic soliton, *Phys. Fluids*, *26*, 1771–1779, 1983. 3.2.1, 6.1, 6.4.1

MacNeice, P., Particle-mesh techniques, *NASA Contractor Report 4666*, NASA - Goddard, 1995. 4.1

Mälkki, A., H. Koskinen, R. Boström, and B. Holback, On theories attempting to explain observations of solitary waves and weak double layers in the auroral magnetosphere, *Phys. Scripta*, *39*, 787–793, 1989. 3.2.1

Mälkki, A., A. I. Eriksson, P.-O. Dovner, R. Boström, B. Holback, G. Holmgren, and H. E. J. Koskinen, A statistical survey of auroral solitary waves and weak double layers. 1. Occurrence and net voltage, *J. Geophys. Res.*, *98*, 15,521–15,530, 1993. 3.1, 3.1, 7.3.3

Mangeney, A., et al., WIND observations of coherent electrostatic waves in the solar wind, *Ann. Geophys.*, *17*, 307–320, 1999. 3.1

Marchenko, V. A., and M. K. Hudson, Beam-driven acoustic solitary waves in the auroral acceleration region, *J. Geophys. Res.*, *100*, 19,791–19,803, 1995. 3.2.1, 4.4, 6.1, 6.2, 6.4.1, 6.4.1, 6.4.2

Matsumoto, H., H. Kojima, T. Miyatake, Y. Omura, M. Okada, I. Nagano, and M. Tsutui, Electrostatic solitary waves (ESW) in the magnetotail: BEN wave forms observed by Geotail, *Geophys. Res. Lett.*, *21*, 2915–2918, 1994. 3.1, 3.2.3

Matsumoto, H., et al., Generation mechanism of esw based on geotail plasma wave observation, plasma observation and particle simulation, *Geophys. Res. Lett.*, *26*, 421–424, 1999. 3.1

McFadden, J. P., C. W. Carlson, and R. E. Ergun, Microstructure of the auroral acceleration region as observed by FAST, *J. Geophys. Res.*, *104*, 14,453–14,480, 1999a. 1.2, 3, 3.1, 7.3.1

McFadden, J. P., C. W. Carlson, and R. E. Ergun, Ion solitary waves and auroral ion beams (abstract), *Trans. Am. Geophys. Union (EOS), 80 (46), Fall Meet. Suppl.*, F834, 1999b. 6.4.2

McFadden, J. P., C. W. Carlson, R. E. Ergun, D. M. Klumpar, and E. Moebius, Ion and electron characteristics in auroral density cavities associated with ion beams: No evidence for cold ionospheric plasma, *J. Geophys. Res.*, *104*, 14,671–14,682, 1999c. 3.1, 3.2.1, 4.5, 6.1, 6.2, 6.2

McFadden, J. P., C. W. Carlson, R. E. Ergun, F. S. Mozer, L. Muschietti, I. Roth, and E. Moebius, FAST observations of ion solitary waves, *J. Geophys. Res.*, *submitted*, 2002. 3.1, 3.1, 6.4.2

Morse, R. L., and C. W. Nielson, One, two-, and three-dimensional numerical simulation of two-beam plasmas, *Phys. Rev. Lett.*, *23*, 1087–1089, 1969. 3.2.3

Mozer, F. S., Analyses of techniques for measuringDC and AC electric fields in the magnetosphere, *Space Sci. Rev.*, *14*, 272–313, 1973. 5.2

Mozer, F. S., and C. A. Kletzing, Direct observation of large, quasi-static, parallel electric fields in the auroral acceleration region, *Geophys. Res. Lett.*, *25*, 1629–1632, 1998. 1.2, 3.1

Mozer, F. S., R. Ergun, M. Temerin, C. Cattell, J. Dombeck, and J. Wygant, New features of time domain electric-field structures in the auroral acceleration region, *Phys. Rev. Lett.*, *79*, 1281–1284, 1997. 3.1, 3.2, 3.1, 3.2.2

Muschietti, L., R. E. Ergun, I. Roth, and C. W. Carlson, Phase-space electron holes along magnetic field lines, *Geophys. Res. Lett.*, *26*, 1093–1096, 1999a. 3.2.3, 6.1

Muschietti, L., R. E. Ergun, I. Roth, and C. W. Carlson, Correction to “Phase-space electron holes along magnetic field lines”, *Geophys. Res. Lett.*, *26*, 1689, 1999b. 3.2.3, 6.1, 7.3.2

Newman, D. L., M. V. Goldman, and R. E. Ergun, Evidence for correlated double layers, bipolar structures, and very-low-frequency saucer generation in the auroral ionosphere, *Phys. Plasmas*, *9*, 2337–2343, 2002. 3.2.2

Omura, Y., H. Kojima, and H. Matsumoto, Computer simulation of electrostatic solitary waves: a nonlinear model of broadband electrostatic noise, *Geophys. Res. Lett.*, *21*, 2923–2926, 1994. 3.2.3

Omura, Y., H. Kojima, N. Miki, T. Mukai, H. Matsumoto, and R. Anderson, Electrostatic solitary waves carried by diffused electron beams observed by the Geotail spacecraft, *J. Geophys. Res.*, *104*, 14,627–14,637, 1999. 3.2.3

Oppenheim, M. M., G. Vetoulis, D. L. Newman, and M. V. Goldman, Evolution of electron phase-space holes in 3D, *Geophys. Res. Lett.*, *28*, 1891–1894, 2001. 3.2.3

Parks, G. K., *Physics of Space Plasmas: An Introduction*, Addison-Wesley, Redwood City, California, 1991. 1, 1.1, 1.2

Peredo, M., and S. Boardsen, Polar spacecraft orbit plots, 1996, http://www-spof.gsfc.nasa.gov/orbits/menu_orbits.html. 5.1

Qian, S., W. Lotko, and M. K. Hudson, Oxygen acoustic solitary waves in a magnetized plasma, *J. Geophys. Res.*, *94*, 1339–1346, 1989. 6.1, 6.4.1

Rayleigh, L., On waves propagated along the plane surface of an elastic solid, in *Rayleigh-wave theory and application : Proceedings of an international symposium organised by the Rank Prize Funds at the Royal Institution, London, 15-17 July, 1985*, edited by E. A. Ash and E. G. S. Paige, Springer-Verlag, 1879. 3

Reiff, P. H., G. Lu, J. L. Burch, J. D. Winningham, L. A. Frank, J. D. Craven, W. K. Peterson, and R. A. Heelis, On the high- and low-altitude limits of the auroral acceleration region, in *Auroral Plasma Dynamics, Geophysical Monograph Series*, edited by R. L. Lysak, pp. 143–154, AGU, 1993. 1.2

Rönnmark, K., Computation of the dielectric tensor of a Maxwellian plasma, *Phys. Plasmas*, *25*, 699–701, 1983. 2.4

Russell, C. T. (Ed.), *The Global Geospace Mission*, Kluwer Academic Publishers, Dordrecht, Netherlands, 1995. 5.1

Russell, J. S., Report on waves, in *Report of the 14th meeting of the British Association for the Advancement of Science, York, September 1844*, pp. 311–390, 1845. 3

Sagdeev, R. Z., Cooperative phenomena and shock waves in collisionless plasma, *Reviews of Plasma Physics*, *4*, 1966. 3.2.1

Sagdeev, R. Z., and A. A. Galeev, *Nonlinear Plasma Theory*, W. A. Benjamin Inc., New York, 1969. 3.2.1

Sato, T., and H. Okuda, Ion-acoustic double layers, *Phys. Rev. Lett.*, *44*, 740–743, 1980. 3.2.1

Scudder, J., and et al., Hydra - a 3-D electron and ion hot hot plasma instrument for the Polar spacecraft of the GGS mission, in *The Global Geospace Mission*, edited by C. T. Russell, p. 439, Kluwer Academic Publishers, Dordrecht, Netherlands, 1995. 5.1.3

Shelley, J., and et al., The Toroidal Imaging Mass-Angle Spectrograph (TIMAS) for the Polar mission, in *The Global Geospace Mission*, edited by C. T. Russell, p. 397, Kluwer Academic Publishers, Dordrecht, Netherlands, 1995. 5.1.3

Singh, N., Electron holes as a common feature of double-layer-driven plasma waves, *Geophys. Res. Lett.*, *27*, 927–930, 2000. 3.2.3, 6.1

Stix, T. H., *Waves in Plasmas*, American Institute of Physics, 1992. 2.3.1, 2.4.1, 3.2

Strangeway, R. J., et al., FAST observations of VLF waves in the auroral zone: Evidence of very low plasma densities, *Geophys. Res. Lett.*, *25*, 2065–2068, 1998. 3.1, 6.1

Suess, S. T., and B. T. Tsurutani, *From the Sun: Auroras, Magnetic Storms, Solar Flares, and Cosmic Rays*, American Geophysical Union, Washington, D. C., 1998. 1

Temerin, M., and R. L. Lysak, Electromagnetic ion cyclotron mode (ELF) waves generated by auroral electron precipitation, *J. Geophys. Res.*, *89*, 2849–2859, 1984. 2.1

Temerin, M., K. Cerny, W. Lotko, and F. S. Mozer, Observations of double layers and solitary waves in the auroral plasma, *Phys. Rev. Lett.*, *48*, 1175–1179, 1982. 3.1, 3.1, 3.1

Tetreault, D., Theory of electric fields in the auroral acceleration region, *J. Geophys. Res.*, *96*, 3549–3563, 1991. 3.2.3, 6.1, 6.4.1

Tetreault, D. J., Growing ion holes as the cause of auroral double layers, *Geophys. Res. Lett.*, *15*, 164–167, 1988. 3.2.3, 7.3.2

Treumann, R. A., and W. Baumjohann, *Advanced Space Plasma Physics*, Imperial College Press, London, 1997. 3.2

Yi-Jiun, S., R. E. Ergun, W. K. Peterson, T. G. Onsager, R. Pfaff, C. W. Carlson, and R. J. Strangeway, Fast Auroral Snapshot observations of cusp electron and ion structures, *J. Geophys. Res.*, *106*, 25,595–25,600, 2001. 3.1

Zakharov, V. E., and E. A. Kuznetsov, On three-dimensional solitons (in plasma), *Sov. Phys.–JETP*, *39*, 285–288, 1974. 6.4.1